



Effects of electron-positron pairs on active galactic nuclei
by Bradley Gene Tritz

A thesis submitted in partial fulfillment of the requirements for the degree of Doctor of Philosophy in
Physics

Montana State University

© Copyright by Bradley Gene Tritz (1990)

Abstract:

Electron-positron pair creation is investigated in and around accretion flows within active galactic nuclei. First, two-temperature accretion disk models from the 1970's are re-examined, and the effects of pairs on disk structure are calculated. It is found that thermal pair production produces insufficient pairs to greatly affect the disk, but that nonthermal processes produce sufficient pairs to significantly alter flow structure for a wide range of parameters. Then improvements are made upon earlier studies of pair-induced over-cooling of two-temperature spherical accretion flows. It is found that thermal processes produce insufficient pairs to cause over-cooling; however, nonthermal pair production can be an effective cooling agent. Finally, the origin, vertical structure, and radiation spectrum of steady-state pair cascade atmospheres surrounding accretion flows are investigated, by developing computer codes to model radiative transfer, scattering, pair production, and pair annihilation. It is found that substantial pair atmospheres may develop above accretion flows which emit even a small fraction of their luminosity as gamma-radiation. The radiation spectrum emitted by the flow may be significantly reprocessed during transit through the atmosphere, leading to interesting observational consequences. The conclusion is reached that under modest and reasonable assumptions, pairs can significantly alter the accretion flows within, and the radiation spectra emitted from, the central engines of active galactic nuclei.

EFFECTS OF ELECTRON-POSITRON PAIRS
ON ACTIVE GALACTIC NUCLEI

by
Bradley Gene Tritz

A thesis submitted in partial fulfillment
of the requirements for the degree

of
Doctor of Philosophy
in
Physics

MONTANA STATE UNIVERSITY
Bozeman, Montana

April 1990

D378
T7399

APPROVAL

of a thesis submitted by

Bradley Gene Tritz

This thesis has been read by each member of the thesis committee and has been found to be satisfactory regarding content, English usage, format, citations, bibliographic style, and consistency, and is ready for submission to the College of Graduate Studies.

3/27/1990
Date

Richard Zumb
Chairperson, Graduate Committee

Approved for the Major Department

3/28/1990
Date

Robert Svenson
Head, Major Department

Approved for the College of Graduate Studies

April 4, 1990
Date

Henry L. Parsons
Graduate Dean

© COPYRIGHT

by

Bradley Gene Tritz

1990

All Rights Reserved

STATEMENT OF PERMISSION TO USE

In presenting this thesis in partial fulfillment of the requirements for a doctoral degree at Montana State University, I agree that the Library shall make it available to borrowers under rules of the Library. I further agree that copying of this thesis is allowable only for scholarly purposes, consistent with "fair use" as prescribed in the U.S. Copyright Law. Requests for extensive copying or reproduction of this thesis should be referred to University Microfilms International, 300 North Zeeb Road, Ann Arbor, Michigan 48106, to whom I have granted "the exclusive right to reproduce and distribute copies of the dissertation in and from microfilm and the right to reproduce and distribute by abstract in any format."

Signature Bruce G. Tritt

Date 4/3/90

TABLE OF CONTENTS

	Page
1. INTRODUCTION	1
The Possibility of Pair Creation in Active Galactic Nuclei	2
Nonthermal Pair Creation	2
Thermal Pair Creation	6
Direct Observation of the 511 KeV Annihilation Line in AGN Spectra	7
The Investigation of Pair Creation in Specific Accretion Models	8
The Present Problem: Detailed Calculations of the Effects of Electron-Positron Pairs in Two-Temperature Accretion Flows; and the Origins, Structure, and Spectral Reprocessing, of Pair Cascade Atmospheres in Active Galactic Nuclei	12
2. PAIR PRODUCTION WITHIN TWO-TEMPERATURE ACCRETION FLOWS	14
Two-Temperature Disk	16
Model with Thermal Pair Production	16
Model with Nonthermal Pair Production	33
Two-Temperature Quasi-Spherical Flow	35
Model with Nonthermal Pair Production	35
Model with Thermal Pair Production	37
Results	38
Two-Temperature Disk	38
Model with Thermal Pair Production	38
Model with Nonthermal Pair Production	45
Two-Temperature Quasi-Spherical Flow	54
3. PAIR CASCADE SHOWER ATMOSPHERE	61
The Accretion Flow as a Photon Source	62
Geometry	62
Spectrum	63
Spatially Distributed Photon and Electron-Acceleration Sources	67

TABLE OF CONTENTS--Continued

	Page
The Shower Approximations	67
The Pair Cascade	72
Solution Method	78
Results	80
Uniform Infinite Radiating Plane	80
Uniform Radiating Spherical Surface	104
Analytic Estimates for Power-Law Distributions	115
Power-Law Evolution in a Pair Cascade	117
Pair Density as a Function of Power-Law Slope	121
Photon Absorption Lengths to Photon-Photon Pair Production	123
4. GENERAL PAIR CASCADE ATMOSPHERE	126
Numerical Treatment of Continuous Variables	128
Elementary Processes	133
Pair Creation	133
Cross Sections and Rates	133
Discretized Pair Creation Spectrum	135
Pair Annihilation	139
Cross Sections and Rates	139
Discretized Annihilation Radiation Spectrum	142
Photon-Electron Scattering	144
Steady-State Photon Distribution	147
Steady-State Electron Distribution	156
Solution Method	159
Results	160
5. CONCLUSIONS	173
REFERENCES CITED	180
APPENDIX--Review of Active Galactic Nuclei	184
Observational Properties	186
Supermassive Black Hole Model	191
Accretion onto a Supermassive Black Hole	195
Jet Formation	199
Grand Somewhat Unified Theory	200

LIST OF FIGURES

Figure	Page
1. Pair abundance, $z=2n_+/n_e$, and disk half-thickness $h_*=h/r$, in the thermal disk for $\alpha_{vis}=0.1$, as a function of radial position r/r_g and dimensionless accretion rate $\dot{m}=\dot{M}/\dot{M}_{Edd}$	40
2. Pair abundance, $z=2n_+/n_e$, and disk half-thickness $h_*=h/r$, in the thermal disk for $\alpha_{vis}=0.5$, as a function of radial position r/r_g and dimensionless accretion rate $\dot{m}=\dot{M}/\dot{M}_{Edd}$	41
3. Radial distribution of electron temperature T_e and ion temperature in the $\alpha_{vis}=0.1$ thermal disk	43
4. Radial distribution of electron scattering optical depth, $\tau_e=n_e\sigma_T h$, and ion optical depth, $\tau_i=n_i\sigma_T h$, in the $\alpha_{vis}=0.1$ thermal disk for $\dot{m}=0.5, 1$, and 2	44
5. Pair abundance z and disk half-thickness h_* in the nonthermal disk as a function of radial position and accretion rate	46
6. Pair abundance z and disk half-thickness h_* in the nonthermal disk as a function of radial position and accretion rate	47
7. Pair abundance z and disk half-thickness h_* in the nonthermal disk as a function of radial position and accretion rate	48
8. Pair abundance z and disk half-thickness h_* in the nonthermal disk as a function of radial position and accretion rate	49

LIST OF FIGURES--Continued

Figure	Page
9. Radial distribution of electron temperature T_e and ion temperature T_i in the nonthermal disk of Fig. 8, for the accretion rate $\dot{m} = 0.5$	52
10. Radial distribution of electron optical depth and ion optical depth, for the nonthermal disk of Fig. 9	53
11. Radial distribution of pair abundance in the nonthermal disk of Figs. 9 and 10	55
12. Critical lines for the nonthermal, quasi-spherical flow, with $\mu=0.3$, and $\epsilon_{th}=0.4$	56
13. Critical lines for the nonthermal, quasi-spherical flow, with $\mu=0.7$, and $\epsilon_{th}=0.4$	57
14. Pair abundances on the critical line in the nonthermal, quasi-spherical flows of Fig. 12 and in the thermal, quasi-spherical flow	59
15. Comparison of critical lines for nonthermal, quasi-spherical flow using differing pair production formulae	60
16. Idealized accretion flow geometries investigated in Chapter 3, and relevant coordinate systems	64
17. Graphical representation of criteria for shower atmosphere	69
18. Thermal pair density profile, and characteristic vertical zones, in typical steady-state pair cascade shower atmosphere above uniform infinite radiating plane	81
19. Radiation spectrum at heights corresponding to points A-G in Fig. 18	82

LIST OF FIGURES--Continued

Figure	Page
20. Variation of thermal pair density N_0 with height h above the plane, for several values of the total number of photon energy bins	94
21. Optical depth to thermal pairs through height h , for several values of the total number of photon energy bins	96
22. Total pair yield of atmosphere for several values of the total number of photon energy bins	98
23. Variation in thermal pair density with height above the plane, for various fractions of total input power going to hard primary component	99
24. Variation in thermal pair density with height above the plane, for various input power-law number density slopes s ($s=\alpha+1$)	100
25. Primary and escaping spectra for $s=3.0$ primary hard input of Fig. 24	102
26. Radiation spectrum at increasing heights above the plane for delta function primary spectra at energies $x_{\text{soft}} = 2.37 \times 10^{-5}$ and $x_{\text{hard}} = 3.8 \times 10^3$	103
27. Variation of thermal pair density with height above the plane for the monochromatic input model of Fig. 26	105
28. Variation of thermal pair density with height above a uniform radiating spherical surface of radii $r_e = 10^{13-18}$ cm	107
29. Escaping spectrum from models of Fig. 28	108
30. Total optical depth of atmosphere forming around $100r_g$ radius accretion cloud surrounding $10^8 M_{\text{sol}}$ black hole as a function of dimensionless accretion rate \dot{m} and energy partitioning f_{hard}	111

LIST OF FIGURES--Continued

Figure	Page
31. Total pair yield of models in Fig. 30	113
32. Mean 2-10 keV X-ray energy index of escaping radiation in models of Figs. 30 and 31	114
33. Escaping radiation energy spectrum from models of Figs. 30-32, for $f_{\text{hard}}=0.1$ and $m=10^{-1}$, 10^0 , 10^1 , 10^2 , and 10^3	116
34. Absorption length to photon-photon pair production for photon of dimensionless energy x , in a photon background corresponding to extrapolation of the $\alpha \approx 2$ power law of line G in Fig. 19, extending from $x=2.37 \times 10^{-5}$ to $x=10^4$	125
35. Convergence of P1+P2 through 14 iterations, as seen in the total electron density in each of the vertical levels $ih=1-4$	162
36. Radiation energy spectrum in each of the vertical levels $ih=1-4$, of photons propagating in directions $\theta < \pi/2$ ($i\theta=1$)	165
37. Radiation energy spectrum in each of the vertical levels $ih=1-4$, of photons propagating in directions $\theta > \pi/2$ ($i\theta=2$)	166
38. Electron number spectrum in each of the vertical levels $ih=1-4$, of electrons propagating in directions $\theta < \pi/2$ ($i\theta=1$)	168
39. Electron number spectrum in each of the vertical levels $ih=1-4$, of electrons propagating in directions $\theta > \pi/2$ ($i\theta=2$)	169
40. Energy spectrum of radiation escaping upward from the atmosphere, and downward from the atmosphere into the accretion flow	172
41. Idealized representative spectra from several prominent classes of AGNs, taken from Phinney (1983)	188
42. Typical pathways of energy dissipation envisioned in AGN accretion flows	197

ABSTRACT

Electron-positron pair creation is investigated in and around accretion flows within active galactic nuclei. First, two-temperature accretion disk models from the 1970's are re-examined, and the effects of pairs on disk structure are calculated. It is found that thermal pair production produces insufficient pairs to greatly affect the disk, but that nonthermal processes produce sufficient pairs to significantly alter flow structure for a wide range of parameters. Then improvements are made upon earlier studies of pair-induced over-cooling of two-temperature spherical accretion flows. It is found that thermal processes produce insufficient pairs to cause over-cooling; however, nonthermal pair production can be an effective cooling agent. Finally, the origin, vertical structure, and radiation spectrum of steady-state pair cascade atmospheres surrounding accretion flows are investigated, by developing computer codes to model radiative transfer, scattering, pair production, and pair annihilation. It is found that substantial pair atmospheres may develop above accretion flows which emit even a small fraction of their luminosity as gamma-radiation. The radiation spectrum emitted by the flow may be significantly reprocessed during transit through the atmosphere, leading to interesting observational consequences. The conclusion is reached that under modest and reasonable assumptions, pairs can significantly alter the accretion flows within, and the radiation spectra emitted from, the central engines of active galactic nuclei.

CHAPTER 1

INTRODUCTION

Among the most intriguing objects in nature are the quasars, the brightest and most distant objects known. In the years since their discovery in the 1960s, astronomers and astrophysicists have come to the realization that these objects are (exceedingly bright) members of a much larger and tremendously varied group: the active galaxies. These galaxies derive their name from the fact that the galactic central core region, called the galactic nucleus, is unusually energetically active. Some measure of appreciation for the extraordinary nature of active galactic nuclei (AGNs) may be gained from a glance at a few of their many spectacular characteristics. For example, the central engine of AGNs (the region where most of the energy is produced) is thought to be some 10 orders of magnitude smaller than the host galaxy as a whole, but can, in the case of bright quasars, outshine the rest of the galaxy by a factor of 10^3 or more. Some AGNs (in what are known as radio galaxies) are seen to propel powerful and remarkably collimated beams of radiation and matter (cosmic jets) which fuel vast radio-emitting structures (radio lobes) a thousand times larger than the host galaxy. And many AGNs exhibit the intriguing ability to radiate more or less uniformly across

some 11 or so decades of frequency, from radio through hard gamma-rays. Many of the prominent spectral features observed in AGNs, along with many theoretical considerations, are consistent with the now almost universally accepted model of an AGN as an accreting supermassive black hole ($M=10^{6-9}M_{\text{sol}}$), residing in the center of the galaxy. If any readers are not familiar with basic AGN theory and observation, they are urged to look over the necessarily brief AGN primer found in the Appendix, before reading the remainder of this paper.

This thesis deals with the effects of electron-positron pairs in AGNs. In this introductory chapter we shall first review simple arguments for the possibility of pair creation in AGNs. We then illustrate the need for studying pairs in AGNs by examining the literature, noting what work has been done in this field and what important lines of inquiry have been inadequately treated. Finally we propose the specific goals we wish to achieve in this thesis, and the methods by which we shall achieve them.

The Possibility of Pair Creation in Active Galactic Nuclei

Nonthermal Pair Creation

Of the AGNs close enough and bright enough to be viewed in γ -rays, many are found to be strong γ -ray emitters (see Appendix). Jelley (1966) was the first to suggest that electron-positron pair creation may occur in AGNs, when γ -rays interact with low energy photons through the quantum electrodynamical process:

$$\gamma + \gamma \rightarrow e^+ + e^- \quad (1.1)$$

The subsequent 15 years or so saw relatively little progress made in investigating the consequences of this possibility. (Notable exceptions include Bonometto and Rees 1971, Herterich 1974, and Cavallo and Rees 1978.) This was due, in large part, to the exceedingly complex physics involved in accelerating particles to energies high enough to produce the γ -radiation necessary for pair creation. (If electrons produced the $h\nu > 100\text{MeV}$ photons observed in some sources, they would have to be ultrarelativistic, with Lorentz factors $\gamma > 10^2$.) Plausible acceleration mechanisms include: strong shock waves, violent magnetic reconnection, and strong electric fields, among others. Interest in the field was renewed when Guilbert, Fabian, and Rees (1983) sidestepped the stubborn issue of acceleration physics and made the obvious but quite fruitful suggestion that much could be learned about AGN behavior by simply modeling particle acceleration as a continuous injection of some high-energy, nonthermal distribution of particles (usually electrons) throughout the emission region. The reasoning was that: (1) the violent variability seen in AGN spectra is a strong indication of chaotic conditions in which at least some particle acceleration is guaranteed; and (2) preliminary studies have shown that most of the mechanisms listed above may produce quite similar power-law particle spectra, so that only a few free parameters (power-law slope, upper and lower energy limits, and total injected power) would be needed to model a generic acceleration mechanism. The newly-accelerated particles would then cool by

Compton upscattering soft photons, by bremsstrahlung emission, or by synchrotron emission, producing γ -radiation in the process, which would then produce pairs.

As Lightman and Zdziarski (1987) point out, acceleration of some electrons to $\gamma \gg 1$ is energetically feasible because typical black hole accretion efficiencies (ratio of luminosity to rest mass accretion rate; see the Appendix) of 10% make available an energy up to $0.1 m_p c^2$ per ionization electron (where m_p is the proton mass and we assume ionized hydrogen is accreting). This scheme is the basis for all "nonthermal" pair creation models considered in this paper.

If a significant fraction of accretion energy is indeed channeled nonthermally to γ -radiation, the criterion for significant pair production is that the source be sufficiently compact and luminous, and the resulting photon densities great enough, so that γ -rays will interact and pair produce instead of escaping from the system. This point may be quantified by a simple, widely used, estimate involving the compactness parameter l (Guilbert, Fabian, and Rees 1983), which is a dimensionless ratio of source luminosity L to source size r :

$$l = \frac{L\sigma_T}{4\pi r m_e c^3}, \quad (1.2)$$

where σ_T is the Thomson cross section. When $l \gg 1$ pair production should be important, with most $\approx 1\text{MeV}$ γ -rays pair producing instead of escaping. When $l \ll 1$ most of these photons will escape and little pair production is expected (see Chapter 2).

When applied to AGN central engines, the compactness parameter tells us on both theoretical and observational grounds that pair production could be important in these objects. Theoretically, following Lightman and Zdziarski (1987) and others, we may rewrite l as product of dimensionless ratios

$$l = (1/2) (m_p/m_e) (L/L_{\text{Edd}}) (r_g/r) , \quad (1.3)$$

where L_{Edd} is the Eddington luminosity (see Appendix), $r_g = 2GM/c^2$ is the Schwartzchild radius of a black hole of mass M , and G is the gravitational constant. For $r \approx 10r_g$, typical of many models, l can exceed unity even for sub-Eddington luminosities.

Observationally, we can estimate the compactness parameter by calculating L from an observed spectrum (the distance to the object must be known), and estimating source size r by the timescale of variability Δt (see the Appendix):

$$R \approx c\Delta t , \quad (1.4)$$

to obtain the observed compactness parameter:

$$l_{\text{obs}} = \frac{L_{\text{obs}} \sigma_T}{4\pi \Delta t_{\text{obs}} m_e c^4} . \quad (1.5)$$

AGN surveys (see Lightman and Zdziarski 1987 for a complete list)

indicate values of l spread fairly uniformly over the interval 10^{-3} to 10^1 , indicating the possible importance of pairs in many AGNs.

If γ -ray production does occur and if the source is sufficiently compact, so that some pairs are produced, there exists the possibility that these pairs will initiate a "nonthermal pair cascade" producing many more pairs. The cascade functions as a positive feedback loop in which the initial relativistic pairs cool by upscattering ambient soft photons to γ -ray energies; these new gamma rays produce a second generation of pairs, which will produce more γ -rays, which will produce more pairs, and so on. Whether these nonthermal processes will be effective or not is a complicated and highly model-dependent question.

Thermal Pair Creation

In contrast to the unequal sharing of energy characterizing nonthermal models, in models of "thermal" pair production, available energy is shared more or less equitably among electrons. Here the importance of pair production depends critically on the electron temperature T_e . If the dimensionless temperature $\theta_e \equiv kT_e/m_e c^2$ is greater than unity, most electrons will be relativistic and readily produce γ -rays, which in turn will produce pairs. If θ_e is not far below unity, the high energy tail of the Maxwell-Boltzmann distribution remains relativistic, and some γ -ray and pair production may result. Many AGN accretion flow models exhibit electron temperatures around $0.1 < \theta_e < 0.5$, indicating the possibility of significant thermal pair production. Whether pairs will indeed be

important is, as was the case for nonthermal models, a difficult and highly model-dependent question.

In addition to photon-photon pair creation, there exist many other pair producing reactions, including photon-electron $\gamma+e\rightarrow e+e^+e^-$, electron-electron $e+e\rightarrow e+e+e^+e^-$, photon-proton $\gamma+p\rightarrow p+e^+e^-$, and so on. The photon-electron cross section is down by roughly a factor of α_f , the fine structure constant, from the photon-photon cross section. The electron-electron cross section is down by an additional factor of α_f , and the corresponding proton rates are even lower. Photon-photon reactions appear always to be the dominant pair creation process in AGNs (see Svensson 1987) because of the large value of its cross section and because particle densities remain too low in most AGN models.

Direct Observation of the 511 KeV Annihilation Line in AGN Spectra

No direct observation of the 511 keV annihilation feature has been reported in extragalactic AGN spectra. This is by no means a death knell to the theory of pairs in AGNs, however. Many theories have been set forth in which the annihilation line is scattered or absorbed on its way out of the source, or is merely intrinsically too weak to be detected. New more powerful detectors slated for the coming few years, and improved modeling (this paper, for example), should shed considerable light on the subject.

We note that an on-again, off-again annihilation line, carrying 10^{37} erg/s (Phinney 1983), has been observed coming from our Galactic center. Our Galactic nucleus has long been suspected to be weakly

active, and if these observations are confirmed, we will have the first (but only) direct evidence of pairs in AGNs.

The Investigation of Pair Creation in Specific Accretion Models

Current theory tells us that matter accreting onto a black hole may assume any number of geometrical forms. However, if any angular momentum is originally present as mass is fed into the system from great distances, or if the hole is spinning and the Lense-Thirring effect is in operation, the accretion flow should settle into some sort of accretion disk in the region near the hole (see the Appendix). It is in this central portion of the accretion flow where most of the gravitational potential energy is released. Any atmosphere of matter or radiation present in the space surrounding the flow (above or below the disk) may scatter, absorb, or re-emit portions of the primary spectrum emitted from the accretion flow, constituting so-called spectral reprocessing. What we see through our telescopes and detectors is the reprocessed primary spectrum. Any successful model of AGN central engines must therefore address both accretion flow and atmosphere. We now consider specific important AGN flow and atmosphere models in which the effects of pair creation could be great, but for which this possibility has not been adequately investigated, or investigated at all.

A quick survey of conventional wisdom tells us that accretion flows can surround themselves with at least five fundamentally different kinds of atmospheres : (1) radiation pressure driven winds, in which intense radiation from the inner regions of the flow blows

matter (pairs or otherwise) outward (Leighly 1990); (2) evaporative/diffusive atmospheres, in which particles with sufficiently high velocities may overcome any (as yet unknown) containment forces and "evaporate" from the surface of the flow (Shakura and Sunyaev 1973); (3) magneto-coronal atmospheres, in which shear amplified magnetic fields induce an instability by which matter in magnetic flux tubes becomes buoyant and rises up out of the flow, perhaps resulting in magnetic flares, prominences, and a high temperature corona much like those seen on the sun (Galeev, Rosner and Vaiana 1979); (4) cosmic jets, in which a complex of ordered magnetic and electric fields tap into the rotational energy of the (spinning) black hole and propel radiation and/or matter out more or less along the rotational axis (Phinney 1983; Burns and Lovelace 1982); and (5) pair cascade atmospheres, in which γ -rays, emitted from the flow, or produced by, say, high temperature electrons in a mageto-corona, initiate a pair cascade which populates the atmosphere with pairs (see comments in Svensson 1985).

Of these five models, only pair winds and jets have received a great deal of treatment (see the above references). We turn our attention to one of the neglected areas, the pair cascade atmosphere. If the assertion by Guilbert, Fabian, and Rees (1983) is true, and AGN accretion flows are indeed natural γ -ray emitters, pair production should not only occur inside the flow, but outside as well, and some sort of pair atmosphere should form. This has yet to be investigated in any detail at all. The task is a difficult one: the situation is intrinsically three-dimensional; the outer limits and

spatial structure of the atmosphere are a priori unknown; the atmosphere may be optically thin, so that radiative transfer will link together all regions of the atmosphere; the atmosphere depends critically on the emission spectrum and geometry of the accretion flow, which in turn may be affected by the atmosphere; and several physical processes (scattering, pair creation, pair annihilation, radiative transfer, particle transfer, ect.) are concurrently at work.

A survey of the literature reveals a large number of accretion disk models that have been proposed over the last twenty years or so. Many of these are variations on one or the other of the two most widely referenced models, the cool, optically thick, geometrically thin disk of Shakura and Sunyaev (1973), and the hot, optically thin, geometrically thin, two-temperature disk of Shapiro, Lightman, and Eardley (1976). These two models were originally formulated as pair-free, without taking into account any possible pair creation. Let us turn our attention to the two-temperature disk. As we note in the Appendix, two-temperature accretion flows are predicted for a large range of flow conditions in AGNs. The presence of pairs could significantly alter the state of matter and radiation within the disk, affecting disk structure and emission spectrum. Before the present work, the only attempt to calculate equilibrium pair densities in the two-temperature disk was by Liang (1979), who noted correctly that the high electron temperatures in the pair free model ($T_e=10^{9-10}K$) indicated pairs might be important. His results, which showed that thermal pair production was very important, with the density of pairs greatly exceeding the density of protons, were seriously

questioned however, when Svensson (1985) and others found his methods to suffer many critical flaws. Also, no investigations into nonthermal pair production have been conducted on this or any other disk whatsoever.

Inflated accretion flows (spherical or quasi-spherical geometry) have been investigated somewhat more thoroughly for the effects of pairs than have the disks (see, for example: Svensson 1987; Lightman and Zdziarski 1987; Done and Fabian 1989; Fabian et al. 1986; and Begelman, Sikora, and Rees 1987). As was the case with the disks, there are many models of spherical accretion from which to choose, but we shall again limit discussion in the present paper to two-temperature class of flows. It is of course desirable that two-temperature flows be investigated for the effects of pairs in both their thin disk and inflated limits. About the only work done in the spherical limit was the pioneering paper of Begelman, Sikora, and Rees (1987), who used crude estimates of both thermal and nonthermal pair creation rates to estimate the effects of pairs on the thermal instability to possible collapse of the innermost regions of the ion pressure supported flow due to the overcooling of ions by pairs through Coulomb collisional energy transfer. The collapse, and particularly the size of the collapsed region, influence heavily the geometry and primary spectrum of the flow (see Begelman, Sikora, and Rees 1987). A revisitation of the work of Begelman, Sikora, and Rees (1987) utilizing more detailed calculations of pair creation rates is needed.

The Present Problem: Detailed Calculations of
the Effects of Electron-Positron Pairs in Two-
Temperature Accretion Flows; and the Origins,
Structure, and Spectral Reprocessing of Pair
Cascade Atmospheres in Active Galactic Nuclei

In this thesis we propose to remedy several important deficiencies in the development of accurate, self-consistent models of AGN central engines in the following manner. (1) We will investigate the effects of pairs on the classic two-temperature disk model of Shapiro, Lightman, and Eardley (1976). We will do this by improving the original pair free model, generalizing it to accommodate the presence of any pairs, developing accurate thermal and nonthermal models of pair creation within the disk, and numerically solving the model to determine the nature and extent of the effects of pairs. (2) We will improve upon the pioneering work of Begelman, Sikora, and Rees (1987) by using more accurate treatments of both thermal and nonthermal pair production to determine the nature and extent of the effects of pairs on the over-cooling and collapse instabilities in two-temperature quasi-spherical accretion flows. (3) We will develop detailed numerical models of pair cascade atmospheres. Computer codes will be developed which, for any primary spectrum emitted by an accretion flow, will numerically solve for the three-dimensional structure of, and the spectral reprocessing by, the resulting atmosphere. Two distinct models will be developed. The first is a "pair cascade shower atmosphere," which employs many simplifying

assumptions. The second, called "the general cascade atmosphere," is a more accurate model with many simplifying assumptions relaxed. We will make primitive comparisons with observation where appropriate and possible.

CHAPTER 2

PAIR PRODUCTION WITHIN TWO-TEMPERATURE ACCRETION FLOWS

Two-temperature accretion flows, in which protons maintain higher temperatures than electrons, are an important class of accretion flows, and are predicted to be present in many AGN central engines (see the Appendix). To investigate the effects of pairs on the structure and properties of two-temperature accretion flows, we adopt two extreme cases, a disk and quasi-spherical approach, which together, hopefully, would give some realistic insight to the actual physical situation. In disk accretion, the two-temperature hot region should be geometrically thick (see Appendix). However, a realistic model of such an inflated torus is non-existent. Therefore, we adopt the hot two-temperature thin disk model of Shapiro, Lightman, and Eardley (1976), the best available at the moment. They estimate that the thin disk model should remain acceptably accurate (to within a factor of about 2) even when the half-thickness h of the disk grown to the order of the radial distance r from the center of the disk: $h \sim r$. Our results should be accurate within the region $h < r$ and at least qualitatively valid up to moderately inflated states, $h \sim r$, at which point spherical or quasi-spherical inflow has become appropriate (White and Lightman 1989). In our quasi-spherical model

we adopt the approach of Begelman, Sikora and Rees (1987) where the effect of the angular momentum is taken into account by allowing the infall velocity v to be less than the free fall velocity by a factor μ . This crudely models accretion as matter spirals, rather than directly falls, in toward the black hole. The quasi-spherical results should be valid in geometries ranging from moderately thick tori, $h \sim r$, to essentially spherical inflow, $h > r$.

If the electron temperature is sufficiently high, bremsstrahlung could become an important cooling mechanism (see White and Lightman 1989). However, we adopt the view that the observed broad-band composite spectra of continuum radiation from Seyfert nuclei and typical radio-quiet quasars are more naturally explained by unsaturated Comptonization of soft photons by energetic electrons (Tsuruta 1988), and thus we do not discuss bremsstrahlung models in this paper. (See, however, White and Lightman 1989 for discussion of *one*-temperature bremsstrahlung disks which do not contradict the observational absence of a Wien hump in low luminosity Seyferts, for instance, but do appear to be inconsistent with gamma-ray observations and observed power-law slopes.) The soft photons may refer, e.g., to the UV bump observed in many of these objects or infrared emission through cyclotron higher harmonics (Takahara and Tsuruta 1982). When Comptonization is unsaturated, the outcoming radiation has a power-law spectrum (e.g., Shapiro, Lightman and Eardley 1976). Our thermal models are, therefore, constructed to satisfy the important constraint that the energy slope α of the

observed power-law X-ray spectra is $\sim 0.3-1$ for AGNs in general, and ~ 0.7 for Seyfert 1s in particular.

Within our two-temperature accretion flows near a black hole the proton temperature is comparable to its virial value, which is $\sim 10^{11}\text{K}$ to 10^{12}K , while the expected electron temperature of around 10^9K is of the order of its rest mass energy (Shapiro, Lightman and Eardley 1976). Under such high temperatures the thermal production of electron-positron pairs could be important. On the other hand, it has been pointed out that pairs can be produced even more efficiently through a nonthermal process (e.g. see Rees 1984, Guilbert, Fabian and Rees 1983, Fabian et al. 1986). These authors argued that in the environment of the accretion flows near a black hole some fraction of electrons could be accelerated effectively to highly relativistic energies through shocks, magnetic reconnections, etc., and these electrons will produce pairs through a cascade process, described in detail in Chapter 3. Therefore, in our work we consider both thermal and nonthermal pair production, in both our disk and quasi-spherical models.

Two-Temperature Disk

Model with Thermal Pair Production

We refer the reader to the pair-free disk structure equations of Shapiro, Lightman, and Eardley (1976). Taking $n_e = n_i + 2n_+$ to be the total electron density (ionization electrons plus pairs), where n_i is the ion (proton) density, and n_+ is the positron (=pair) density, we accommodate the presence of pairs by formally including the pair

contributions to the gas pressure and mass density in the equation of state and the condition of hydrostatic equilibrium:

$$P = n_e k T_e + n_i k T_i, \quad (2.1)$$

$$P/h = (n_e m_e + n_i m_p)(GM/r^3)h. \quad (2.2)$$

Here T_e is the electron (and positron) temperature; T_i the ion (proton) temperature; P the pressure; M the mass of the accreting black hole ($10^7 M_{\text{sol}}$ for models presented in this chapter); and h the disk half-thickness at radius r where $h \ll r$ is the thin disk criterion. We ignore the radiation pressure contribution to the total pressure P in equation (2.1). Radiation pressure will become important at super-Eddington accretion rates (see Appendix) and should be considered. However, at such high accretion rates we find that the flow inflates considerably (see "Results" section of this chapter) and our thin disk analysis no longer holds. Equation (2.2) represents the balance between the vertical component of the gravitational force $F_g = (GM\rho/r^2)(h/r)$ and the pressure force $F_p = P/h$. Here we have invoked the thin disk assumption $h \ll r$ to use the small angle approximation $h/(r^2+h^2)^{1/2} \approx h/r$. The electron contributions to the pressure and density will be important in pair-dominated plasmas, but remain small when pair densities are low. The equation of conservation of angular momentum remains unaltered from Shapiro, Lightman, and Eardley (1976), (shear stress)(area) r =(angular momentum transfer):

$$\alpha_{\text{vis}} P (2\pi r \cdot 2h) \dot{r} = (GMr)^{1/2} \dot{M} \Phi . \quad (2.3)$$

Here \dot{M} is the mass accretion rate; α_{vis} the so-called "viscosity parameter" satisfying the usual viscosity law: (shear stress) = $\alpha_{\text{vis}} P$, with $0.01 < \alpha_{\text{vis}} < 1$ (see Shakura and Sunyaev 1973 and Shapiro, Lightman and Eardley 1976); and $\Phi(r) = 1 - (6GM/c^2/r)^{1/2}$, which reflects the absence of viscous stresses at the disk's inner edge where matter leaves its quasi-Keplerian orbit and quickly falls toward the horizon (see the Appendix; Shapiro and Teukolsky 1983).

We use the expression of Stepney and Guilbert (1983) for the collisional energy transfer rate from the hot ions to the cooler electrons, which is considerably more accurate than the treatment in Shapiro, Lightman, and Eardley (1976),

$$\begin{aligned} \dot{u}_{ep} &= \frac{3m_e}{2m_p} n_e n_i \sigma_T \ln \Lambda \frac{k(T_i - T_e)}{K_2(1/\theta_e) K_2(1/\theta_i)} \\ &\times \left[\frac{2(\theta_e + \theta_i)^2 + 1}{\theta_e + \theta_i} K_1 \left(\frac{\theta_e + \theta_i}{\theta_e \theta_i} \right) + 2K_0 \left(\frac{\theta_e + \theta_i}{\theta_e \theta_i} \right) \right] \end{aligned} \quad (2.4)$$

where $\theta_e = kT_e/(m_e c^2)$, $\theta_i = kT_i/(m_p c^2)$, $\ln \Lambda \approx 25$, σ_T is the Thomson cross section, and K_i is the modified Bessel function of the second kind of order i . This expression results from integrating the Rutherford differential cross section for coulomb collisions over relativistic Maxwell-Boltzmann distributions using relativistically correct two-body

reaction rates formalism (see Weaver 1967). Taking the low-temperature limit $1 \gg \theta_e \gg \theta_i$ (involving asymptotic expansions of the $K_i(z)$; see Abramowitz and Stegun 1965), the approximate form of equation (2.4) used by the above-mentioned studies is recovered:

$$\dot{u}_{ep} \propto (T_i - T_e) T_e^{-3/2}.$$

Ion energy balance is accomplished by matching ion cooling, equation (2.4), to viscous heating of the disk at all r :

$$\dot{u}_{ep} = \dot{u}_{vis}, \quad (2.5)$$

where shear stresses heat the disk at the rate (see Shapiro, Lightman, and Eardley 1976)

$$\dot{u}_{vis} = 3/(8\pi) \dot{M} (GM/r^3) \Phi / h. \quad (2.6)$$

In order to calculate pair production from photon-photon and photon-electron interactions the photon spectrum within the disk must be specified (the electron distribution will be addressed shortly). However, the radiation spectrum depends upon the particular electron cooling mechanisms at work. Facilitating comparison with the original pair-free disk model of Shapiro, Lightman, and Eardley (1976), we follow these authors and assume the existence of a copious source of soft photons (UV or softer) which are Compton upscattered (Comptonized) off the hot relativistic electrons and subsequently escape from the disk. This is the so-called "Comptonized soft-photon" model. This approach has a number of commendable features.

First the form of the Comptonized spectrum depends very weakly, or not at all, upon the spectral shape, mean photon energy, and strength, of the soft source (Lightman and Zdziarski 1987). This eliminates a build-up of free parameters needed to specify the soft source. Secondly extensive monte carlo and analytical work of others (Pozdnyakov, Sobol, and Sunyaev 1977 and 1979; Zdziarski 1985; Sunyaev and Titarchuk 1980) has provided accurate, convenient, analytic fits to Comptonized soft spectra in idealized geometries. Thirdly unsaturated Comptonization easily provides the UV-X-ray power-law characteristics of most Seyfert 1 spectra (see Appendix). Finally a soft UV source would be a natural consequence of any cooler (10^{4-5}K) gas clouds in and around the hot (10^{9-12}K) disk we are considering. Alternative electron cooling mechanisms (bremsstrahlung and Comptonized bremsstrahlung) have been investigated by White and Lightman (1989).

The Comptonization process proceeds as follows. Soft photons of initial (dimensionless) energy x_1 are repeatedly upscattered by thermal electron of (dimensionless) temperature θ_e until either they escape from the disk or reach energies of $x \approx \theta_e$, after which the process saturates and further scatterings result in no net energy transfer between photon and electron populations. Saturation is marked by the development of thermal population of photons, the Wien spectral component.

Those photons not reaching thermal energies before escape will in general form a power-law distribution, as we now demonstrate. Photons far below the electron thermal energy ($x_1 \ll \theta_e$) will undergo a

mean energy amplification given by $A=1+4\theta_e+16\theta_e^2$. This popular formula conveniently combines the nonrelativistic ($\theta_e \ll 1$) result $A_{nr}=1+4\theta_e$ with that in the extreme relativistic ($\theta_e \gg 1$) case $A_{er}=16\theta_e^2$ in a smooth manner. We let τ_e be the optical depth to Thomson scattering ($\tau_e \equiv n_e \sigma_T h$) and note $e^{-\tau_e}$ is roughly the mean probability of escape per scattering. The mean probability that a photon anywhere within the system will scatter rather than directly escape is $P_{sct}=1-e^{-\tau_e}$. If the system is optically thin, $\tau_e < (\text{a few})$, the probability of exactly k scatterings before escape $P_{sct}^k e^{-\tau_e}$ can be approximated as simply P_{sct}^k . After k scatterings the photon energy has risen to $x=x_1 A^k$, producing a photon spectrum (for $x < \theta_e$): $L(x)=L(x_1)P_{sct}^k$. We can rewrite P_{sct}^k as follows:

$$\begin{aligned} P_{sct}^k &= \left(A^{\log P_{sct} / \log A} \right)^k \\ &= \left(\frac{x}{x_1} \right)^{\log P_{sct} / \log A} \end{aligned} \quad (2.7)$$

and obtain the power law $I(x) \propto x^{-\alpha}$ with energy index

$$\alpha = \frac{-\log P_{sct}}{\log A} \quad (2.8)$$

This useful result was first shown by Y.B. Zeldovich and numerically verified by Pozdnyakov, Sobol, and Sunyaev (1977) and many others.

We can therefore safely treat the radiation field within the disk as a superposition of a power law and a Wien component, following Zdziarski (1985):

$$n(x) = \frac{1}{2}N_p(x/\theta_e)^{-\alpha}(e^{-x/\theta_e})/x + \frac{1}{2}N_w(x/\theta_e)^3(e^{-x/\theta_e})/x \quad (2.9)$$

where $x=hc/(m_e c^2)$ is the dimensionless photon energy, α is the energy index of the power-law portion of the spectrum, N_w is the total density of Wien photons, and N_p is related to the power-law photon density (Svensson 1984). Using numerical monte carlo calculations, Zdziarski (1985) has found that equations (2.8) and (2.9) together are quite accurate if the relative strength of the two spectral components is given by the fitting formula:

$$N_w/N_p = [\Gamma(\alpha)/\Gamma(2\alpha+3)]P_{\text{sct}} , \quad (2.10)$$

where Γ is the Euler gamma function.

The power-law index α is fixed by observation in our models (a free parameter, in other words). Many Seyfert 1 spectra exhibit $\alpha \approx 0.7$ in the X-ray region (Mushotzky 1984, and the Appendix) and we set $\alpha=0.7$ for models presented in this chapter. Equation (2.8) is therefore a constraint between τ_e and θ_e .

We normalize the photon spectrum by equating, at each radius, radiative luminosity to viscous heating:

$$\dot{u}_{\text{vis}} = u_{\text{rad}}/[\max(1, \tau_e)h/c] , \quad (2.11)$$

where $u_{\text{rad}} = (3/2)kT_e N_W + (1/2)\Gamma(1-\alpha)kT_e N_p$ is the photon energy density within the disk, obtained by integrating equation (2.9).

Pair equilibrium requires the balance of pair creation, annihilation, and inflow:

$$0 = \dot{n}_+ = \dot{n}_+^{\text{cre}} + \dot{n}_+^{\text{ann}} + \dot{n}_+^{\text{inf}} . \quad (2.12)$$

We take annihilation to proceed at the rate (see Svensson 1982):

$$\dot{n}_+^{\text{ann}} = -(3/32)g_a \sigma_T c (n_e - n_+) (n_e + n_+) , \quad (2.13)$$

with:

$$g_a = [1 + 2\theta_e^2 / \ln(1.12\theta_e + 1.3)]^{-1} . \quad (2.14)$$

This is a convenient and quite accurate fit to the exact result. (The exact rate is obtained by integrating the annihilation cross section, given in Chapter 4, over a relativistic Maxwell-Boltzmann distribution of electrons and positrons). If pairs are advected inward with the flow of the ions, then the disk geometry casts pair inflow into the form:

$$\dot{n}_+^{\text{inf}} = (\text{hr})^{-1} \frac{d}{dr} (\text{hr} v_{\text{acc}} n_+) , \quad (2.15)$$

where:

$$v_{\text{acc}} = \dot{M} / [4\pi r (n_p m_p + n_e m_e)] \quad (2.16)$$

is the net inward velocity of accretion, obtained from examining mass conservation.

Pairs will be produced through photon-photon interactions $\gamma + \gamma \rightarrow e^+ e^-$ and photon-electron interactions $\gamma + e \rightarrow e + e^+ e^-$. All other pair producing reactions (electron-electron, along with all proton and three-body reactions) are neglected (see Svensson 1984 and Liang 1979). The division of the photon spectrum into two components, equation (2.9), requires five pair production rates to be found : interactions between (1) power-law photons, (2) power-law and Wien photons, (3) Wien photons, (4) power-law photons and electrons and (5) Wien photons and electrons:

$$\dot{n}_{\ddagger}^{\text{cre}} = \dot{n}_{\ddagger}^{\text{PP}} + \dot{n}_{\ddagger}^{\text{PW}} + \dot{n}_{\ddagger}^{\text{WW}} + \dot{n}_{\ddagger}^{\text{Pe}} + \dot{n}_{\ddagger}^{\text{We}} . \quad (2.17)$$

The utility of the fit in equation (2.9) is presently seen by the fact that we may analytically reduce all three photon-photon rates down to the same single integral over the cross section, and the two photon-electron rates down to a (different) single integral over the cross section.

We shall first derive the $\gamma + \gamma$ pair creation rate, $\dot{n}_{\ddagger}^{\text{PP}}$ from the interaction between two isotropic populations:

$$n_1(x_1) = \frac{1}{2} N_1 (x_1/\theta_1)^{-\alpha_1} e^{(-x_1/\theta_1)} / x_1 \quad (2.18)$$

and:

$$n_2(x_2) = \frac{1}{2}N_2 (x_2/\theta_2)^{-\alpha_2} e^{(-x_2/\theta_2)/x_2} . \quad (2.19)$$

The probability per unit time of absorption by population 2 photons for a photon from population 1 with energy x_1 is

$$\frac{d\tau(x_1)}{dt} = \int_0^\pi \int_0^\infty \sigma_{\gamma\gamma}(s) c(1-\cos\theta) \frac{1}{2}\sin\theta n_2(x_2) dx_2 d\theta , \quad (2.20)$$

where θ is the collision angle between x_1 and x_2 , $\frac{1}{2}\sin\theta n_2(x_2)dx_2 d\theta$ is the differential population 2 photon density, $c(1-\cos\theta)$ is the relative velocity of x_2 along the direction of motion of x_1 , and $\sigma_{\gamma\gamma}(s)$ is the total pair production cross section, which is a function of the center-of-momentum (c.m.) frame energy γ of either photon (see Gould and Schröder 1967):

$$\sigma_{\gamma\gamma}(s) = \frac{1}{2}\pi r_0^2 (1-\beta^2) \left((3-\beta^4) \ln \frac{1+\beta}{1-\beta} - 2\beta(2-\beta^2) \right) . \quad (2.21)$$

Here $\beta=(1-\gamma^{-2})^{1/2}$ is the c.m. velocity of either electron, $s=\gamma^2$, $2s=x_1x_2(1-\cos\theta)$, and r_0 is the classical electron radius. Switching integration variables from θ to s yields:

$$\frac{d\tau(x_1)}{dt} = \frac{c\pi r_0^2}{x_1^2} \int_0^\infty dx_2 \frac{n_2(x_2)}{x_2^2} \int_0^{x_1 x_2} ds \frac{2\sigma \gamma(s)}{\pi r_0^2} \quad (2.22)$$

Defining the inner integral as the dimensionless function $\varphi(x_1 x_2)$ (see Gould and Schröder 1967) and noting the total creation rate will be the integral of equation (2.22) over $dn_1(x_1)$, we have the symmetric form

$$\dot{n}_+ \gamma = c\pi r_0^2 \int \int \frac{\varphi(x_1 x_2)}{x_1^2 x_2^2} n_1(x_1) n_2(x_2) dx_1 dx_2 \quad (2.23)$$

Inserting the spectral functions of equations (2.18) and (2.19) into equation (2.23), defining $s_0 = x_1 x_2$ and switching variables from x_2 to s_0 we have

$$\begin{aligned} \dot{n}_+ \gamma &= c\pi r_0^2 \frac{N_1 N_2}{4} \int_1^\infty ds_0 \varphi(s_0) s_0^{(-3-\alpha_2)} \theta_1^{\alpha_1} \theta_2^{\alpha_2} \\ &\times \int_0^\infty dx_1 x_1^{(-1-\alpha_1-\alpha_2)} e^{(-x_1/\theta_1 - s_0/(x_1 \theta_2))} \quad (2.24) \end{aligned}$$

The x_1 integral can be found in Gradshteyn and Ryzhik (1980) as #3.471.9. Inserting a factor $1/(1+\delta_{12})$ to avoid double counting in the

case populations 1 and 2 are the same population, we arrive at

$$\dot{n}_+^{\gamma\gamma} = (3/16) \sigma_{Tc} \frac{N_1 N_2}{1 + \delta_{12}} (\theta_1 \theta_2)^{(\alpha_1 + \alpha_2)/2} \\ \times \int_1^{\infty} ds_0 \varphi(s_0) s_0^{-(6 + \alpha_1 + \alpha_2)/2} K_{\alpha_2 - \alpha_1} \left(\frac{4s_0}{\theta_1 \theta_2} \right)^{1/2} \quad (2.25)$$

This result was found by Svensson (1984). Here \dot{n}_+^{PP} is obtained when $\alpha_1 = \alpha_2 = \alpha$, $N_1 = N_2 = N_p$, $\theta_1 = \theta_2 = \theta_e$ and $\delta_{12} = 1$; \dot{n}_+^{PW} is obtained when $\alpha_1 = \alpha$, $\alpha_2 = -3$, $N_1 = N_p$, $N_2 = N_w$, $\theta_1 = \theta_2 = \theta_e$ and $\delta_{12} = 0$; and \dot{n}_+^{WW} is obtained when $\alpha_1 = \alpha_2 = -3$, $N_1 = N_2 = N_w$, $\theta_1 = \theta_2 = \theta_e$ and $\delta_{12} = 1$. An accurate analytic fit to $\varphi(s_0)$ is found in Gould and Schröder (1967), after correcting a critical misprint. Equation (2.25) is integrated numerically for various θ_e and the results stored for tabular interpolation.

We next calculate the pair production rate from interactions between an isotropic Maxwell-Boltzmann electron (and positron) distribution at temperature θ_1

$$n_1(p_1) = N_1 p_1^2 \frac{e^{-(p_1^2 + 1)^{1/2}} / \theta_1}{\theta_1 K_2(1/\theta_1)} \quad (2.26)$$

and the isotropic photon distribution given by equations (18) or (19):

$$n_2(p_2) = \frac{1}{2} N_2 (p_2/\theta_2)^{-\alpha_2} e^{(-p_2/\theta_2)/p_2} . \quad (2.27)$$

Here p_1 and p_2 are the electron and photon momenta respectively. (We suppress factors of c and $m_e c^2$ throughout, so that the dimensionless energy-momentum relationships read $x=p$ for photons and $\gamma^2=p^2+1$ for electrons.) We will first calculate the differential reaction rate dR ($\text{cm}^{-3} \text{sec}^{-1}$) in a beam of electrons with density dn_1 and energy $\gamma_1=(1-\beta_1^2)^{1/2}$ colliding with a photon beam of density dn_2 and momentum p_2 , where the collision angle is θ . We temporarily switch to the electron rest frame (signified here by primed quantities) where the physics is much simpler and calculate the (Lorentz-invariant) rate

$$dR = dR' = dn'_1 dn'_2 c \sigma_{\gamma e}(p'_2) , \quad (2.28)$$

where

$$p'_2 = p_2 \gamma_1 (1 - \beta_1 \cos \theta) . \quad (2.29)$$

is the rest-frame photon momentum. Here c is the relative velocity and $\sigma_{\gamma e}(p'_2)$ is the total photon-electron pair creation cross section. Accurate analytic fits to $\sigma_{\gamma e}(p'_2)$ are calculated by Haug (1981) and presented by Stepney and Guilbert (1983). Invariance of the dot product of the four-vector currents $j_1=n_1(1,\beta_1\hat{v}_1)$ and $j_2=n_2(1,\hat{v}_2)$ yields the density transformation:

$$dn'_1 dn'_2 = dn_1 dn_2 (1 - \beta_1 \cos\theta) = dn_1 dn_2 \frac{p'_2}{p_2 \gamma_1}, \quad (2.30)$$

where the second equality follows from equation (2.29). We now substitute equation (2.30) into equation (2.28) and integrate over the (isotropic) distributions to obtain the total rate

$$\dot{n}_4^{\gamma e} = \frac{1}{2}c \int \int \int n_1(p_1) n_2(p_2) \frac{p'_2}{p_2 \gamma_1} \sigma_{\gamma e}(p'_2) dp_1 dp_2 du, \quad (2.31)$$

where $u = \cos\theta$ and the factor of 1/2 removes a spurious factor of 2 introduced by the u integration. We change variables from u in favor of p'_2 via equation (2.29)

$$\begin{aligned} \dot{n}_4^{\gamma e} &= \frac{1}{2}c \int_4^\infty dp'_2 \sigma_{\gamma e}(p'_2) p'_2 \\ &\times \int_0^\infty dp_2 \frac{n_2(p_2)}{p_2^2} \int_{p_1^{\min}}^\infty dp_1 \frac{n_1(p_1)}{\gamma_1^2 \beta_1}, \end{aligned} \quad (2.32)$$

where:

$$p_1^{\min} = \frac{1}{2} \left| \frac{p'_2}{p_2} - \frac{p_2}{p'_2} \right|. \quad (2.33)$$

The lower limit to the p'_2 integration represents the reaction

threshold, which defines a minimum energy state in the c.m. frame. Threshold for this reaction occurs when all three electrons (incident plus created pair) are at rest in the c.m. frame after the interaction, giving a total c.m. energy of $E_{\text{cm}}=3$. Before the interaction this energy is carried by the incident photon x_{cm} and the incident electron, whose c.m. energy is determined by the requirement that the incident momenta of the photon and electron must be the same. That is,

$$E_{\text{cm}} = 3 = x_{\text{cm}} + (x_{\text{cm}}^2 + 1)^{1/2} . \quad (2.34)$$

This expression gives the c.m. photon threshold energy $x_{\text{cm}} = \frac{4}{3}$. The Lorentz factor γ_{rel} of the relative velocity β_{rel} between the c.m. and electron rest frames is

$$\gamma_{\text{rel}} = (1 + x_{\text{cm}}^2)^{1/2} , \quad (2.35)$$

which gives $\gamma_{\text{rel}} = \frac{5}{3}$ and $\beta_{\text{rel}} = \frac{4}{5}$. We then Lorentz transform x_{cm} back to the rest frame

$$x_{\text{rest}} = x_{\text{cm}} \gamma_{\text{rel}} (1 + \beta_{\text{rel}}) , \quad (2.36)$$

and obtain the threshold value $x_{\text{rest}} = \frac{4}{3} \frac{5}{3} (1 + \frac{4}{5}) = 4$.

The lower limit p_1^{min} to the p_1 integration is found by examining equation (2.29) for the smallest value of $p_1 (= \gamma_1 \beta_1)$ for any choice of p_2 , p_2' and $\cos\theta$. If p_1 is considered a function of the

variables $p'_2/p_2 \equiv a$ and $\cos\theta \equiv u$, it is immediately obvious that for any $a < 1$ the minimum for p_1 occurs when $u = +1$, yielding $p_1^{\min} = (a^{-1} - a)/2$. For any $a > 1$ the minimum occurs when $u = -1$, yielding $p_1^{\min} = (a - a^{-1})/2$. These two results are equivalent to p_1^{\min} given in equation (2.33).

Substituting the spectral shapes of $n_1(p_1)$ and $n_2(p_2)$ from equations (2.26) and (2.27) into equation (2.32) gives

$$\begin{aligned} \dot{n}_+ \gamma_e &= \frac{c}{2} \int_4^\infty dp'_2 \sigma_{\gamma_e}(p'_2) p'_2 \\ &\times \int_0^\infty dp_2 \frac{1}{2} N_2 (p_2/\theta_2)^{-\alpha_2} e^{-(p_2/\theta_2)/p_2^3} \\ &\times \int_{p_1^{\min}}^\infty dp_1 N_1 p_1^2 \frac{e^{-(p_1^2+1)^{1/2}/\theta_1}}{\theta_1 K_2(1/\theta_1) \gamma_1^2 \beta_1} \end{aligned} \quad (2.37)$$

The p_1 integral is trivial (writing p_1 and β_1 as functions of γ_1) and produces:

$$\dot{n}_+ \gamma_e = \frac{c N_1 N_2 \theta_2^{\alpha_2}}{4 K_2(1/\theta_1)} \int_4^\infty dp'_2 \sigma_{\gamma_e}(p'_2) p'_2$$

$$\times \int_0^{\infty} dp_2 p_2^{(-\alpha_2-3)} e^{-[\theta_2^{-1} + (2\theta_1 p_2')^{-1}]p_2 - p_2'/(2\theta_1 p_2)} \quad (2.38)$$

The p_2 integration is done with the help of integral #3.471.9 in Gradshteyn and Ryzhik (1980), and we obtain the final result (changing the dummy variable to x for ease of notation):

$$\begin{aligned} \dot{n}_+^{\gamma e} &= \frac{cN_1 N_2}{2K_2(1/\theta_1)} \theta_2^{\alpha_2} \int_4^{\infty} dx \sigma_{\gamma e}(x)x \left(\frac{x}{(2\theta_1/\theta_2)+(1/x)} \right)^{-(2+\alpha_2)/2} \\ &\times K_{-2-\alpha_2} \left[2 \left(\frac{x}{2\theta_1} \left[\frac{1}{\theta_2} + \frac{1}{2x\theta_1} \right] \right)^{1/2} \right]. \end{aligned} \quad (2.39)$$

where \dot{n}_+^{Pe} results when $N_1=n_e$, $\theta_1=\theta_2=\theta_e$, $\alpha_2=\alpha$, and $N_2=N_p$; and \dot{n}_+^{We} results when $N_1=n_e$, $\theta_1=\theta_2=\theta_e$, $\alpha_2=-3$, and $N_2=N_w$. This result was found by Zdziarski (1985). Equation (2.39) is integrated numerically for various θ_e and the results stored for tabular interpolation.

Equations (2.1)-(2.3), (2.5), (2.8), and (2.10)-(2.12) constitute the eight equations necessary for the solution of the eight variables describing the thermal disk at any radius r : n_e , n_i , T_e , T_i , P , h , N_p , and N_w . Model parameters to be specified are: M , $\dot{m} \equiv \dot{M}/\dot{M}_{\text{Edd}}$, α_{vis} , and α . Here, $\dot{M}_{\text{Edd}}c^2$ is the Eddington luminosity. Results are given in the "Results" section of this chapter.

Model with Nonthermal Pair Production

We adopt the scheme (see, e.g. Lightman and Zdziarski 1987) whereby some fraction ϵ_e of the power developed through viscous dissipation within the disk goes to the acceleration of some electrons to relativistic energies ($\gamma \gg 1$). The γ -rays produced as these relativistic electrons quickly cool will produce pairs, which, in turn, cool and produce additional γ -rays. Depending upon conditions, several generations of pairs may be produced in a nonthermal pair cascade process. Detailed investigations into the efficiency of producing pairs through this process have been carried out for the idealized case of uniform, spherical sources (see Lightman and Zdziarski 1987, Svensson 1987, Done and Fabian 1989). These authors find that for a wide range of parameters, the "pair-yield," PY (that fraction of energy initially directed to nonthermal electron acceleration which ultimately appears as rest mass energy of pairs), is solely a function of the "electron compactness parameter," l_e :

$$PY = \begin{cases} 2 \times 10^{-3} l_e & 3 < l_e < 50 \\ 0.1 & l_e > 50 \end{cases} \quad (2.40)$$

where (see, e.g., Begelman, Sikora, and Rees 1987):

$$l_e = (L_e/r)\sigma_T/(m_e c^3) , \quad (2.41)$$

and L_e is the total power given to electron acceleration in a source of size r . Detailed investigation (or any investigation) of pair

cascades in the context of a two-temperature (or any) disk has not yet been done. As a starting point then, we apply equations (2.40) and (2.41) to the disk, noting (see, e.g. Lightman, Zdziarski, and Rees 1987) that this treatment would be appropriate in the case of marginally thick disks ($h/r < 1$) with high viscosity ($\alpha_{\text{vis}} \geq 0.1$). Then:

$$L_e = \epsilon_e L = \epsilon_e (1/12) \dot{M} c^2 \quad (2.42)$$

is the power going to nonthermal electron acceleration throughout the disk. Here we have integrated equation (2.6) to obtain $L = (1/12) \dot{M} c^2$, the total viscous dissipation of the disk (see Shapiro, Lightman, and Eardley 1976). The pair production rate is now

$$\dot{n}_+^{\text{cre}} = \text{PY} \epsilon_e \dot{u}_{\text{vis}} / (2m_e c^2) . \quad (2.43)$$

We retain the annihilation and inflow terms from the thermal model, as well as equations (2.1)-(2.3). The passage of energy through a nonthermal channel we reflect in a modified ion energy balance equation, which replaces equation (2.5):

$$\dot{u}_{\text{ep}} = (1 - \epsilon_e) \dot{u}_{\text{vis}} . \quad (2.44)$$

We no longer require detailed specification of the photon spectrum, so we replace equation (2.8) by the condition of unsaturated Comptonization:

$$y \equiv 4\theta_e (4\theta_e + 1) \max(\tau_e, \tau_e^2) = 1 . \quad (2.45)$$

Equations (2.1)-(2.3), (2.12) [with pair creation given by (2.43), annihilation by (2.13), and inflow by (2.15)], (2.44), and (2.45) are solved for the now six variables n_e , n_i , T_e , T_i , P , and h . The list of parameters to be specified is M , \dot{m} , α_{vis} , and ϵ_e . Results are presented in the "Results" section of this chapter.

Two-Temperature Quasi-Spherical Flow

Model with Nonthermal Pair Production

We next investigate pair-induced over-cooling of quasi-spherical two-temperature flows, extending the treatment of Begelman, Sikora, and Rees (1987). Here we approximate the inflow as spherical, but adjust the accretion velocity to some fraction μ of its freefall value to accommodate in a simple manner any angular momentum of the flow. Mass conservation then gives:

$$n_i = \dot{M} / (m_p v_{\text{acc}} 4\pi r^2) , \quad (2.46)$$

where

$$v_{\text{acc}} = \mu (2GM/r)^{1/2} ; \quad 0 < \mu < 1 . \quad (2.47)$$

Begelman, Sikora, and Rees (1987) define a critical radius, r_{crit} , interior to which, Coulomb energy loss from ions to electrons

overwhelms ion heating:

$$\dot{u}_{ep} = \dot{u}_{gr} \text{ at } r_{crit} , \quad (2.48)$$

where \dot{u}_{ep} is given by equation (2.4) and $\dot{u}_{gr} = GM\dot{M}/(4\pi r^4)$ is the rate of gravitational energy dissipation at r . We set the ion temperature to remain near its virial value ($T_i \gg T_e$) outside the strongly cooled region:

$$(3/2)kT_i = \epsilon_{th}(GMm_p/r) , \quad \epsilon_{th} < 1 . \quad (2.49)$$

Adopting a nonthermal scheme similar to that used with the disk flow, we divert a fraction ϵ_e of \dot{u}_{gr} to accelerate a small nonthermal population of electrons, and write pair production as

$$\dot{n}_+^{cre} = PY \epsilon_e \dot{u}_{gr} / (2m_e c^2) , \quad (2.50)$$

where equation (2.40) gives PY , equation (2.41) gives l_e , and now the total power given to electron acceleration is:

$$L_e = \epsilon_e L = \epsilon_e (1/6) \dot{M} c^2 . \quad (2.51)$$

Here we have assumed radiation is produced down to at least $r=6GM/c^2$. Integrating gravitational potential energy dissipation down to this radius gives the total luminosity $L=(1/6)\dot{M}c^2$. We approximate pair inflow:

$$\dot{n}_+^{\text{inf}} = \frac{1}{r^2} \frac{d}{dr} (r^2 n_+ v_{\text{acc}}) \quad (2.52)$$

by

$$\dot{n}_+^{\text{inf}} = n_+ v_{\text{acc}} / r . \quad (2.53)$$

Electron cooling will be unsaturated Comptonization: $y=1$ [equation (2.45)]. We solve equations (2.46), (2.48), (2.49), (2.12) [with pair creation given by (2.50), inflow by (2.53), and annihilation by (2.13)], and (2.45) [with $\tau_e \equiv n_e \sigma_T r$ defining the electron scattering optical depth for spherical geometry] for r_{crit} , $T_e(r_{\text{crit}})$, $T_i(r_{\text{crit}})$, $n_i(r_{\text{crit}})$, and $n_e(r_{\text{crit}})$. Model parameters are M , m , μ , ϵ_{th} , and ϵ_e . Results are presented in the "Results" section of this chapter.

Model with Thermal Pair Production

In our final model we examine the effect of thermal pair production on the two-temperature, quasi-spherical flow. Pair creation is accomplished through the same physical processes assumed in the thermal disk model. Again, a Comptonized photon spectrum is given by equation (2.9). The seven flow variables at the critical radius [r_{crit} , $T_e(r_{\text{crit}})$, $T_i(r_{\text{crit}})$, $n_i(r_{\text{crit}})$, $n_e(r_{\text{crit}})$, $N_P(r_{\text{crit}})$, and $N_W(r_{\text{crit}})$] are found by solving equations (2.46), (2.48), (2.49), (2.8) & (2.10) [both with $\tau_e = n_e \sigma_T r$], (2.12) [with pair creation given by (2.17), annihilation by (2.13), and inflow by (2.53)], and (2.54):

$$\dot{u}_{gr} = u_{rad} / [\max(1, \tau_e)r/c] . \quad (2.54)$$

Model parameters are M , \dot{m} , α , μ , and ϵ_{th} . Results are presented in the following section.

Results

Two-Temperature Disk

A computer code was developed to obtain the following solutions to the two-temperature disk. The code is sufficiently general to be used for both the thermal and nonthermal disk models.

Model with Thermal Pair Production. The pair inflow term given by equation (2.15) renders pair equilibrium, equation (2.12), a first order differential equation in the variable r . Thus solutions to the disk models detailed in the preceding sections are obtained by numerically integrating equation (2.12) in from some large radius to near the inner edge of the disk: $r_{in} = 6GM/c^2 = 3r_g$. At each step along the integration the model equations are solved simultaneously (numerically) for the various disk variables. The boundary value we supply to the differential equation at the starting point is the value of the accretion pair flux: $hrv_{acc}n_+$. The starting radius is always chosen large enough so that setting $hrv_{acc}n_+$ either to zero or to its static value (neglecting the pair inflow term) would introduce acceptably small errors (<10%) in pair density at all subsequent points along the integration. All integrations terminate at $r = 3.5r_g$. (The disk model breaks down as r_{in} is approached.)

Figures 1 and 2 present solutions to the thermal disk for two reasonable values of the viscosity, $\alpha_{\text{vis}}=0.1$ and 0.5 , and for a wide range of \dot{m} . The power-law index of the photon spectrum is set to $\alpha=0.7$ for all thermal model runs that we consider in this paper, consistent with observations of a majority of Seyferts (see, e.g. Mushotzky 1984). The black hole mass is set at $10^7 M_{\text{sol}}$ throughout. Lines of constant pair abundance $z \equiv 2n_+/n_1$ are shown in the figures as solid lines, and lines of constant $h_* \equiv h/r$ are drawn dashed. The thin disk criterion ($h_* \ll 1$) is strictly met only far to the left of the $h_*=1$ line, though results should be accurate to within a factor of about 2 in the neighborhood of this line (see Shapiro, Lightman, and Eardley 1976). We find pair densities in the thermal disk remain well below ion densities, with $z < 1$ for all reasonable parameter choices. We also find z generally to increase with decreasing r and increasing \dot{m} . Exceptions are the dropoff in z very near the disk's inner edge [due to the zero-stress boundary condition produced by Φ in equations (2.3) and (2.6)], and a turnover seen for $1 \geq \alpha_{\text{vis}} \geq 0.5$ in the $h_* \geq 1$ region (see, e.g., Figure 2). Here increasing \dot{m} causes the electron scattering optical depth to rise sufficiently to force equation (2.8) to lower the electron temperature. Thermal pair production rates, which are extremely sensitive to the electron temperature, fall, suppressing pair production. We find the presence of pairs to inflate the disk: h/r increases at constant r/r_g . However, the low pair abundances in the thermal disk keep this inflation negligibly small (the lines of constant h/r in Figures 1 and 2 would not be altered were there no pairs present).

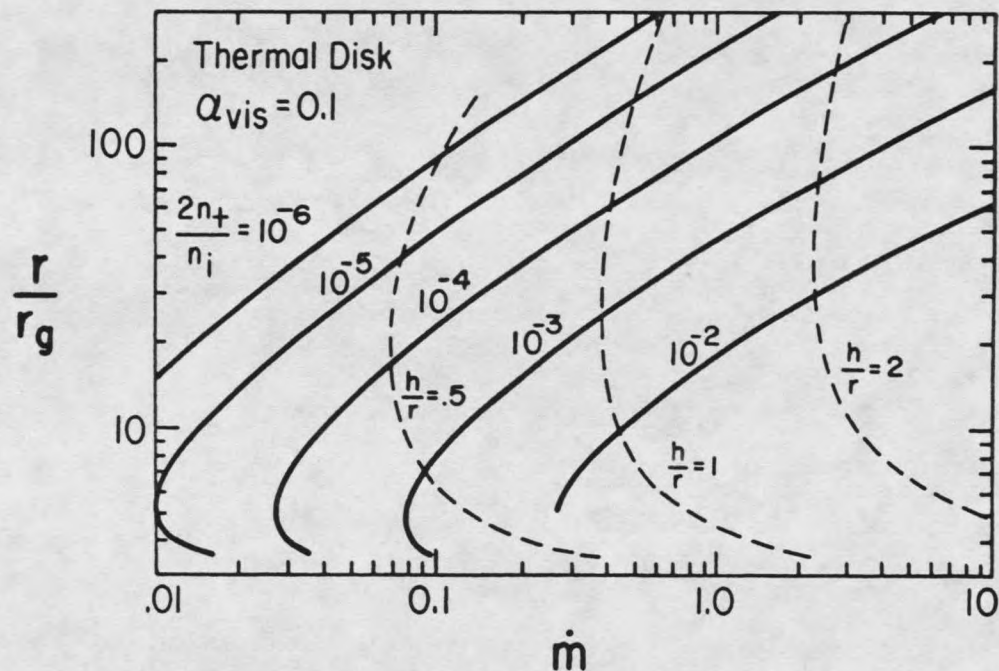


Fig. 1. Pair abundance, $z=2n_+/n_1$, and disk half-thickness $h_*=h/r$, in the thermal disk for $\alpha_{vis}=0.1$, as a function of radial position r/r_g and dimensionless accretion rate $\dot{m} = \dot{M}_{vis}/\dot{M}_{Edd}$. Solid curves indicate lines of constant z ; dashed curves are lines of constant h_* . The thin disk assumption, $h < r$, is valid to the left of the $h_*=1$ line. Here $r_g = 2GM/c^2$, and $\dot{M}_{Edd} c^2$ is the Eddington luminosity.

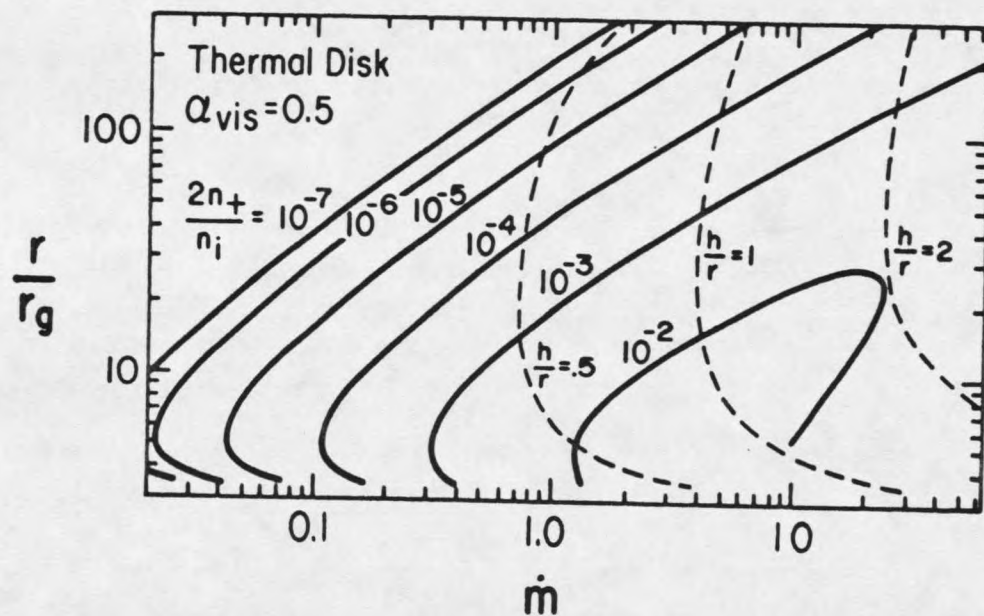


Fig. 2. Pair abundance, $z=2n_+/n_i$, and disk half-thickness $h_*=h/r$, in the thermal disk for $\alpha_{vis}=0.5$, as a function of radial position r/r_g and dimensionless accretion rate $\dot{m} = \dot{M}/\dot{M}_{Edd}$. Solid curves indicate lines of constant z ; dashed curves are lines of constant h_* . The thin disk assumption, $h < r$, is valid to the left of the $h_*=1$ line. Here $r_g = 2GM/c^2$, and $\dot{M}_{Edd} c^2$ is the Eddington luminosity.

Thermal pair production has little effect upon disk temperatures. Figure 3 shows ion and electron temperatures in the thermal disk with $\alpha_{\text{vis}}=0.1$ for several accretion rates. Ion temperatures are quite high ($T_i=10^{10-12}\text{K}$), while electrons are much cooler, with $T_e=1-3\times 10^9$ ($\theta_e\approx 0.3$). Turning off pair production (setting $\dot{n}_+^{\text{cre}}=0$) produces no change in the figure (compare Figure 9), though indeed a slight rise in the ion temperature and drop in the electron temperature for a given \ln and r/r_g always accompanies the inclusion of pairs in the model. Thermal pair production has a slightly greater effect on the scattering optical depth of the disk than on temperature. Figure 4 shows the electron (solid line) and ion (dashed) optical depths for the thermal disk for the same parameters as Figure 3. The dotted lines of Figure 4 indicate $\tau_e(=\tau_i)$ with no pairs. The effect of pairs is to lower τ_i from its pair-free value, and to raise τ_e (see also Figure 10).

Similar results were obtained when varying the power-law slope over the range $0.3<\alpha<0.8$, which covers essentially all Seyferts and radio-quiet quasars (e.g. see Lightman and Zdziarski 1987 and the Appendix).

Recently other authors have investigated the effects of thermal pair production on optically thin accretion disks. White and Lightman (1989) investigated the disk in both the one-temperature and two-temperature versions, including as electron cooling mechanisms: pure bremsstrahlung, Comptonized bremsstrahlung, and Comptonized external soft photons. Their results verified ours in the external soft source model. They found, however, that the bremsstrahlung models

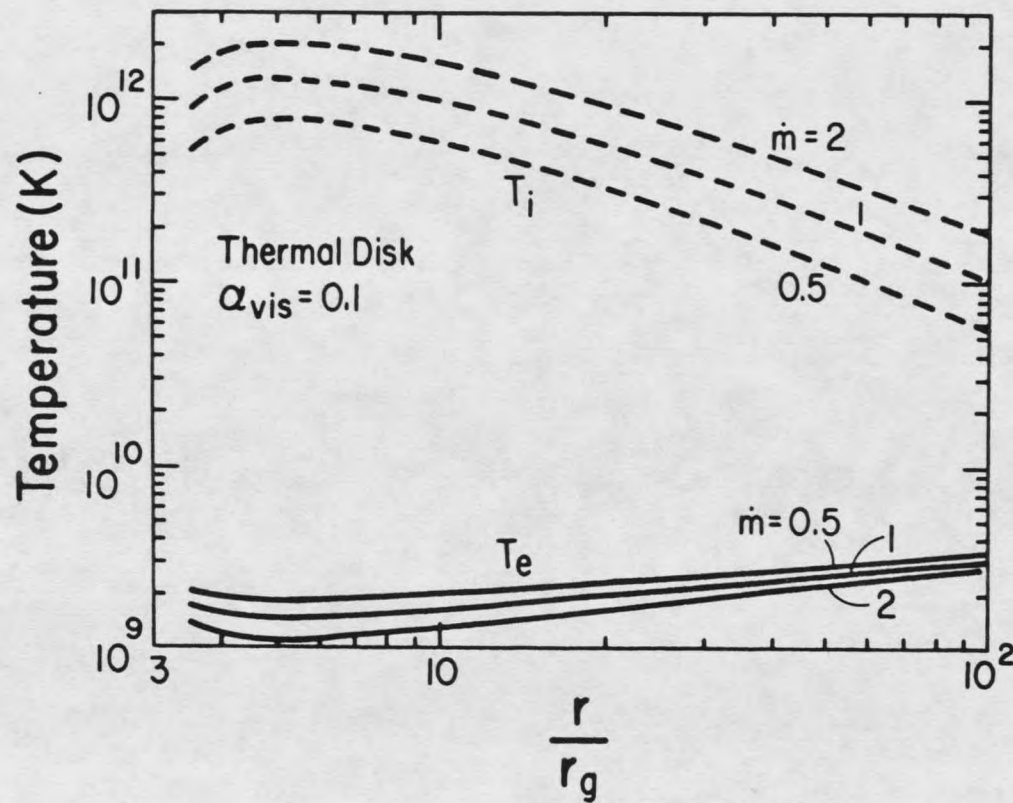


Fig. 3. Radial distribution of electron temperature T_e (solid lines) and ion temperature (dashed lines) in the $\alpha_{vis}=0.1$ thermal disk. Temperatures are shown for accretion rates $\dot{m}=0.5, 1, \text{ and } 2$.

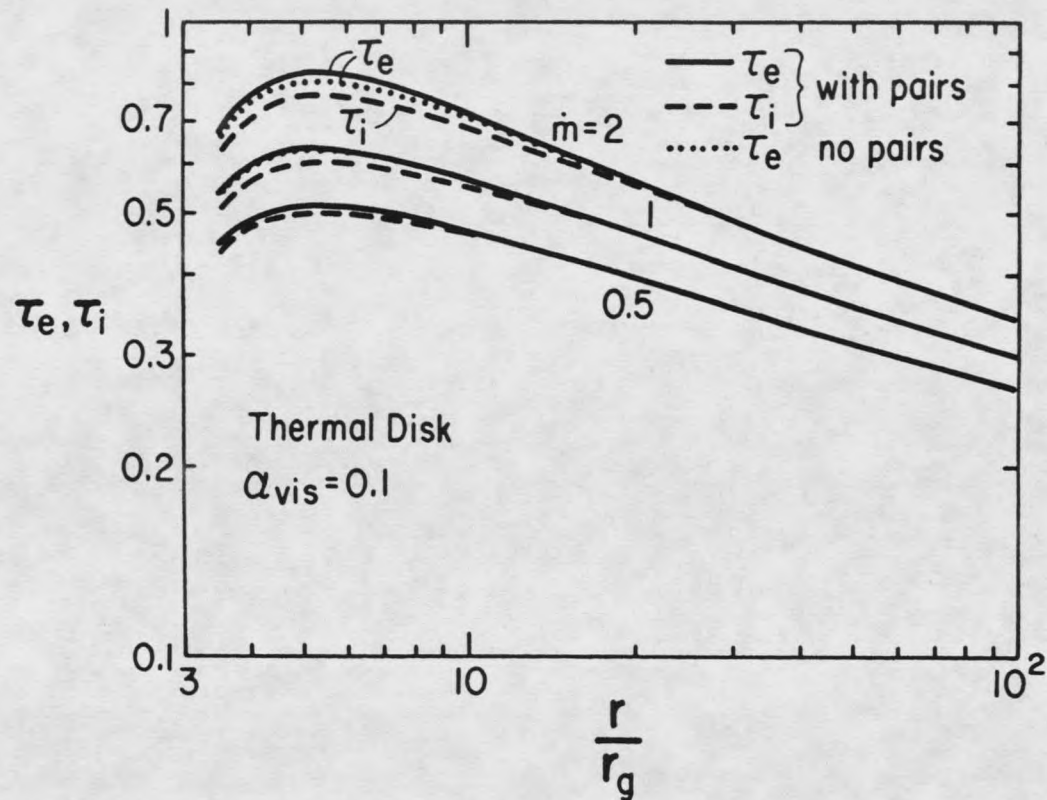


Fig. 4. Radial distribution of electron scattering optical depth, $\tau_e = n_e \sigma_T h$ (solid lines), and ion optical depth, $\tau_i = n_i \sigma_T h$ (dashed lines), in the $\alpha_{\text{vis}} = 0.1$ thermal disk for $m = 0.5, 1,$ and 2 . Pair production produces the splitting of τ_e and τ_i seen at small radii. The dotted lines show the $\tau_e (= \tau_i)$ line in the case of no pairs (pair production ignored).

exhibited a critical accretion rate above which pair runaway is predicted in the innermost regions of the disk. Below the critical rate, high and low pair abundance states are both possible. Kusunose and Takahara (1988) investigated the two-temperature disk, including pure bremsstrahlung and Comptonized cyclotron higher harmonics. They found a critical accretion rate and high and low pair states in agreement with White and Lightman (1989).

Model with Nonthermal Pair Production. Figures 5-8 present solutions to the nonthermal disk model for various choices of α_{vis} and ϵ_e . For a wide range of the viscosity, pairs can dominate ions if nonthermal processes receive more than about 1/3 of the power generated through viscous dissipation, i.e., $\epsilon_e > 0.3$. When a majority of the luminosity is funneled through the nonthermal channel, z can reach a maximum value of 5-10 (see Figure 8). We find z to increase with both increasing ϵ_e and increasing α_{vis} for a given \dot{m} and r/r_g .

Figures 5-8 indicate that pair abundance varies with accretion rate as $z \propto \dot{m}^2$ for low z regions (small \dot{m} and large r/r_g). Earlier studies of nonthermal pair creation in spherically accreting systems (i.e., Lightman and Zdziarski 1987) exhibit the weaker dependence $z \propto \dot{m}^1$. The author was the first to obtain, and explain, this important difference between disk and spherical flows. The difference arises from the competition between annihilation and inflow in pair balance in the small \dot{m} region. Inflow dominates for spherical models, but the disk model reverses the situation and annihilation dominates, giving rise to the differing forms of $z(\dot{m})$. To show this, we first examine

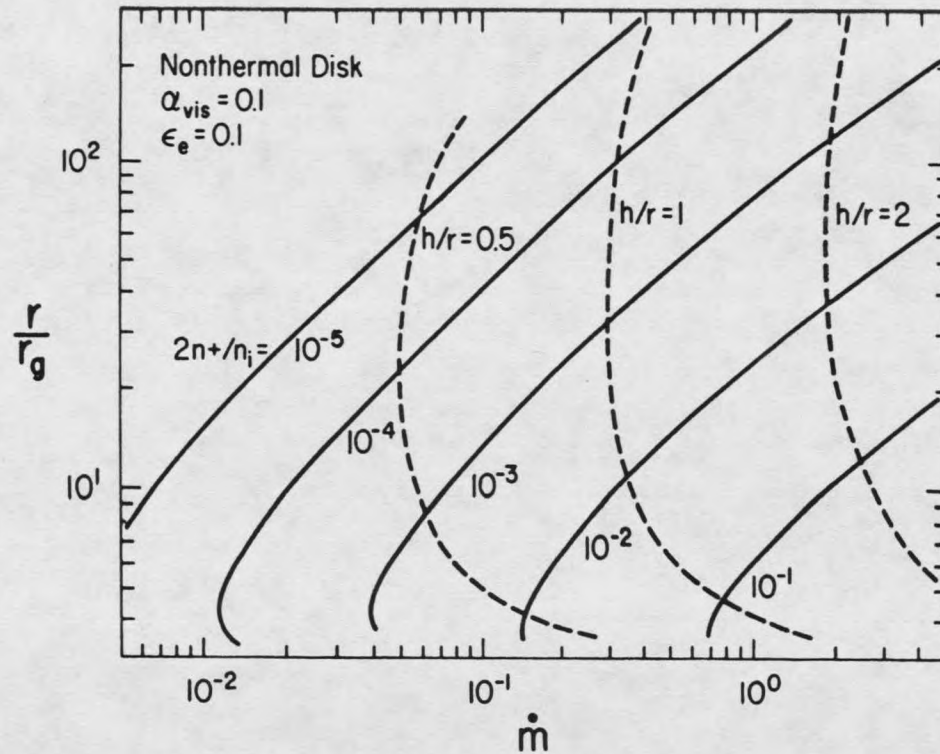


Fig. 5. Pair abundance z and disk half-thickness h_* in the nonthermal disk as a function of radial position and accretion rate. Lines of constant z are solid; lines of constant h_* are dashed. Here $\alpha_{\text{vis}}=0.1$ and $\epsilon_e=0.1$.

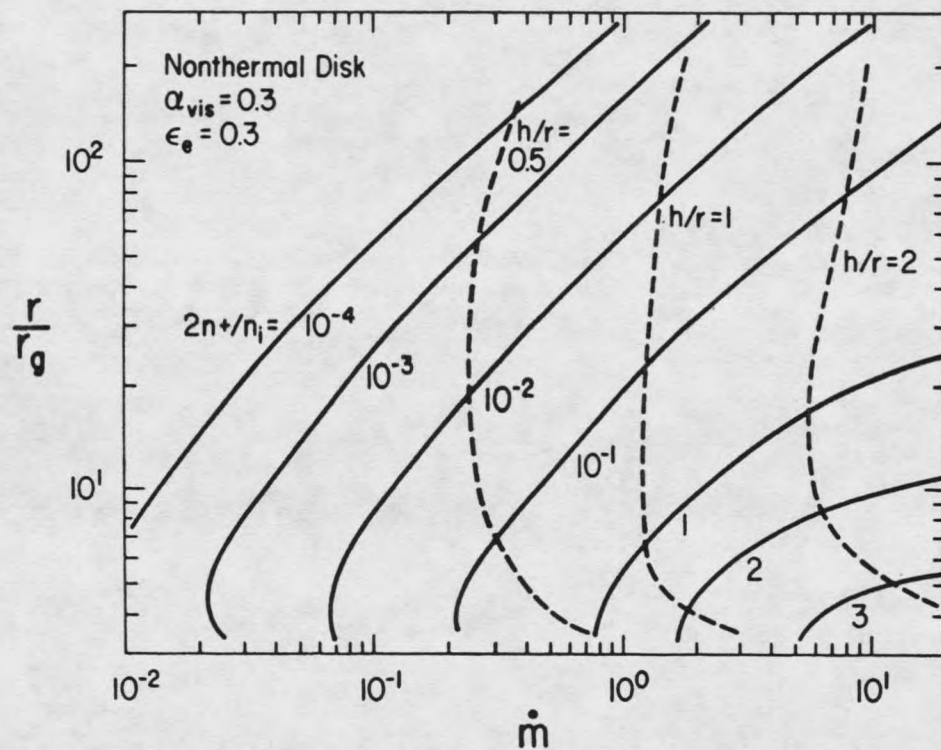


Fig. 6. Pair abundance z and disk half-thickness h_* in the nonthermal disk as a function of radial position and accretion rate. Lines of constant z are solid; lines of constant h_* are dashed. Here $\alpha_{\text{vis}}=0.3$ and $\epsilon_e=0.3$.

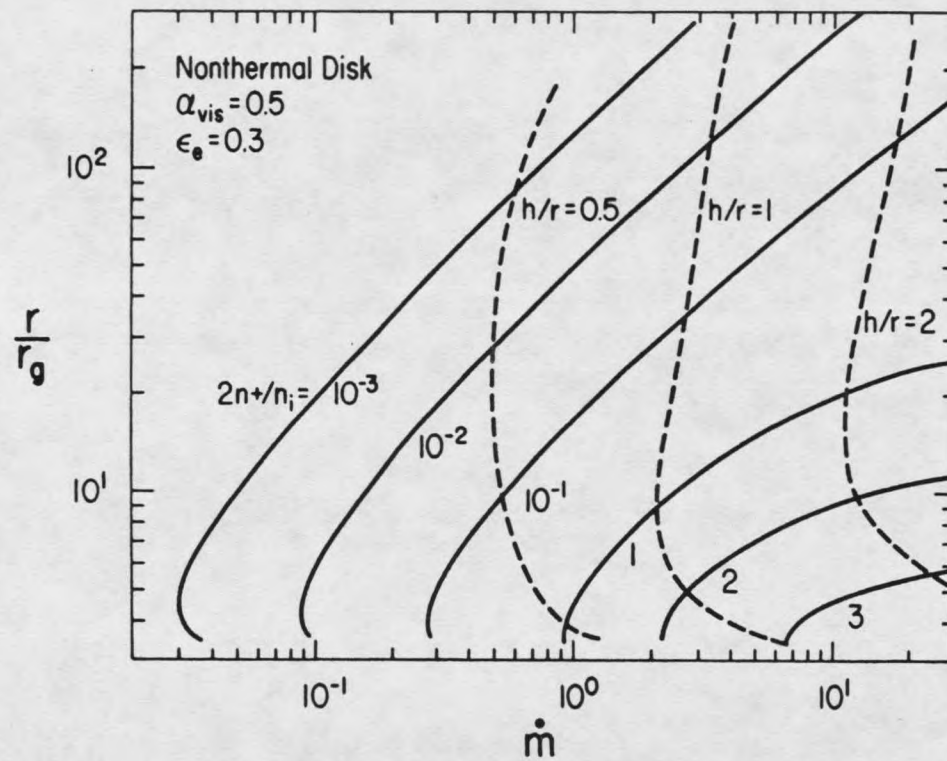


Fig. 7. Pair abundance z and disk half-thickness h_* in the nonthermal disk as a function of radial position and accretion rate. Lines of constant z are solid; lines of constant h_* are dashed. Here $\alpha_{\text{vis}} = 0.5$ and $\epsilon_e = 0.3$.

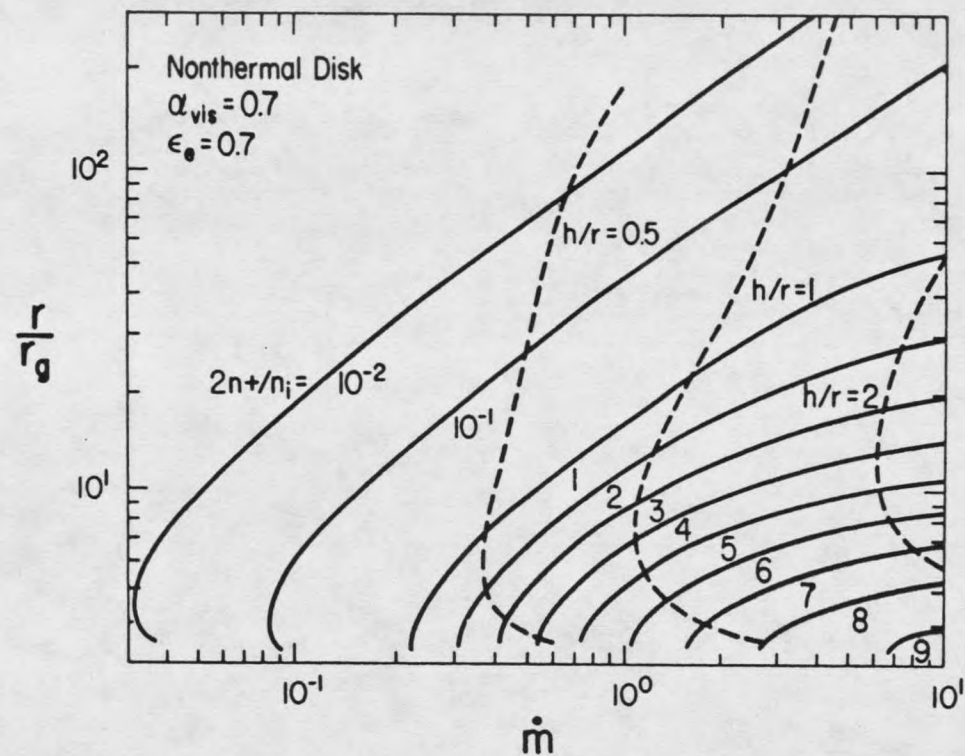


Fig. 8. Pair abundance z and disk half-thickness h_* in the nonthermal disk as a function of radial position and accretion rate. Lines of constant z are solid; lines of constant h_* are dashed. Here $\alpha_{\text{vis}} = 0.7$ and $\epsilon_e = 0.7$.

the ratio of pair inflow [equation (2.15) for the disk, equation (2.52) for spherical flow] to annihilation [equation (2.13) for any flow]. For $n_+/n_i \ll 1$ we have

$$\frac{\dot{n}_+^{\text{inf}}}{\dot{n}_+^{\text{ann}}} = \frac{4\pi m_p r(r \text{ or } h)v_{\text{acc}}^2}{(3/8)\sigma_T c r \dot{M}}, \quad (2.55)$$

in which we find the only difference between the disk and spherical geometries is the choice of variables in the parentheses: r for spherical flow and h for the disk. We hold functions of r constant and collect in dependence. The spherical flow accretion velocity given by equation (2.47) is a constant fraction of free-fall velocity, and has no \dot{m} dependence. Thus for spherical flows we have $(\dot{n}_+^{\text{inf}}/\dot{n}_+^{\text{ann}})_{\text{sph}} \propto \dot{m}^{-1}$, which indicates pair inflow dominates annihilation at sufficiently small accretion rates. The disk accretion velocity is obtained from mass conservation [equation (2.16)]: $v_{\text{acc}} \propto \dot{m} / (n_i r h)$. For small z the pair-free analytic solutions of Shapiro, Lightman, and Eardley (1976) will be useful. These show $n_i \propto \dot{m}^{-1/4}$ and $h \propto \dot{m}^{5/12}$. Thus $v_{\text{acc}} \propto \dot{m}^{10/12}$ and $(\dot{n}_+^{\text{inf}}/\dot{n}_+^{\text{ann}})_{\text{disk}} \propto \dot{m}^{13/12}$ for the disk, which indicates annihilation dominates pair inflow at small accretion rates. We can now use the appropriate form of pair balance to obtain z . For spherical flow, balancing creation [equation (2.50) with $l_e < 50$] with inflow [equation (2.52)] gives $z \propto \dot{m}^{-1}$. For the disk, balancing creation [equation (2.43) with $l_e < 50$] with inflow gives $z \propto \dot{m}^{-2}$. In fact, insertion of the constants and functions of r into the nonthermal disk pair balance,

and using the pair free analytic results of Shapiro, Lightman, and Eardley (1976) yields the estimate for the nonthermal disk:

$$z = 4.1 \times 10^3 \epsilon_e^2 \dot{m}^{25/12} \alpha_{\text{vis}}^{-11/12} \Phi^{13/12} (r/r_g)^{-21/8}, \quad (2.56)$$

which is in good agreement with our numerical results at small \dot{m}

Substantial pair production can greatly affect disk thickness. We find, as in the thermal disk, that pairs inflate the disk: h/r increases at constant r/r_g , although here the effect can be quite large. This inflation is seen as a shift to smaller \dot{m} (to the left) of the $h/r=\text{constant}$ lines in those portions of the $\dot{m}-r/r_g$ plane in which pairs are numerous (compare, e.g., Figure 2 with Figure 7). As a corollary we note that significant pair production lowers the upper limit to the range of \dot{m} for which the disk remains thin ($h/r < 1$). Figure 9 shows the effect of copious nonthermal pair production on the ion and electron temperatures for $\alpha_{\text{vis}}=0.7$, $\epsilon_e=0.7$, and $\dot{m}=0.5$. Solid lines indicate the case with pairs present, dashed lines with no pairs (\dot{n}_+^{cre} set to zero). As in the thermal model, pairs elevate ion temperatures and depress electron temperatures, although here the effect can be considerably more pronounced. Similarly, Figure 10 presents the depression and elevation of τ_i and τ_e , respectively, due to pairs for the same model parameters as Figure 9. The figure shows that even for a pair dominated inner region, where $\tau_e/\tau_i \approx 5$, the ion density has been reduced to such a degree that the electron optical depth remains below one. For $\epsilon_e < 0.1$ pairs fail to dominate ions and results closely agree with those in the thermal flow.

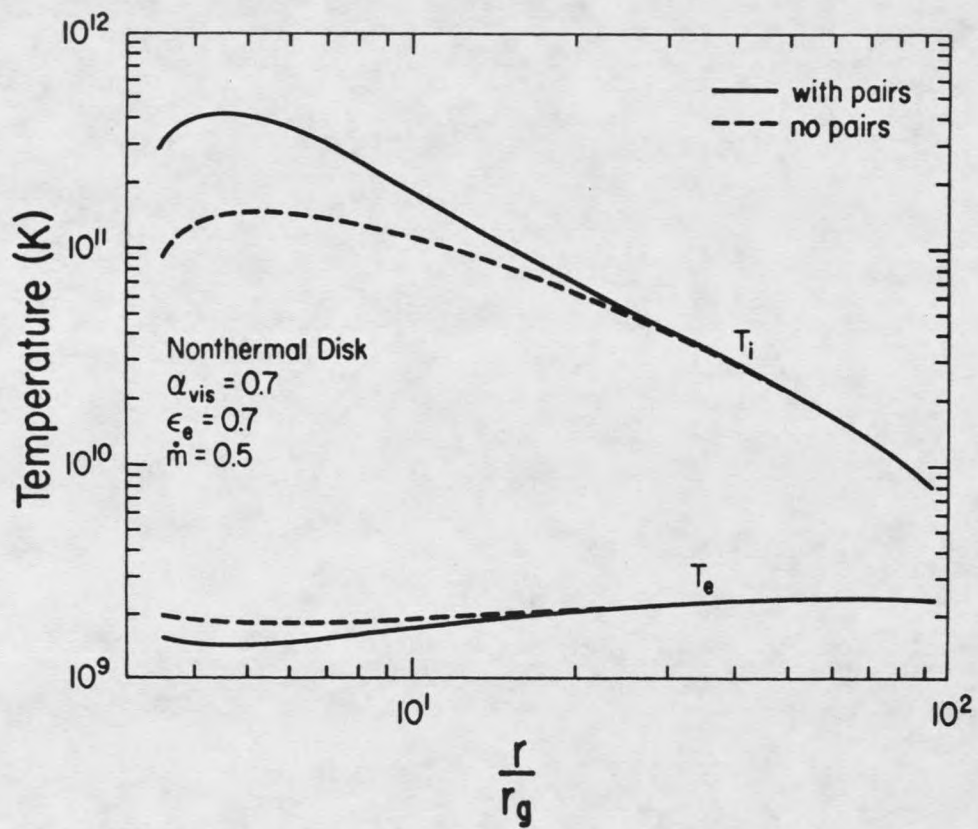


Fig. 9. Radial distribution of electron temperature T_e and ion temperature T_i in the nonthermal disk of Fig. 8, for the accretion rate $\dot{m} = 0.5$. The dashed lines indicate the pair-free case.

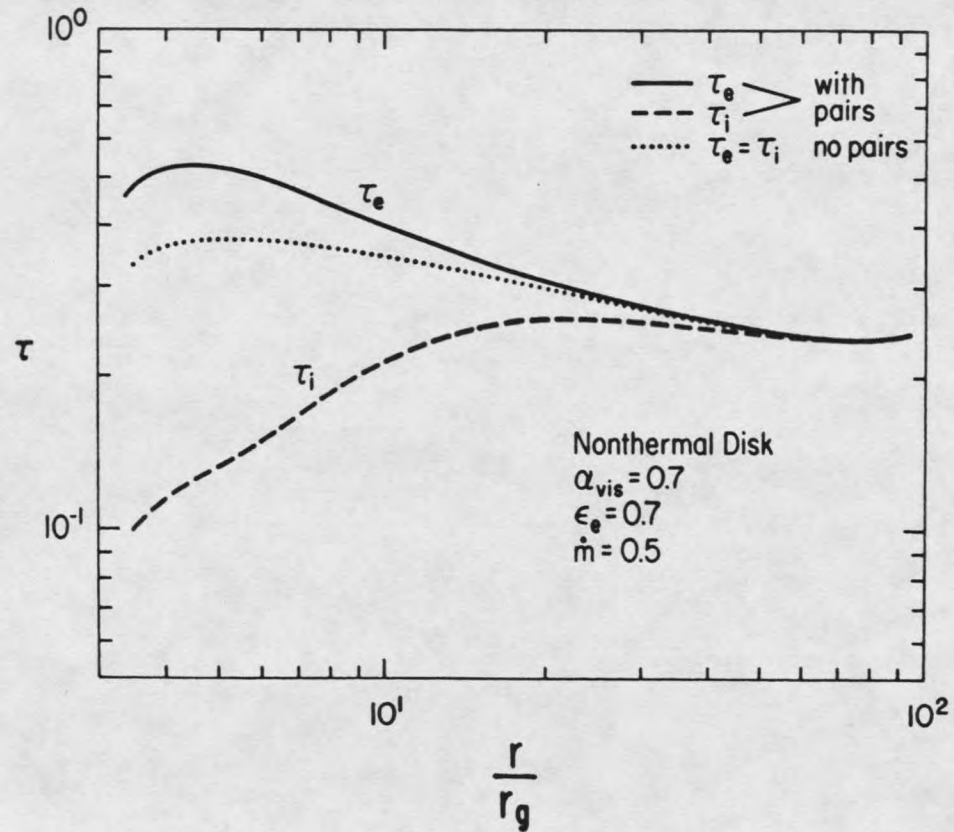


Fig. 10. Radial distribution of electron optical depth (solid line) and ion optical depth (dashed line), for the nonthermal disk of Fig. 9. The pair-free case is shown dotted.

The effect that pair inflow can have in lowering equilibrium pair densities is seen in Figure 11, where the radial profile of pair abundance z for the same parameters as Figures 9 and 10 is shown by the solid line. The dashed line indicates the static solution, in which the inflow term of pair equilibrium [equation (2.12)] has been neglected. Pair advection has lowered z by a factor ≥ 10 in the inner, pair-dominated region, underscoring the importance of including inflow as well as annihilation in pair-dominated flows.

Two-Temperature Quasi-Spherical Flow

To solve our models of quasi-spherical, two-temperature flows we conduct a numerical search for the radius, r_{crit} , at which $\dot{u}_{\text{ep}} = \dot{u}_{\text{gr}}$, subject to the values of n_e , n_i , T_e , T_i (and N_p & N_w for the thermal model) that we obtain by simultaneously solving the specified set of flow equations at that radius. A computer code was developed to obtain the following solutions to the two-temperature, quasi-spherical flow. The code may be used for both the thermal and nonthermal models.

Figure 12 shows the variation of r_{crit} over a large range of \dot{m} for the nonthermal model with $\epsilon_{\text{th}}=0.4$; $\epsilon_e=0, 0.1, 0.3, \text{ and } 1.0$; and $\mu=0.3$. Figure 13 presents the case $\mu=0.7$. On these figures, for a given \dot{m} , the radii above the r_{crit} line constitute the inflated, two-temperature domain ($T_i \gg T_e$, $\dot{u}_{\text{ep}} < \dot{u}_{\text{gr}}$), supported by ion pressure. The onset of over-cooling of ions is presumed to happen in the neighborhood of r_{crit} , where ion cooling by electrons just balances gravitational energy release. The dashed lines in Figures 12 and 13

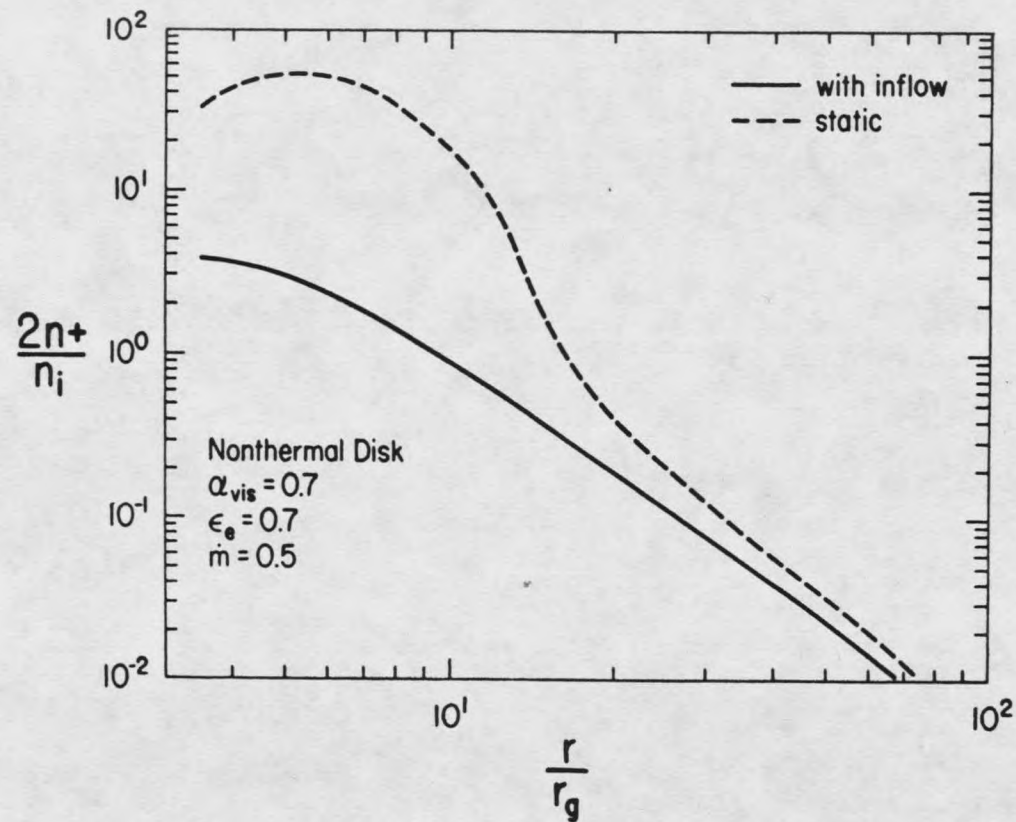


Fig. 11. Radial distribution of pair abundance in the nonthermal disk of Figs. 9 and 10. The dashed line indicates the static solution, found by neglecting pair inflow.

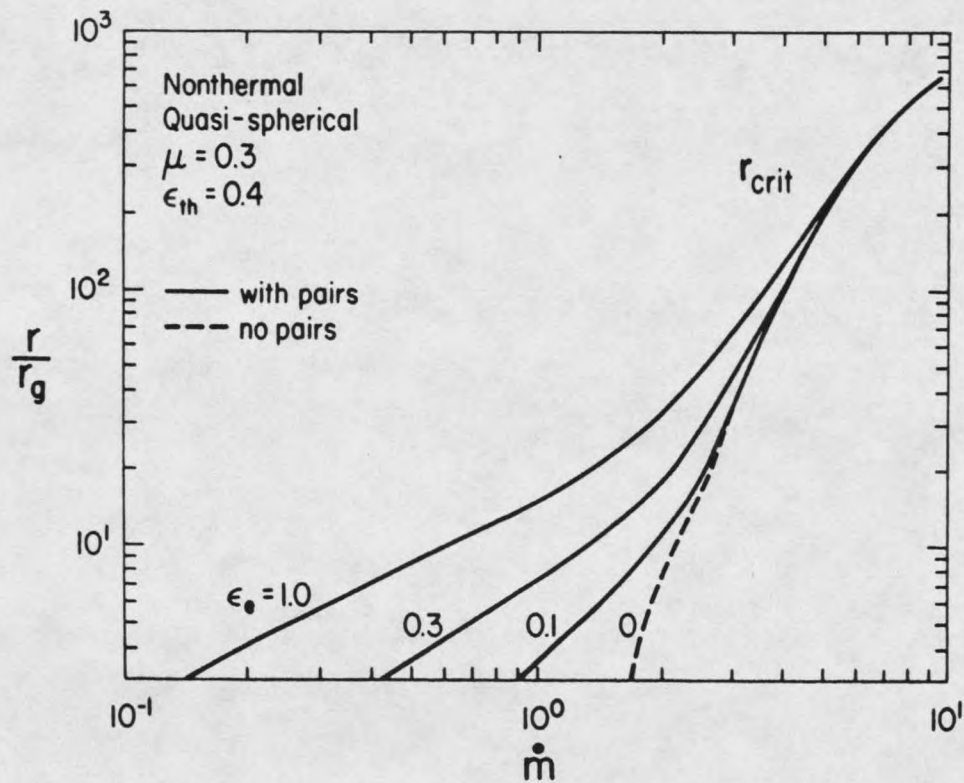


Fig. 12. Critical lines for the nonthermal, quasi-spherical flow, with $\mu=0.3$, and $\epsilon_{th}=0.4$. Two-temperature flow exists above the critical line, while over-cooling of ions occurs under the line. The dashed line shows the $\epsilon_e=0$ (no pairs) case, and the solid lines show the $\epsilon_e=0.1, 0.3$, and 1.0 cases.

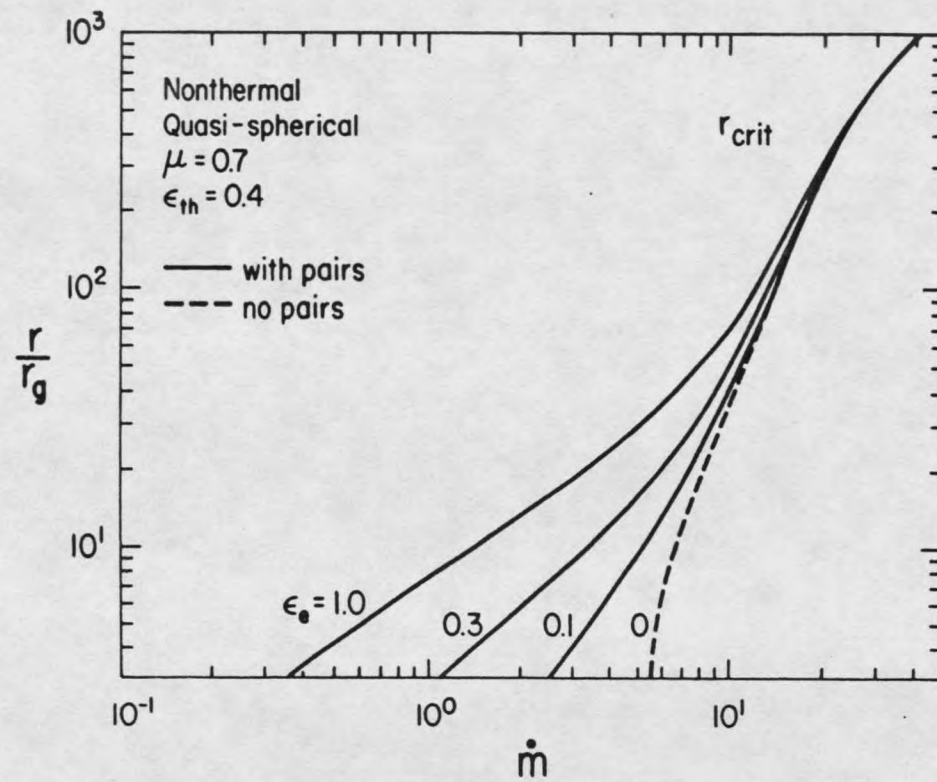


Fig. 13. Critical lines for the nonthermal, quasi-spherical flow, with $\mu=0.7$, and $\epsilon_{th}=0.4$. Two-temperature flow exists above the critical line, while over-cooling of ions occurs under the line. The dashed line shows the $\epsilon_e=0$ (no pairs) case, and the solid lines show the $\epsilon_e=0.1, 0.3$, and 1.0 cases.

indicate the location of the critical radius with no pairs present ($\epsilon_e=0$). We find that for a given \dot{m} , pairs will greatly enlarge the size of r_{crit} as nonthermal pair production is turned up (increasing ϵ_e). For constant ϵ_e , r_{crit} grows with increasing \dot{m} . The pair densities we find at the critical radius are shown in Figure 14 for the same parameters as in Figure 12. Note that $z>1$ for $\epsilon_e \geq 0.1$ at small critical radii. We find that nonthermal pair production in the quasi-spherical geometry, just as in the case of the disk, is sufficiently copious to allow pairs to overwhelm ions for wide ranges of parameters.

Thermal pair production in the quasi-spherical flow for any reasonable choice of parameters, has little effect upon r_{crit} . We find that z always remains < 1 at r_{crit} . The dashed line of Figure 14 shows z due to thermal pair production at various critical radii for typical μ and ϵ_{th} .

We find that our treatment of nonthermal pair production produces considerably smaller pair abundances than Begelman, Sikora, and Rees (1987) found in their study. The latter treatment therefore overestimated the size of the over-cooled region, and thus the size of the critical radius, as shown in Figure 15. For 10% of the dissipated gravitational energy going through the nonthermal channel, we show critical radii found by Begelman, Sikora, and Rees (1987) as the dotted line, the critical radii we found as the solid line, and the pair-free reference case as the dashed line.

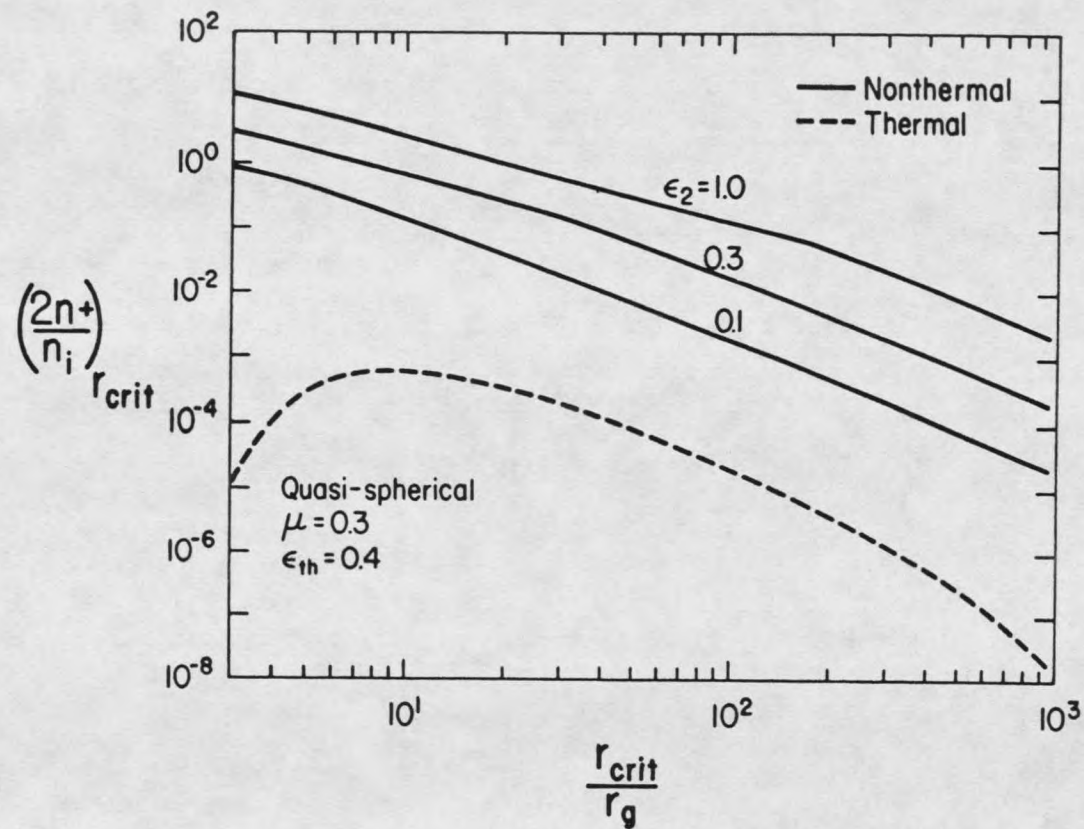


Fig. 14. Pair abundances on the critical line in the nonthermal, quasi-spherical flows of Fig. 12 (solid lines) and in the thermal, quasi-spherical flow (dashed line). Here $\epsilon_2 = \epsilon_e$.

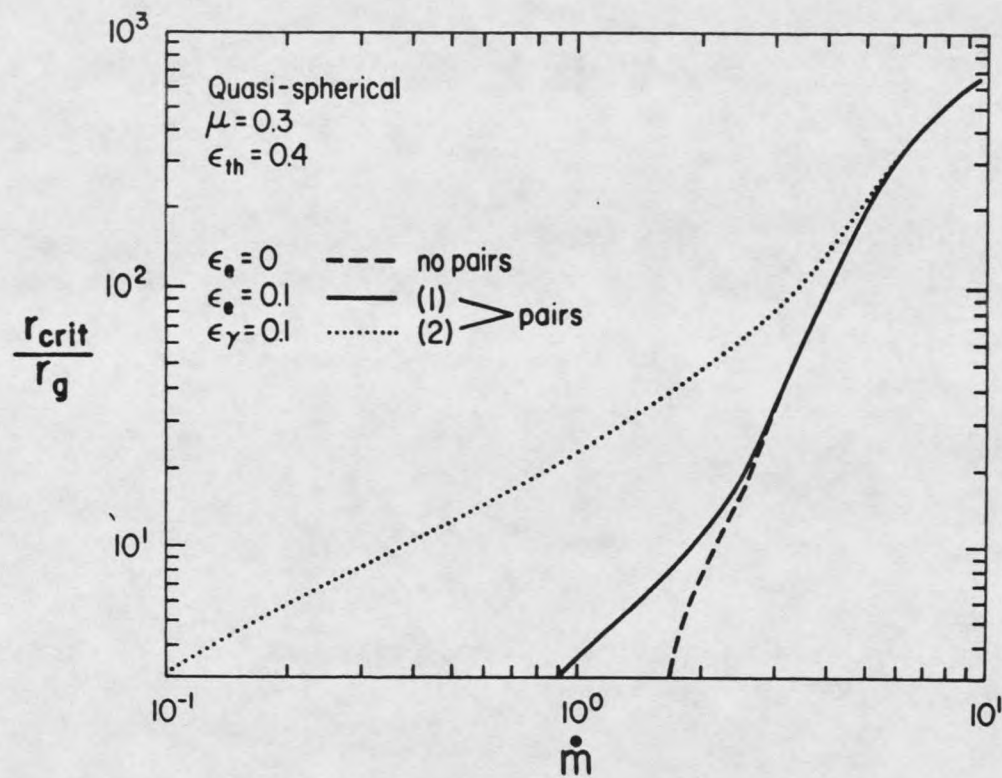


Fig. 15. Comparison of critical lines for nonthermal, quasi-spherical flow using differing pair production formulae. The solid line (1) shows our model with $\epsilon_e=0.1$, $\mu=0.3$, and $\epsilon_{th}=0.4$. The dotted line (2) represents the substitution of the nonthermal pair production expression used by Begelman, Sikora, and Rees (1987) (their equation [11] with $\epsilon_\gamma=0.1$) for our equation (26). The dashed line is the $\epsilon_e=0$ (pair-free) model.

CHAPTER 3

PAIR CASCADE SHOWER ATMOSPHERE

Chapter 2 addressed the issue of pair production within a specific class of accretion flows. Once the pair-altered flow structure is determined, the radiation spectrum emitted from the flow can always in principle be determined. The battle is only partially won however, for the question immediately arises: Is what leaves the accretion flow surface the same as what we see through our telescopes and detectors? Any intervening matter or radiation between the primary source and the observer may reprocess the primary spectrum. The composition, spatial distribution, and energy distribution of this background atmosphere must be known in order to calculate the nature and extent of this reprocessing. One then encounters the following difficulty: the atmosphere, which modifies the escaping spectrum, is itself modified by that same spectrum. This requires a self-consistent solution of both the modified primary spectrum and the atmosphere. Much work to date (see references in Chapter 1 and the Appendix) has sidestepped this issue to some degree and arbitrarily put a scattering atmosphere into place (within appropriate theoretical and observational constraints), and then calculated the reprocessed radiation spectrum, approaches suffering from what might

be called the "fiat atmosphaera" (or, "let there be an atmosphere") syndrome.

When an accretion flow emits γ -radiation, a pair cascade may be initiated in the space surrounding the flow, and a pair cascade atmosphere will result. This chapter details the scheme by which the author obtained the first, detailed, numerical, self-consistent calculations of the steady-state pair cascade atmosphere and concurrent spectral reprocessing which occur when accretion flows radiate a portion of their luminosity as gamma-rays. We restrict our attention in this chapter to a specific type of atmosphere, the "pair cascade shower," in which the scattering of radiation back down towards the accretion flow is neglected. This and some other simplifying assumptions are relaxed in Chapter 4, where the general pair cascade atmosphere is presented.

The Accretion Flow as a Photon Source

Geometry

To construct a cascade shower atmosphere model, we must first specify the shape of the emission surface (the accretion flow surface) from which the primary spectrum emerges. As we have seen in Chapter 2 and the Appendix, predicting accretion flow geometry in AGNs can be an extremely model-dependent question. However, the range of plausible geometries can be thought to lie roughly along a one-parameter family of shapes ranging from spherical to flat disk, with toroidal, inflated disk, etc. lying somewhere in between. From a practical standpoint, we shall consider the two extreme members of

this family, which are the simplest to encode for numerical calculation: (1) the uniform, infinite plane and (2) the uniform spherical surface of radius r_e . These geometries are shown in Figure 16. Here it is important to note that the infinite plane is limited in practical astrophysical application on three counts. First, observational and theoretical evidence of uniform infinite structures in the universe is sparse. Secondly, the atmospheres we obtain in this geometry are unphysical in that they are unbounded vertically (see "Results" section for details). Thirdly, very near the surface of a radiating disk of finite lateral extent ($h \ll R$, where h is the height above the surface, and R is a typical lateral dimension of the disk), where infinite planar analysis would indeed be appropriate, equally appropriate would be the spherical model with height h above the emission surface much less than the emission radius r_e . Also, at increasingly large heights h above the finite disk, the disk increasingly resembles a point source, and the spherical model with $h \gg r_e$ is again useful. Thus the uniform sphere can of course exactly describe spherical accretion flows, but can also adequately describe finite accretion disks. The infinite plane, however, is still worth studying both for the sake of completeness, and more importantly, because it will provide invaluable insight to results from the spherical case (see "Results" section).

Spectrum

Once the emission surface has been set to either planar or spherical, the primary emission spectrum must then be specified. Our

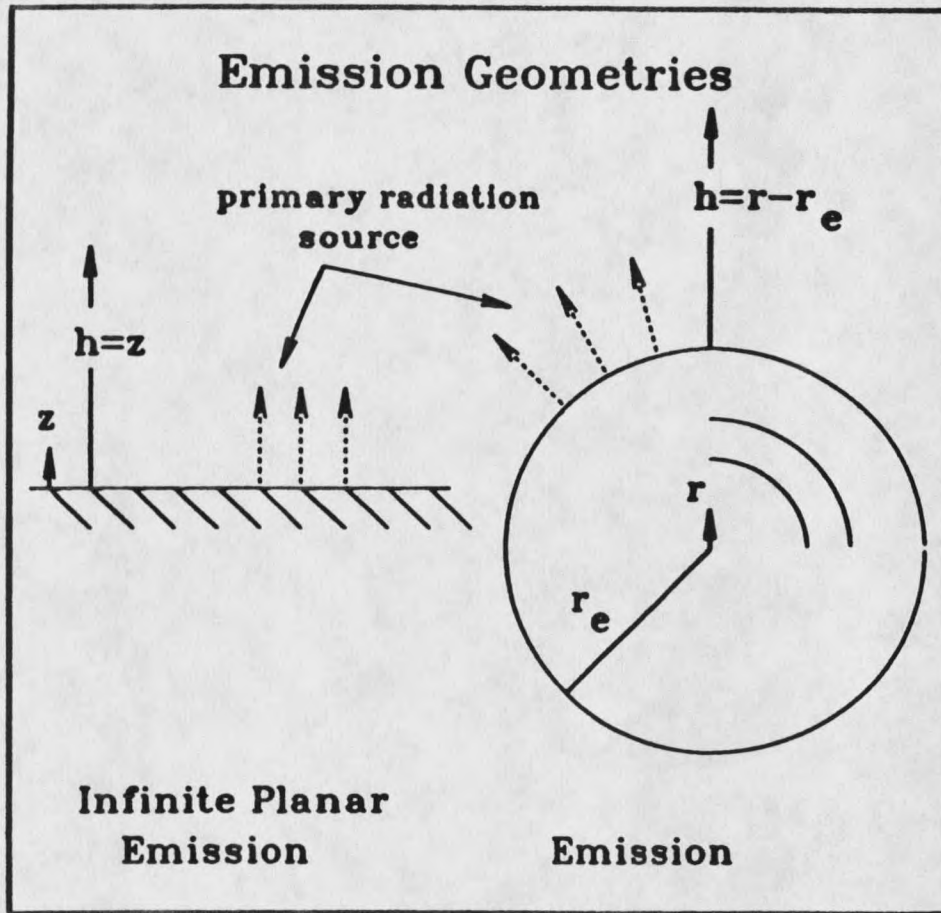


Fig. 16. Idealized accretion flow geometries investigated in this chapter, and relevant coordinate systems. Primary emission from the accretion flows shown dashed.

code will accept any input spectral shape, as long as dimensionless photon energies $x=hv/m_e c^2$ remain within certain bounds: $10^{-8} < x < 10^4$ for the models we present. For user convenience the code will automatically construct spectra in the form of Planckian, power-law, or delta function distributions, or any combinations thereof.

We draw upon both observational evidence and theoretical speculation to construct astrophysically plausible primary emission spectra from accretion flows. Referring to the typical quasar spectra shown in the Appendix, we see a prominent feature in the UV-X-ray region which rises above an extrapolated power law. This feature is common to a wide class of radio-quiet quasars and luminous Seyfert galaxies, and is insightfully known as the "UV bump." The origin of the UV bump is actively debated but a possibility is that this UV emission is the peak of a blackbody spectrum from cool ($T=10^4$ - 5×10^5 K) gas, existing either as cool clouds within hotter (two-temperature) plasma, or as an optically thick, geometrically thin accretion disk. This is quite plausible because: (1) solutions to optically thick, geometrically thin accretion disks around black holes with masses relevant to radio-quiet quasars and Seyfert 1's ($M=10^{7-8} M_{\text{sol}}$) exhibit temperatures consistent with the location of the UV bump (Malkan 1983), and (2) we have found (see Chapter 2) a broad class of accretion flows that are unstable to collapse to a thin disk state radiating the observed UV feature. The models we present will therefore include as a "soft" component of the primary (input) spectrum, $F_{\text{soft}}(x)$ (energy per unit area per unit time per unit x emitted from the surface), which we take to be a Plankian

distribution at some temperature T_{disk} or a monochromatic source at the blackbody peak $x=2.8kT_{\text{disk}}/(m_e c^2)$.

For pair production to occur, a sufficiently strong flux of hard ($x>1$) photons must be present. As discussed in Chapter 2, it would be difficult to envision this not to be the case, but it is equally difficult to make specific quantitative predictions. We therefore model this "hard" component, $F_{\text{hard}}(x)$, quite generally as either a power law (specifying the energy index α , and the upper and lower limits x_{max} and x_{min} respectively) or a monochromatic source (at some x_{hard}). The relative strength of the two components is specified by f_{hard} , the fraction of the total radiative flux going to the hard component

$$f_{\text{hard}} = \frac{\int dx F_{\text{hard}}(x)}{\int dx [F_{\text{hard}}(x)+F_{\text{soft}}(x)]} \quad (3.1)$$

The total flux can be parametrized by an effective temperature T_{eff} :

$$\sigma T_{\text{eff}}^4 = \int dx [F_{\text{hard}}(x)+F_{\text{soft}}(x)] \quad (3.2)$$

Specifying the shape of $n_{\text{soft}}(x)$ and $n_{\text{hard}}(x)$, along with specifying f_{hard} and T_{eff} , completely determines the primary (input) spectrum.

Spatially Distributed Photon and Electron-Acceleration Sources

Gravitational energy dissipation within the accretion flow may be injected into an atmosphere not only by direct radiative emission from the surface of the flow, but may also be transported by such processes as magnetic flares well out into the atmosphere, and there dissipated into radiation or into the acceleration of high energy particles (electrons). Although similar magneto-coronal processes are probably at work just next door in the solar corona, they are not well understood, and accurate detailed models are not yet available. We therefore represent any dissipation of this kind by photon and electron injection functions: $\dot{n}_{inj}(x,h)$ and $\dot{N}_{inj}(\gamma,h)$. These give the number of injected photons (or electrons) per unit volume per unit dimensionless energy x (or γ) per unit volume per unit time at height h above the accretion flow surface. Particle injection is to be considered as the acceleration of particles already present, and not the creation of new ones. Electrons and positrons are assumed to be accelerated in equal numbers, maintaining charge neutrality.

The Shower Approximations

We make the important "shower" approximation to the atmosphere: all radiation is assumed to propagate outward from the accretion flow surface (that is, photon propagation velocities will always have a positive z -component in the planar geometry, and a positive r -component in the spherical case); reflection or scattering back towards the flow is neglected. The rationale is twofold. First, on purely pragmatic grounds, a shower atmosphere yields tremendous

savings in numerical computational time over more general atmospheres in which radiation is free to travel in any direction, as is the case in Chapter 4. In the shower atmosphere, conditions at any height h above the flow cannot be influenced by conditions above h . This allows a single integration of the appropriate kinetic equations, from the flow surface upward, to produce a solution to the atmosphere. In the general atmosphere, all heights h may influence all others, and solutions to the atmosphere must be obtained through time-consuming iterative methods. The second, more fundamental point in the defense of the shower approximation is that physical conditions in the atmosphere are such that the approximation should indeed be roughly obeyed. Since the primary emission from the flow surface is by definition directed away from the source, the remaining requirements for a shower are that any spatially distributed volume sources (magneto-coronal, etc.) emit preferentially outwards (which is certainly plausible, and weakly supported by solar flare observations) and that the atmosphere not become very optically thick, so that photons will on average scatter no more than a few times on their transit through the atmosphere and thereby have little opportunity to be back-scattered. In fact, for most of the astrophysically plausible models we run in this chapter (see "Results" section), the scattering optical depth in pairs remains much less than unity and always remains \leq a few. The shower approximation is shown schematically in Figure 17.

The shower assumption approximately allows for a simple, extremely crude, treatment of radiative transfer in which radiation

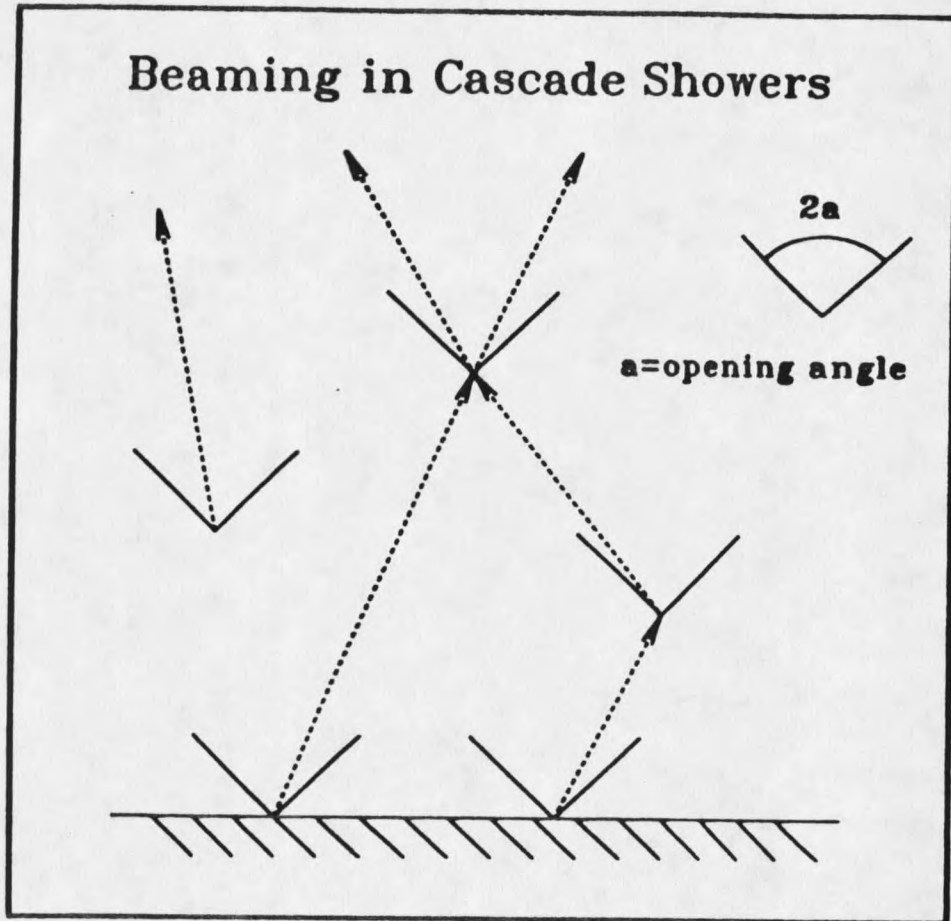


Fig. 17. Graphical representation of criteria for shower atmosphere. All radiation and particle velocities (dashed lines) at any point in the atmosphere are directed within outward-pointing solid angle cones of opening angle a . The most general showers allow $a = \pi/2$; beamed showers are defined as $a < \pi/2$.

proceeds in the +z-direction for planar emission and in the +r-direction for spherical emission (see Figure 16). The approximate photon continuity equations, which describe how steady-state photon densities at energy x and height h change with height, then take the simple forms:

$$\frac{dn(x,z)}{dz} = \frac{\dot{n}_{\text{rct}}(x,z)}{c} + \frac{\dot{n}_{\text{inj}}(x,z)}{c} \quad \text{planar} \quad (3.3)$$

$$\frac{dn(x,r)}{dr} = \frac{\dot{n}_{\text{rct}}(x,r)}{c} + \frac{\dot{n}_{\text{inj}}(x,r)}{c} - \frac{2n(x,r)}{r} \quad \text{spherical} \quad (3.4)$$

Here $\dot{n}_{\text{rct}}(x,z\text{-or-}r)$ is the net photon reaction rate from the result of the various two-body reactions we consider: photon-electron scattering, photon-photon pair creation, and pair annihilation (see the following section). The additional term in equation (3.4) is the inverse square law dilution as radiation spreads radially outward: $n=1/r^2 \rightarrow (dn)/(dr)=-2n/r$.

In a second fundamental simplifying assumption, we shall employ angle-averaged cross sections and reaction rates corresponding to isotropic photon and electron distributions. The rationale is again twofold. First, on pragmatic grounds, the assumption of isotropy affords tremendous savings in both the ease of analysis and in numerical computational considerations. This treatment serves as a convenient starting point whence we proceed to Chapter 4, in which this assumption is relaxed and exact reaction rates are calculated for

arbitrarily anisotropic distributions. Second, isotropic reaction rates do not differ drastically from rates corresponding to distributions likely to be found in the shower atmosphere. To verify this claim, and to provide an estimate of the error caused by the use of isotropic rates, we calculated the exact photon-electron scattering rate $R(\theta)$ ($\text{cm}^{-3} \text{sec}^{-1}$) for various typical energy distributions of photons, $n_1(x)$, and electrons, $N_2(\gamma)$, for photon and particle velocity directions uniformly distributed within a solid angle cone of half-angle θ . Complete 4π steradian isotropy is given by $\theta=\pi$ and narrow beaming for $\theta\approx 0$. The specific densities $n_1(x)$ and $N_2(\gamma)$ are normalized to set the total photon and electron density each to one. We have

$$R(\theta) = \int_0^\infty dx \int_0^\theta d\theta_1 \int_0^{2\pi} d\phi_1 \int_0^\infty d\gamma \int_0^\theta d\theta_2 \int_0^{2\pi} d\phi_2 \\ \times n_1(x) N_2(\gamma) \sin\theta_1 \sin\theta_2 c(1-\beta\cos\theta_{12}) \sigma_{\text{KN}}(x_{\text{rest}}), \quad (3.5)$$

where $\beta=(1-1/\gamma^2)^{1/2}$, $\cos\theta_{12}=\sin\theta_1\sin\theta_2\cos(\phi_2-\phi_1)+\cos\theta_1\cos\theta_2$ is the cosine of the collision angle between an interacting photon and electron, $x_{\text{rest}}=x\gamma(1-\beta\cos\theta_{12})$ is the photon energy in the electron rest frame and σ_{KN} is the total Klein-Nishina cross section. The integration is easily done numerically (and one ϕ -integration may be dispensed with due to azimuthal symmetry). Defining $\mu(\theta)=R(\theta)/R(\pi)$ to be the factor by which the scattering rate is reduced from its

isotropic value, and inserting typical spectra from our runs (see "Results" section), we find that even for very narrow showers, with $\theta=20^\circ$, we obtain $\mu=0.3$ to 0.4 depending upon the spectra. That is, even for narrowly beamed showers, the assumption of isotropy yields rates that are a factor of only 2 or 3 too large. This is wholly acceptable in the game of AGN research. What is more, in reality the shower is probably nearly semi-isotropic (in the upward half-space), so that $\theta \approx 90^\circ$. This gives $\mu \approx 1.5$, which is of course quite acceptable.

Although our models are of course independent of any particular beaming angles, we note that for truly self-consistent treatment, beaming angles of intermediate values around $30-40^\circ$ are required so that isotropy introduces small errors, but at the same time radiative transfer remains principally in the z- or r-direction.

The Pair Cascade

To accurately describe the pair cascade in a most computationally economical manner we use an approximate treatment similar to that used by Lightman and Zdziarski (1987) and Fabian et al. 1986 in their studies of uniform spherical volume sources. Most of the simplifying approximations used in the treatment of the cascade in this chapter will be relaxed in Chapter 4. We have improved upon certain of their features, and modified the entire approach for use in the context of an atmosphere rather than in a uniform, fixed-volume spherical source. We review this "standard" approximate approach to the cascade because: (1) there is a remarkably wide range of choices in how to simply approximate the various features of a cascade; (2) the

cascade is, of course, of central importance to the atmosphere we construct, so the specific details of all approximations used in this model will be important in both understanding the solutions we obtain and, as Svensson (1987) notes, in making comparisons with other work; and (3) the degree to which the present model differs from the more accurately treated general cascade atmosphere of Chapter 4 can only be understood if the specific details of both are spelled out, as we now proceed to do for the case at hand. In this section we drop the positional z - and r -dependences for notational clarity, and write only energy dependences.

Photon-photon pair production absorbs photons at the rate ($\text{cm}^{-3} \text{sec}^{-1}$ per unit x)

$$\dot{n}_{\text{abs}}(x_1) = 0.2\sigma_T c n(x_1) \int_{2/x_1}^{10/x_1} dx_2 n(x_2). \quad (3.6)$$

Here we have approximated the photon-photon pair production cross section as a rectangular function, equal to zero unless the product of incident photon energies $x_1 x_2$ lies between 2 and 10, in which case the cross section is $0.2\sigma_T$. The lower limit reflects the cross section decrease near threshold (the threshold for head-on collisions is $x_1 x_2 = 1$), while the upper limit approximates the Klein-Nishina-like decline at high energies. Equation (3.6) leads to pairs being produced at the differential rate:

$$\dot{N}_{pp}(\gamma) = 2(0.2)\sigma_T c \int_{\sqrt{2}} dx_1 n(x_1) \int_{2/x_1}^{\min(x_1, 10/x_1)} dx_2 n(x_2) \delta[\gamma - (x_1 + x_2)/2] \quad (3.7)$$

The leading factor of 2 yields two particles for every pair production event. The limits of integration prevent double counting. The delta function indicates we assume the electron and positron share the available energy equally. The newly-formed pairs quickly cool from relativistic energies (where they constitute the "nonthermal" pair distribution) down to subrelativistic energies (where they thermalize before annihilation, forming the "thermal" pair population) by upscattering lower energy photons.

We accommodate the Klein-Nishina decline in scattering cross section at high energies by requiring the angle-averaged initial rest-frame photon energy $x_{rest} = \gamma x (1 - \beta \cos \theta)$ to be less than a certain cut-off value, $\gamma x < \frac{3}{4}$, where γ and x are the initial electron and photon energies and θ is the collision angle. This cut-off represents the condition for Thomson scattering and the resultant cascade is sometimes called a Thomson cascade. Thus the scattering of photons into and out of x by nonthermal electrons proceeds at the rates

$$\dot{n}_{ht+}(x) = c\sigma_T \int_{3/(4x)} dx' n(x') \int d\gamma N(\gamma) \delta(x - \frac{4}{3}\gamma^2 x') S(\frac{3}{4} - x'\gamma), \quad (3.8)$$

$$\dot{n}_{\text{ht}}(x) = c\sigma_T \int_1^{3/(4x)} d(\gamma)N(\gamma) , \quad (3.9)$$

where the step function S [$S(z)=1$ for $z>0$ and $S(z)=0$ otherwise] insures Thomson scattering and the delta function reflects the well-known photon energy gain when scattering radiation off of isotropic ultrarelativistic electrons

$$x_{\text{final}} = (4/3)\gamma^2 x_{\text{initial}} . \quad (3.10)$$

Note that when pairs have cooled to the trans-relativistic regime Equations (3.8) and (3.10) no longer hold, but fortunately little energy transfer is involved (see Lightman and Zdziarski 1987). Electrons at γ cool at the rate

$$\dot{\gamma} = -\sigma_T c \left(\frac{4}{3}\gamma^2 - 1\right) \int_0^{3/(4\gamma)} dx' n(x')x' , \quad (3.11)$$

where $(\frac{4}{3}\gamma^2 - 1)x'$ is the energy lost by the electron when scattering off a photon of energy x' : Note that the cooling rate scales as γ^2 while the annihilation of pairs goes as γ^{-2} (see equation 2.14). This is why we may neglect annihilation in the nonthermal pair population. We ignore electron transport (diffusion and winds) throughout this paper, and can therefore integrate the electron continuity equation to

obtain the nonthermal electron densities

$$N(\gamma) = -\dot{\gamma}^{-1} \int_{\gamma}^{\gamma_{\max}} d\gamma' [\dot{N}_{pp}(\gamma') + \dot{N}_{inj}(\gamma')] . \quad (3.12)$$

When pairs cool to subrelativistic energies they thermalize to a population characterized by total density N_0 and temperature T_0 [or, equivalently, the dimensionless temperature $\theta_0 = kT_0/(m_e c^2)$]. This population will scatter photons into and out of x at the rates

$$\begin{aligned} \dot{n}_{th+}(x) &= N_0 c \int dx' n(x') \sigma_{KN}(x') \\ &\times \delta \left(x'(1 + 4\theta_0 - x'/[1+x']) \right) , \end{aligned} \quad (3.13)$$

$$\dot{n}_{th-}(x) = N_0 c \sigma_{KN}(x) n(x) . \quad (3.14)$$

Here we have the average fractional energy change suffered by a photon of initial energy x as it scatters off the thermal pair population

$$\frac{\Delta x}{x} = 4\theta_0 - \frac{x}{1+x} . \quad (3.15)$$

This treatment correctly produces upscattering when $x < 4\theta_0$ and downscattering otherwise. The temperature θ_0 is determined by requiring that no net energy exchange occur between the thermal pairs and radiation

$$0 = \int dx \Delta x n(x) \sigma_{KN}(x) . \quad (3.16)$$

Substituting equation (3.15) for Δx and solving for θ_0 yields

$$\theta_0 = \frac{\int dx \frac{x^2}{1+x} n(x) \sigma_{KN}(x)}{4 \int dx x n(x) \sigma_{KN}(x)} . \quad (3.17)$$

The density of thermal pairs is given by the balance of pair production and annihilation

$$N_0^2 = \frac{\int d\gamma \dot{N}_{PP}(\gamma)}{2 \frac{1}{2} \frac{1}{2} \frac{3}{8} \sigma_{Tcg_{ann}}(\theta_0)} . \quad (3.18)$$

Finally, photons are created by pair annihilation at the rate

$$\dot{n}_{cre}(x) = 2N_0^2 \frac{1}{2} \frac{1}{2} \frac{3}{8} \sigma_{Tcg_{ann}}(\theta_0) \delta(x - 1 - \frac{3}{2}\theta_0) . \quad (3.19)$$

Here we assume the two photons share equally in the available energy.

Solution Method

We difference the photon energy uniformly in the logarithm of the dimensionless energy $x=h\nu/(m_0c^2)$ between the values $10^{-8} < x < 10^4$. The total number of x-bins is denoted $N_{\text{bins},x}$. The photon number density per unit volume per unit x at x_i we denote as $n(x_i)$. The total number density of photons in energy bin i is then $n(x_i)\Delta x_i$, where Δx_i is the energy width of bin i , and x_i is the geometric mean value of x within the bin. Similarly we difference electron energy uniformly in the logarithm of the dimensionless Lorentz factor $\gamma=1/(1-\beta^2)^{1/2}$ between the limits $1 < \gamma < 10^4$. We define $N(\gamma_i)$ to be the electron (negative electrons plus positrons) number density per unit volume per unit γ at γ_i (always with negative electrons and positrons in equal measure), define $\Delta\gamma_i$ to be the width of the i^{th} bin, and note that $N(\gamma_i)\Delta(\gamma_i)$ is the total number density of electrons in the i^{th} bin, where γ_i is the geometric mean value in bin i .

With discretized energy spectra, the photon continuity equations (3.3) or (3.4) represent a coupled system of $N_{\text{bins},x}$ ordinary differential equations for the $N_{\text{bins},x}$ variables $n(x_i, h)$ at each point h in the atmosphere. These can be simultaneously numerically integrated upward from the primary emission surface through the atmosphere. At each integration step, equations (3.12), (3.17), and (3.18) determine the steady-state electron distributions from the local photon distribution. The initial conditions applied at the emission surface

($h=0$) correspond to the primary spectral energy fluxes $F_{\text{hard}}(x_i)$ and $F_{\text{soft}}(x_i)$ described earlier. The initial conditions can be written as:

$$n(x_i, 0) = \frac{F_{\text{hard}}(x_i) + F_{\text{soft}}(x_i)}{x_i (m_e c^2) c} \quad (3.20)$$

Two distinct integration techniques are used. The first is an adaptive step size, fifth-order Runge-Kutta routine taken from Press et al. 1986 and modified by the author for present circumstances. Step size is controlled by the estimated error in the fractional change of each $n(x_i)$ over each step. The second method is an adaptive step size, fourth-order Runge-Kutta routine created by the author. Step size here is controlled by both the fractional change of the thermal pair density N_0 and the constancy of the integrated photon energy flux F , where

$$\begin{aligned} F(z) &= \sum_i c n(x_i, z) x_i \Delta x_i \\ &= \sum_i [F_{\text{soft}}(x_i) + F_{\text{hard}}(x_i)] \Delta x_i = \text{const} , \end{aligned} \quad (3.21)$$

for the plane, and

$$F(r) = \sum_i c n(x_i, r) x_i \Delta x_i$$

$$= \frac{r_e^2}{r^2} \sum_i [F_{\text{soft}}(x_i) + F_{\text{hard}}(x_i)] \Delta x_i = \text{const} , \quad (3.22)$$

for the sphere. We find little difference in results produced by the two methods, but a significant savings in computational time accompanies the latter. The runs presented in the following section were done using the faster technique.

Results

Uniform Infinite Radiating Plane

Figures 18 and 19 present the vertical structure of a typical cascade shower found by the author for emission from a uniform infinite surface. In order to more readily gain physical insight into the shower cascades investigated here, we do not include any spatially distributed photon or particle injection throughout the atmosphere. Figure 18 gives the density of subrelativistic pairs $N_0(h)$ (cm^{-3}) as a function of the height h (cm) above the surface. (The density of relativistic pairs is always much less than that of nonrelativistic pairs because we find relativistic pairs to cool rapidly.) Figure 19 gives the local photon spectrum (specific dimensionless energy flux: $\text{erg}/m_e c^2 / \text{cm}^2 / \text{s} / x$, where $x = h\nu / m_e c^2$) at several values of h , the seven lines A-G corresponding to the spectrum at heights labeled A-G in Figure 18. Line A in both figures corresponds to the input spectrum at $h=0$. The input spectrum has a soft component consisting of blackbody emission at $T_{\text{disk}} = 5 \times 10^4$ and a hard component consisting of a power law with energy flux slope

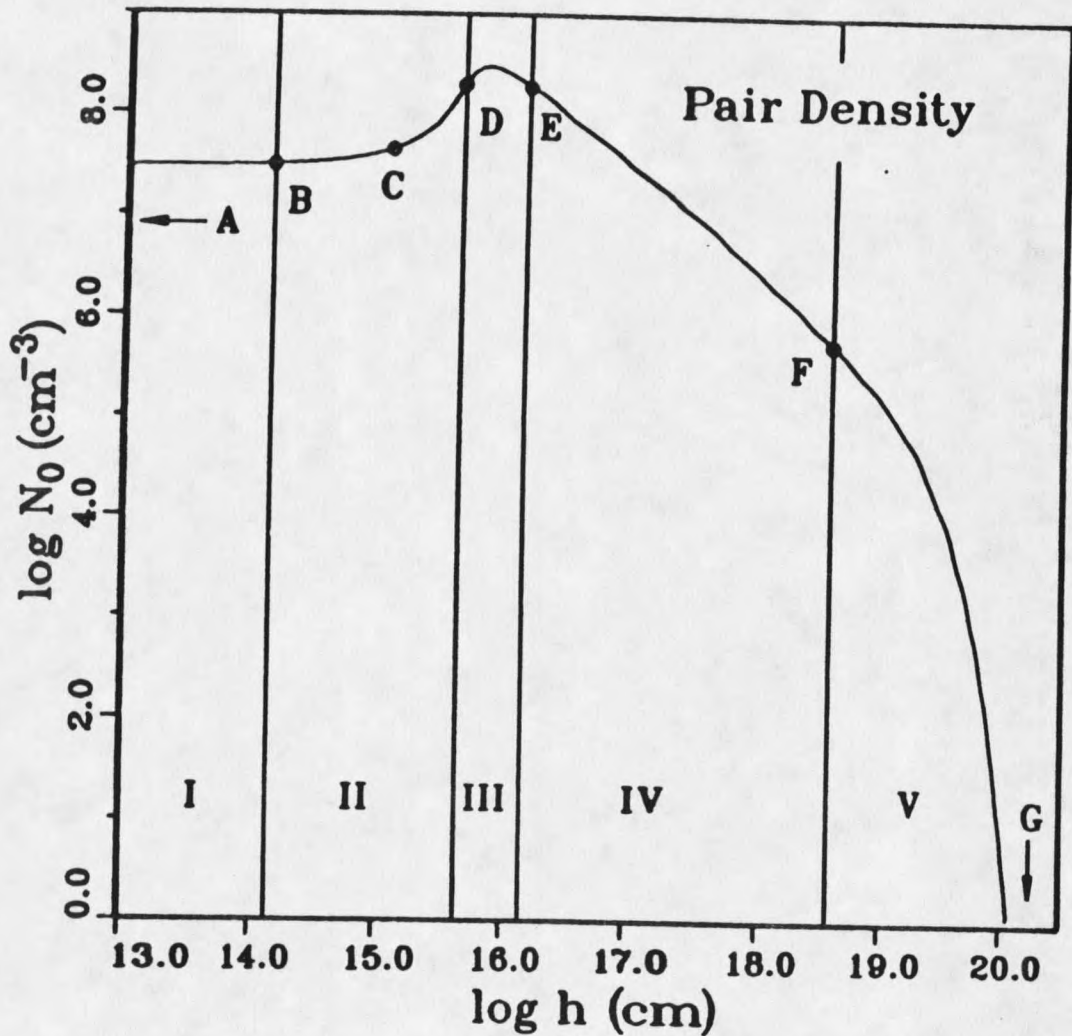


Fig. 18. Thermal pair density profile, and characteristic vertical zones, in typical steady-state pair cascade shower atmosphere above uniform infinite radiating plane. Density N_0 is combined density of negative electrons and positrons in cm^{-3} . Height h above the plane in cm. Primary input spectrum: (1) soft component consisting of $T=5 \times 10^4 \text{K}$ blackbody; (2) hard component consisting of power law extending through the range $2.373 \times 10^{-5} < x < 10^4$, with energy slope $\alpha=0.5$, carrying 10% of total power. Points A-G are heights corresponding to spectra shown in Fig. 19. Point A corresponds to $h=0$; point G to arbitrarily large distances.

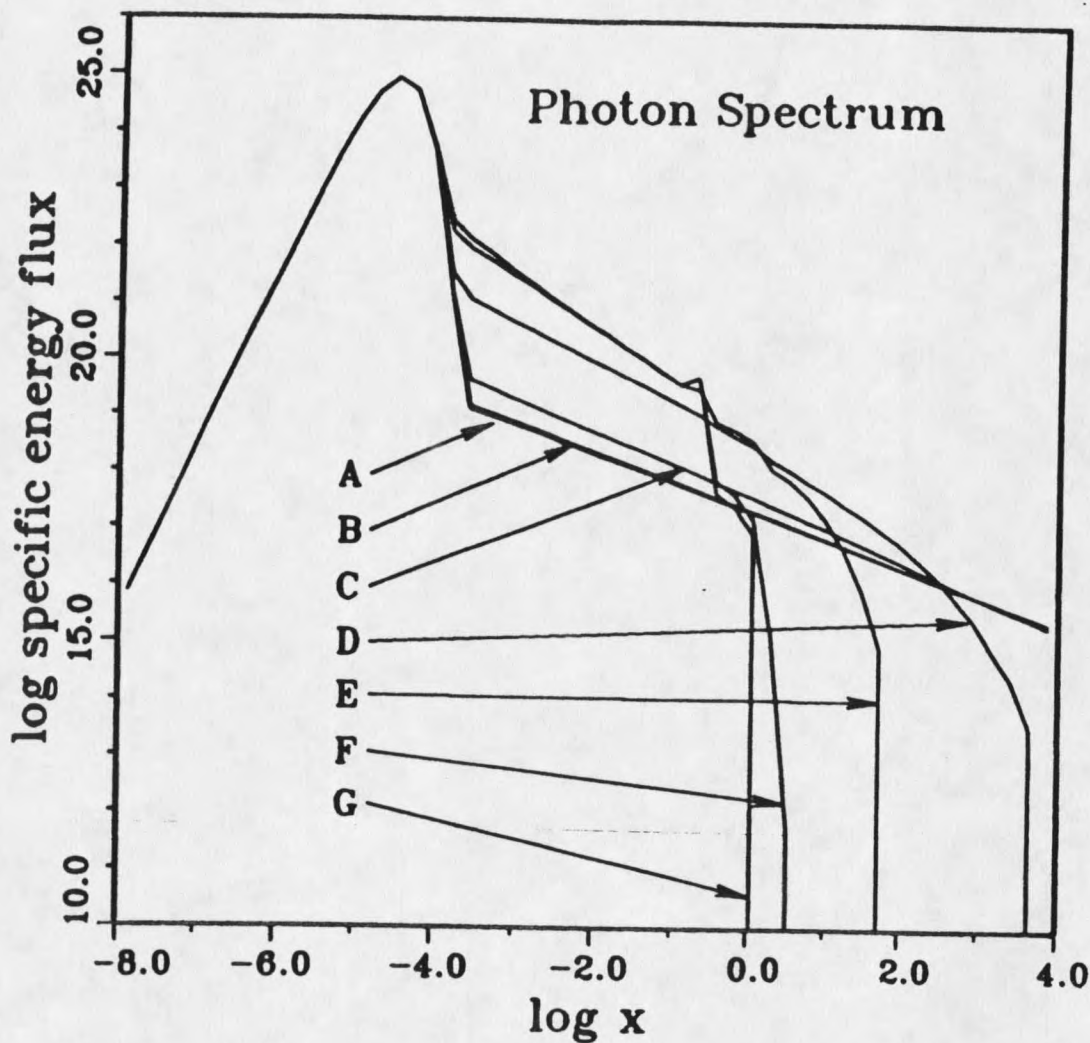


Fig. 19. Radiation spectrum at heights corresponding to points A-G in Fig. 18. Line A is the primary input; G is the escaping output. Units are dimensionless specific energy flux [$\text{erg}/(\text{m}_e c^2)/\text{cm}^2/\text{sec}/(h\nu/\text{m}_e c^2)$] as a function of dimensionless energy $x=h\nu/\text{m}_e c^2$.

$\alpha=0.5$ ($F(x) \propto x^{-\alpha}$) carrying 10% of the total luminosity ($f_{\text{hard}}=0.1$) and extending from the blackbody maximum to $x_{\text{max}}=10^4$. (See the photon source spectrum section for details.) We employ a numerical resolution of $N_{\text{bins},x}=50$. Figure 18 also displays the five characteristic domains, or vertical zones, into which we generally find the atmosphere divided. The zones are labeled I-V to facilitate reference. Figures 18 and 19 are quite representative of the atmospheres resulting from a wide range of input spectra. In this section we shall investigate in some detail the important features of this atmosphere, and then use it as a point of reference from which to investigate atmospheres formed by differing primary spectra.

Zones I and II are quite closely fit by an exponential growth in the thermal pair density:

$$N_0(h) = N_0(0) e^{(h/L_{\text{cas}})} , \quad (3.23)$$

where L_{cas} is the scale height of the increase and $N_0(0)$ is the thermal pair density at the emission surface. The division between the essentially flat zone I and the accelerating growth in II marks the location $z \approx L_1$. To explain this behavior we conduct the following order-of-magnitude argument.

First consider one of the consequences of the "Analytic Estimates for Power-Law Distributions" section, what may be called the "law of steepening slope." Power-law distributions of photons shallower than $\alpha=1.0$ will always steepen towards $\alpha=1.0$ under the

influence of pair cascade processes. This is clearly seen in Figure 19, where the power-law portion of each spectrum steepens from line A through line G. Next we note that the soft blackbody distribution acts predominantly as a seed photon source: very little energy is transferred from the blackbody photons to the power law, although many blackbody photons are upscattered into the power law. This means that the energy carried by the power law remains essentially constant as one proceeds up through the atmosphere. This conservation of power-law energy then requires the high-energy end of the power law to drop in density and the low-energy end to gain in density as the cascade progresses and the slope steepens. There must, then, exist an energy at which photon densities do not change as the power law steepens. This falls typically between $x=1$ and $x=x_{\max}$. Photon densities at energies near this "pivot point" will not change appreciably during this stage of the cascade. This is easily seen in Figure 19, where lines A, B, and C (all of which lie in zones I or II) exhibit progressive steepening, but remain anchored at a constant strength at energy $x \approx 10^3$. This results in lines A, B, and C evolving very little in the entire $x > 1$ region, but considerably in the $x < 1$ region.

Calling the integrated density of power-law photons below $x=1$, n_1 , and that above $x=1$, n_2 , conservation of energy keeps $n_2 \approx \text{constant}$. The rise in n_1 represents the effect of a positive feedback loop in which pairs upscatter photons from the blackbody distribution into n_1 , which then produce pairs, which upscatter more photons from the blackbody component into n_1 , and so on. Slightly

more quantitatively, we may further define n_e to be the total high energy (nonthermal) pair density, N_0 to be the total density of cool (thermal) pairs, and n_s to be the integrated blackbody photon density. The pair production requirement $2\langle x_a x_b \rangle < 10$ (see discussion of equation 3.6) roughly means a photon of energy x will pair produce predominantly with photons of energy $1/x$. This means pairs are created predominantly from interactions between the n_1 and n_2 populations. Note that the blackbody photons are too soft to pair produce with any photons at all: $2.82\theta_{\text{disk}} < 1/x_{\text{max}}$. Thus we write the pair creation rate as

$$\dot{n}_e \approx n_1 n_2 \sigma_T c, \quad (3.24)$$

where we approximate all cross sections in the derivation by σ_T . Since only one n_1 photon is absorbed to create a pair, but that pair will in turn upscatter many photons from n_{soft} into n_1 , upscattering into n_1 is the dominant process in n_1 's kinetic equation,

$$\frac{dn_1}{dh} \approx \frac{n_s n_e \sigma_T c}{c}. \quad (3.25)$$

The nonthermal electron steady-state balance of pair creation and cooling by the soft radiation yields

$$\dot{n}_e \approx n_e n_s \sigma_T c. \quad (3.26)$$

Substituting equations (3.24) and (3.26) into equation (3.25) we obtain

$$\frac{dn_1}{dh} \approx n_1 n_2 \sigma_T, \quad (3.27)$$

which yields exponential growth for n_1

$$n_1 \approx n_1(0) e^{(n_2 \sigma_T h)}. \quad (3.28)$$

The balance of pair creation and annihilation of thermal pairs will determine N_0 :

$$N_0^2 \sigma_T c \approx \dot{n}_e. \quad (3.29)$$

Substituting the above results for \dot{n}_e we obtain

$$N_0^2 \approx n_2 n_1(0) e^{(n_2 \sigma_T h)}. \quad (3.30)$$

And finally, taking the square root we have:

$$N_0 \approx n_2^{1/2} n_1(0)^{1/2} e^{(h/L_{\text{abs}})}, \quad (3.31)$$

where the cascade scale height is given approximately as

$$L_{\text{abs}} \approx \frac{1}{\sigma_T n_2}. \quad (3.32)$$

Notice the length scale for exponential growth is inversely proportional to n_2 , which is born out in our results (see Figure 23 and discussion thereof). More intense primary spectra, by increasing n_2 , will result in smaller scale heights and more compact atmospheres.

Figures 18 and 19 indicate that the photon spectrum shortward of the blackbody UV-hump remains a power law throughout zones I and II (lines A, B, and C). In the "Analytic Estimates or Power-Law Distributions" section of this chapter, we calculate the equilibrium thermal pair density in power-law photon distributions, which is given by equation (3.65) as a function of power-law slope, strength, and upper and lower limits. Applying that analysis to the input power-law of Figure 19 (line A) we obtain an estimate for the initial pair density of $N_0(0)_{\text{est}} = 1.77 \times 10^7 \text{ cm}^{-3}$. Figure 18 shows the actual initial value of $2.94 \times 10^7 \text{ cm}^{-3}$.

Zone III of the atmosphere represents a saturation of the pair cascade, and a consequent maximum of N_0 . In overview, pair cascades work to redistribute energy from a few high energy particles or photons to many lower energy particles and photons. In particular, cascades drive systems with abundant high energy populations towards a state in which radiation energy is spread equally among the decades of frequency. This state is a power law with a photon number density slope of $s=2$: $n(x) \sim x^{-s} \sim x^{-2}$. Precisely how this occurs is analytically derived in the "Analytic Estimates for Power-Law Distributions" section, and we now review the important features.

In a pair cascade, a photon power-law of number density slope s , that extends appreciably beyond $m_e c^2$ will produce pairs at the differential rate $P(\gamma) \sim \gamma^p$, with $p=s$. If a strong source of soft radiation is available to cool the new pairs, a steady-state pair density $N(\gamma) \sim \gamma^{-\Gamma}$, with $\Gamma=s+1$, will form. The upscattered photons form a power law $n'(\gamma) \sim \gamma^{-s'}$, where $s'=(1/2)(\Gamma+1)=(s/2)+1$. This new steeper distribution of photons produces a second steeper generation of pairs, and the cycle repeats. After i generations we have $s_i=(s_0+2^{i+1}-2)/(2^i)$. Any input $s_0 < 2$ will steepen and approach 2. An equilibrium exists at $s=2$ in which the scattered radiation spectrum from pairs has the same slope as the photons which produces those pairs, and no further slope evolution occurs. This cascade-driven spectral slope evolution is clearly seen in Figure 19. By the time the height signified by point E is reached (the end of zone III), the power-law slope has steepened to very near $s=2$, and no further steepening occurs.

Another result from the last section of this chapter is that equilibrium thermal pair density in a power-law photon distribution is maximized by $s=2$, for a given constant total power carried by the power law. Thus a maximum for N_0 is expected when the cascade saturated, as seen in Figure 18. The maximum value of N_0 may be estimated analytically by the results in the "Analytic Estimates for Power-Law Distributions" section. Applying equation (3.65) to the saturated $s=2$ power law in Figure 18, we obtain $N_0^{\max}=4.02 \times 10^8 \text{ cm}^{-3}$, compared with the actual value of $2.95 \times 10^8 \text{ cm}^{-3}$ from the figure.

Along with softening power-law slopes, pair cascades work to degrade maximum energies toward $m_e c^2$. This can be seen by estimating the maximum energy for each generation of γ -rays in a cascade. An initial γ -ray energy $x_0 \gg 1$ will interact with a low energy photon $1/x_0$ and produce a pair with energy $\gamma_0 = x_0/2$. This pair will predominantly upscatter soft photons $x_s \approx 10^{-4.5}$ to energies $x_1 = (4/3)\gamma_0^2 x_s = (x_0/3)x_0^2 \approx 10^{-5} x_0^2$. The cycle then repeats for further generations. If $x_0 = 10^4$, then $x_1 = 10^3$, $x_2 = 10^1$, $x_3 = 10^{-3}$, etc.. (Of course, when x is no longer above the pair production threshold $\sqrt{2}$, no further pair generations will be produced. The significance of this is that, as one proceeds up through the atmosphere, by the time several pair generations have occurred, and the cascade has saturated, the cascade processes no longer produce any $x > \sqrt{2}$ photons in abundance. Thus at any point in the atmosphere, the very highest energy photons are depleted by pair absorption, but not being replenished. The spectral high energy cut-off then proceeds down through the energies, as seen in lines D through G in Figure 19. (No depletion will be seen for $x > \sqrt{2}$ because low energy photons require an $x > \sqrt{2}$ photon to pair produce, but because of the power law, photon densities at $x < \sqrt{2}$ are much greater than at $x > \sqrt{2}$, so that each pair production event results in a much greater fractional density loss for the $x > \sqrt{2}$ than for $x < \sqrt{2}$. The $x > \sqrt{2}$ quickly deplete, and $x < \sqrt{2}$ are left virtually undiminished.)

The height h at which the high energy cut-off (called the γ -ray turnover by observers) has proceeded down to some energy x , can easily and accurately be estimated as the absorption length $L_{\text{abs}}(x)$

for a photon at x due to absorption by photons in the saturated $s=2$ power law (absorption by the blackbody photons is energetically prohibited).

We have analytically estimated the absorption lengths for all $x > \sqrt{2}$ in the "Analytic Estimates for Power-Law Distributions" section, and illustrate the results in Figure 34. The height of the curve above energy x indicates the absorption length at that energy, $L_{\text{abs}}(x)$, which indicates the approximate height in the atmosphere at which the exponential depletion at x begins. Or alternatively, the x corresponding to some L is the high energy cut-off at height $h=L$. This is in good agreement with the results in Figure 19. For example Figure 19 indicates depletion at $x \approx 10^2$ occurs somewhere between positions D and E, around $h \approx 10^{16}$ cm. The analytic estimates of Figure 34 give $h = 10^{16.3}$ cm for the high energy cut-off to occur at $x = 10^2$. Note that Figure 34 correctly predicts that higher energies will deplete first (smaller L_{abs}). We defer discussion of the behavior near $\sqrt{2}$ to later in this section.

Zone IV represents a steady decline in thermal pair density at the precise rate

$$N_0 \sim 1/h . \quad (3.33)$$

This behavior begins at the height where the high energy cut-off has proceeded down into the interval $\sqrt{2} < x < \sqrt{10}$. The significance of this interval is that only within this interval can two photons of the same energy pair produce, whereas $x_1 < \sqrt{2}$ must interact with $x_2 > \sqrt{2}$ and

$x_1 > \sqrt{10}$ must interact with $x_2 < \sqrt{10}$. Note that the power-law form of the spectrum dictates that the largest photon density within this interval is the lowest energy: the first (discretized!) energy above $\sqrt{2}$. Call this energy x_* and its density n_* . Pair production is then clearly dominated by $x_* + x_*$ interactions, and x_* is depleted at the rate

$$\frac{dn_*}{dh} \sim -n_* n_* , \quad (3.34)$$

which has the asymptotic solution

$$n_* \sim 1/h . \quad (3.35)$$

The balance of pair production and annihilation gives:

$$N_0^2 \sim n_* n_* , \quad (3.36)$$

which together with equation (3.35) gives equation (3.33).

Zone V of the atmosphere is well fit by an exponential decay in thermal pair density. Zone V begins when the high energy cut-off has reached x_* (the first discrete energy larger than $\sqrt{2}$), and n_* drops sufficiently so that the principal pair creation mechanism is no longer $x_* + x_*$ but rather $x_* + x_{**}$ where x_{**} is the first discrete energy below $\sqrt{2}$. The energies $x < \sqrt{2}$ suffer essentially no depletion because they have entered pair production only with photons whose densities were

much less than $n(x)$. Thus the $n(x < \sqrt{2})$ remain essentially constant and the depletion rate for x_* becomes exponential as predicted:

$$\frac{dn_*}{dh} \sim -n_* n_{**} , \quad (3.37)$$

$$n_* \sim e^{(-An_{**}h)} . \quad (3.38)$$

where A is some constant. We balance pair annihilation with creation:

$$N_0^2 \sim n_* n_{**} , \quad (3.39)$$

Equation (3.38) along with the approximate constancy of n_{**} gives the exponential decay:

$$N_0 \sim e^{(-An_{**}h)} , \quad (3.40)$$

where A is some constant. The location of the boundary separating zones IV and V is easily and accurately estimated by Figure 34. For $N_{\text{bins},x} = 50$, $x_* = 1.905$. This value is shown on the figure and corresponds to an absorption length of 2×10^{18} cm. Figure 18 indicates a boundary at 4×10^{18} cm.

We saw in the previous paragraph that the turnover from $N_0 \sim 1/h$ in zone IV to $N_0 \sim \exp(-Ah)$ in zone V occurs at a height about equal to the absorption length for x_* , $L_{\text{abs}}(x_*)$. Note, however, that as the numerical energy binning becomes increasingly fine (increasing the

number of bins $N_{\text{bins},x}$) x_* approaches $\sqrt{2}$ and Figure 34 indicates $L_{\text{abs}}(x_*)$ increases. This is a direct result of the approximate pair creation threshold $x_1 x_2 \geq 2$. Photons at $\sqrt{2}$ can only interact with similar photons. As this threshold is approached, there are increasingly fewer photons available. (This effect remains when the exact cross section is used, only there the threshold is $x_1 x_2 \geq 1$.) This increase in $L_{\text{abs}}(x_*)$ should postpone the onset of exponential attenuation of the pair atmosphere to larger h . In the continuum limit $x_* \rightarrow \sqrt{2}$ and $L_{\text{abs}}(x_*) \rightarrow \infty$ because a photon at $x = \sqrt{2}$ can react with only the infinitesimally small number of photons at that energy, and zone IV should continue upward indefinitely, never turning over to zone V.

Figure 20 presents $N_0(h)$ for the model parameters of Figures 18 and 19, but for several values of $N_{\text{bins},x}$. The extension of the $N_0 \sim 1/h$ behavior higher into the atmosphere is clearly seen for increasingly fine binning. The continuum limit is easily obtained by simply extrapolating the $1/h$ dependence outward indefinitely. This affords a tremendous savings in computational time over running large $N_{\text{bins},x}$ models. For $N_{\text{bins},x} \geq 50$, little error is seen in the lower regions of the atmosphere when binning is changed. The total atmospheric optical depth to thermal pairs becomes logarithmically unbounded in the continuous limit. This is predicted by inserting the $N_0 \sim h^{-1}$ dependence into the definition of the optical depth up to height h ,

$$\tau(h) = \int_0^h dh N_0(h) \sigma_T . \quad (3.41)$$

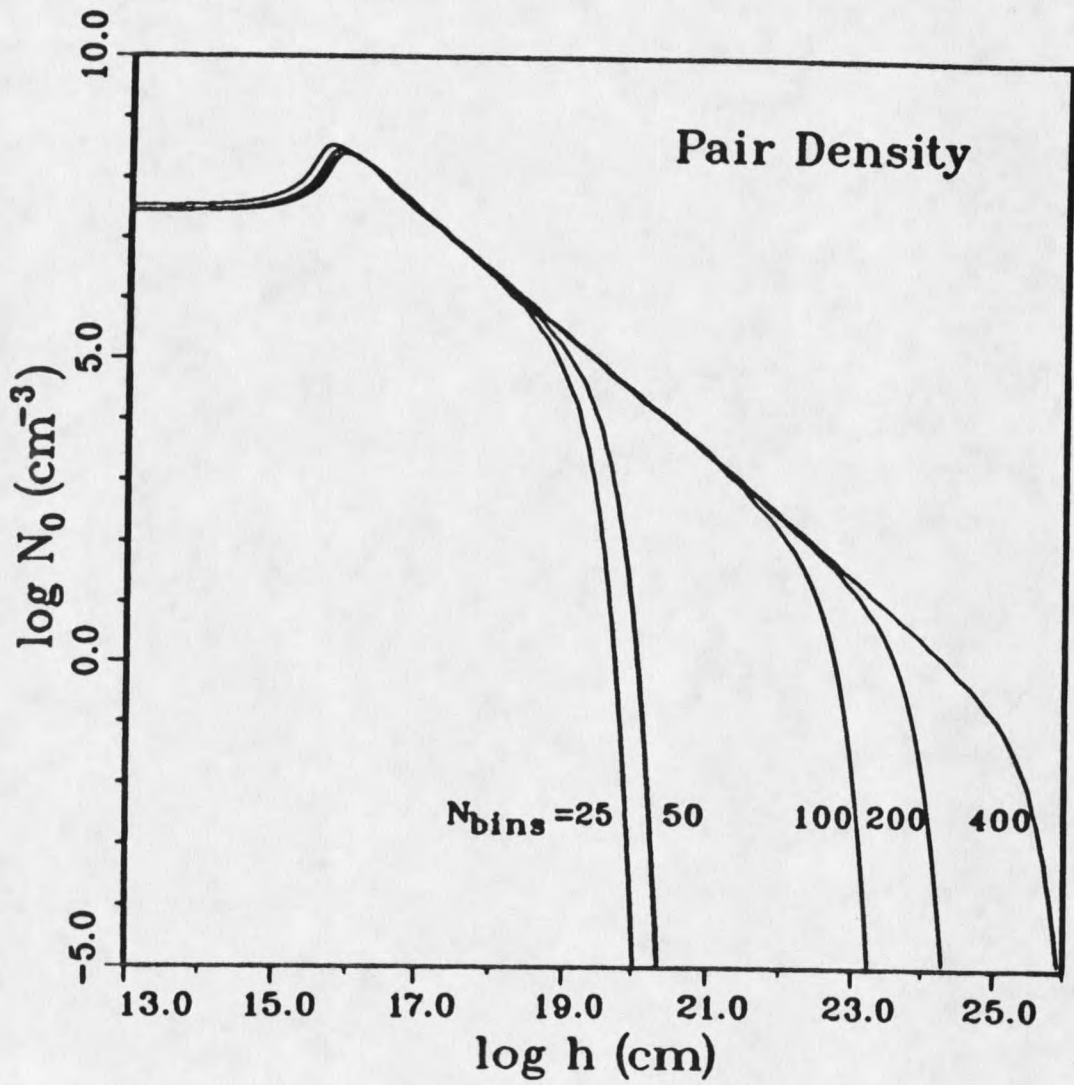


Fig. 20. Variation of thermal pair density N_0 with height h above the plane, for several values of the total number of photon energy bins. $N_{\text{bins}} = 50$ corresponds to the model in Fig. 18.

We obtain $\tau(h) \sim \log(h)$, which is unbounded as h approaches infinity. The logarithmic form of $\tau(h)$ is seen in Figure 21, in which $\tau(h)$ is shown for several $N_{\text{bins},x}$. As $N_{\text{bins},x}$ increases, the optical depth follows a logarithmic profile further out into the atmosphere. For a finite number of bins, the turn-over to zone V exponential decay will be encountered. Since the integral of e^{-h} out to infinity is bounded, only a finite contribution to τ is gained in zone V, and the τ profile in Figure 21 levels out to remain finite. The infinite value in the continuum limit is not altogether surprising and is simply a direct consequence of the (unphysical) infinite uniform plane geometry (somewhat analogous to calculating the column energy density of an electric field above a uniform infinite charged plane), as we shall see in the following section.

Concern would be warranted if a second quantity, the integrated pair yield PY, were also infinite. The pair yield (see Chapter 2) measures the overall efficiency with which the atmosphere turns hard radiation injection into pair creation. We must modify the definition of PY used by others in uniform spherical volume sources (see Lightman and Zdziarski 1987, and Fabian et al. 1986) to accommodate the present geometry,

$$PY = \frac{\int_0^{\infty} dh \int_0^{\infty} d\gamma \dot{N}_{PP}(\gamma)}{\int_0^{\infty} dx F_{\text{hard}}(x)} \quad (3.42)$$

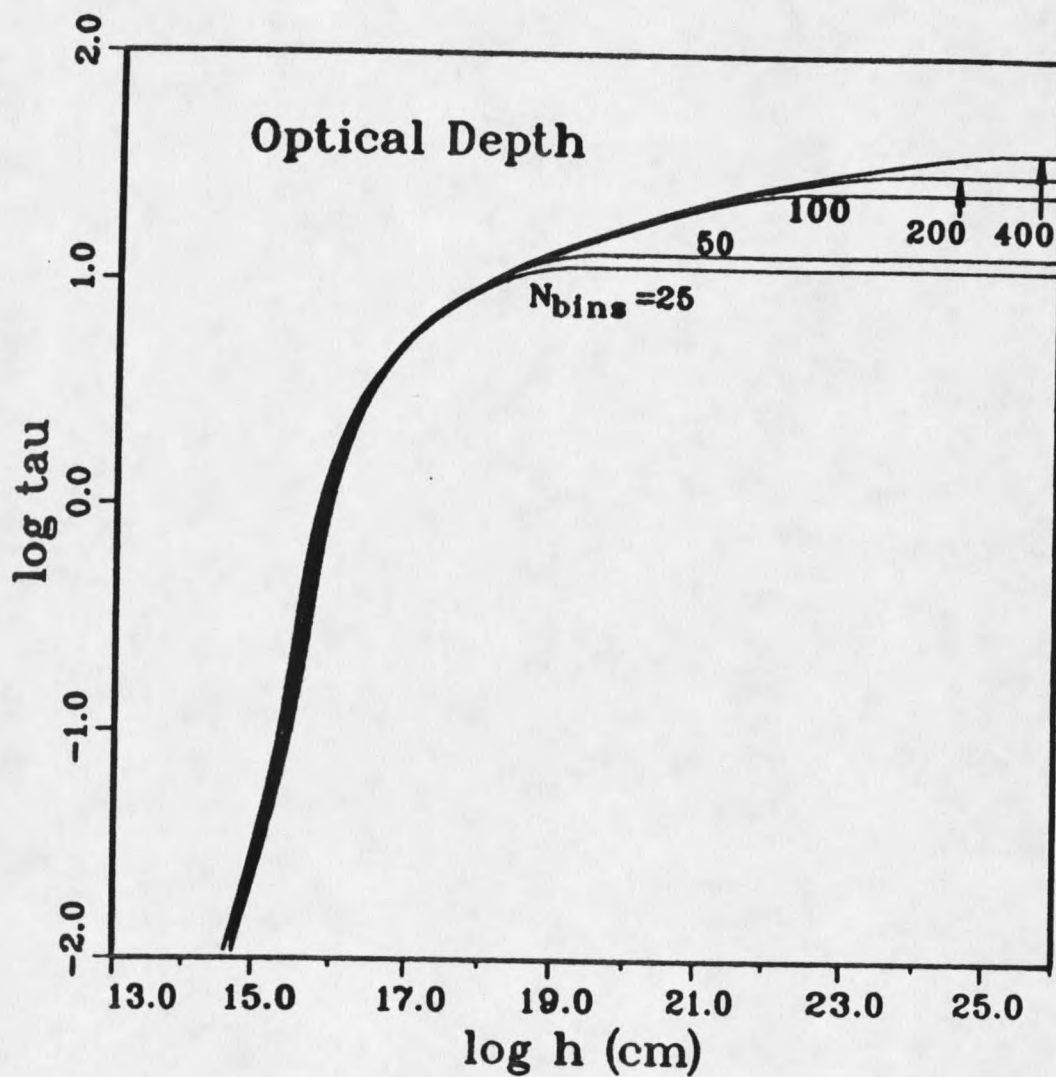


Fig. 21. Optical depth to thermal pairs through height h , for several values of the total number of photon energy bins. $N_{\text{bins}} = 50$ corresponds to model in Fig. 18.

The variation of PY with $N_{\text{bins},x}$ is shown in Figure 22 and is seen to trend to a well-defined finite limit of around 8-9%, comparable to the uniform spherical volume source results of typically 10% or less.

Finally we investigate the effects on atmospheric structure and spectrum caused by variations in the input photon spectrum, using the prototypical model of Figures 18 and 19 as reference. We keep $N_{\text{bins},x}=50$. The continuum limit may be taken by inspection usually. First we vary the partitioning of available luminosity between the soft (blackbody) and hard (power-law) input. Figure 23 shows $N_0(h)$ for several values of f_{hard} from 10^{-4} to 0.99.

The immediately striking feature in Figure 23 is that, as long as the soft source remains stronger than the power law ($f_{\text{hard}} < 0.5$), the pair density profiles all end up on the same $h-N_0$ line. This is caused by the combined action of two effects, both of which depend on the fact that power-law densities are proportional to f_{hard} ($n_1, n_2 \sim f_{\text{hard}}$). Equation (3.31) then tells us that $L_{\text{cas}} \sim f_{\text{hard}}^{-1}$. a 10-fold increase in f_{hard} , for example, will cause the pair cascade to occur 10 times further out into the atmosphere, as Figure 23 clearly shows. Equation (3.32) tells us that $N_0 \sim f_{\text{hard}}^{+1}$. Thus a 10-fold increase in f_{hard} corresponds to raising the graph in Figure 23 by a factor of 10, which is also clearly seen. When $f_{\text{hard}} > 0.5$, the assumption of a plentiful soft source is no longer valid in our crude estimates, and the estimates fail, as evidenced by the anomalous behavior seen for $f_{\text{hard}}=0.9$ and 0.99.

Next we investigate the effects of input power-law slope of the atmosphere. Figure 24 shows the pair profile $N_0(h)$ for several input

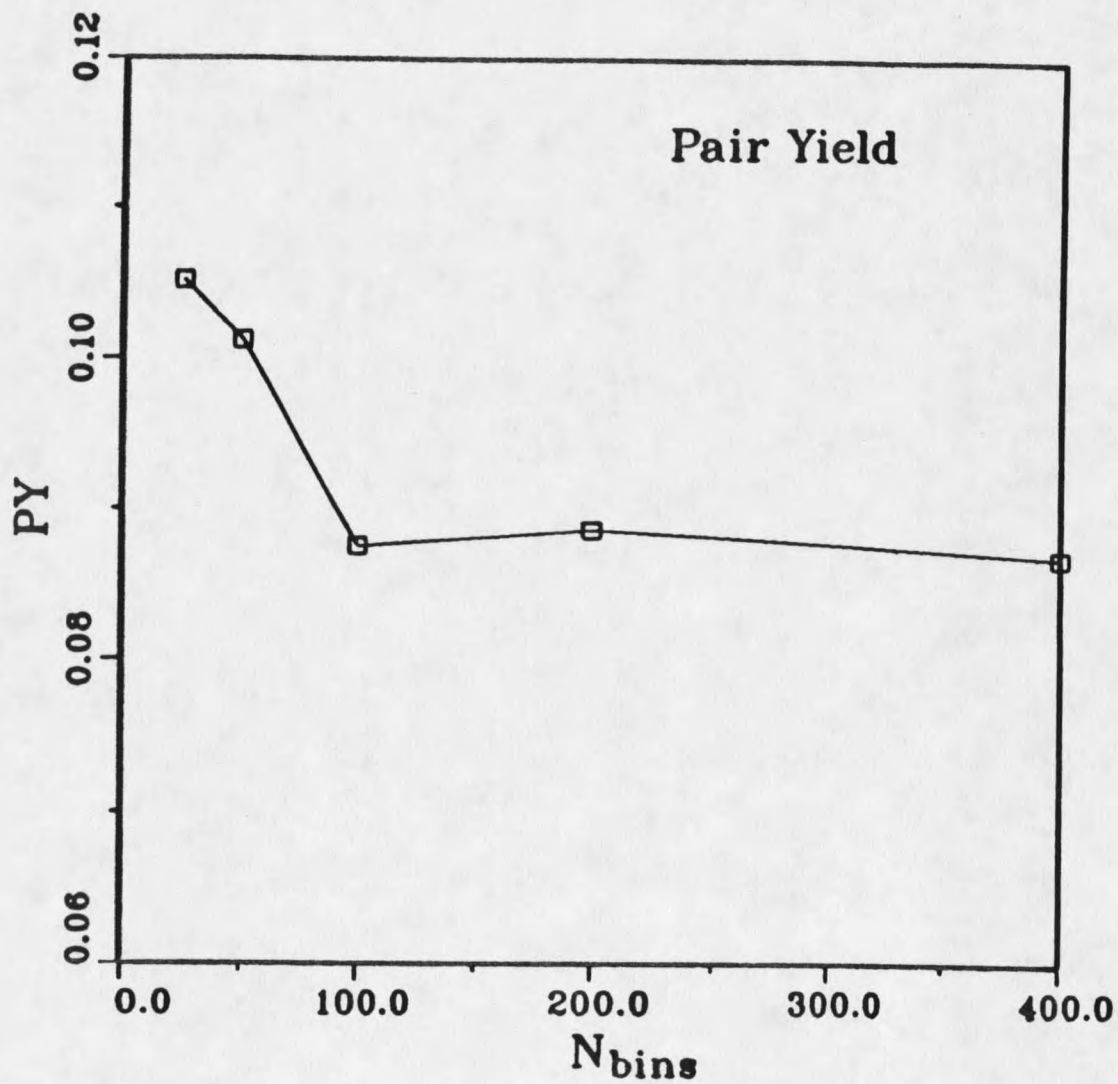


Fig. 22. Total pair yield of atmosphere for several values of the total number of photon energy bins. $N_{bins}=50$ corresponds to model in Fig. 18.

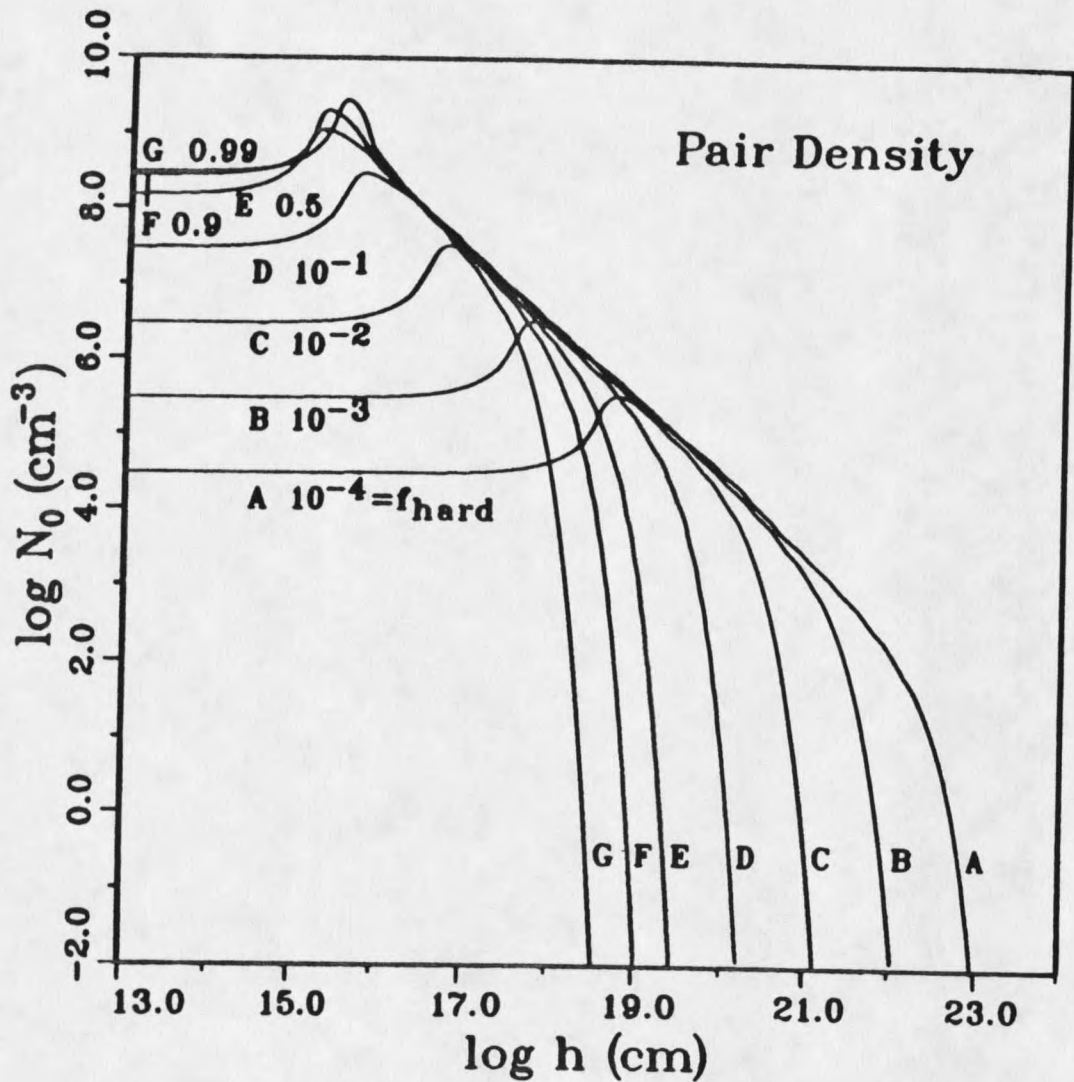


Fig. 23 Variation in thermal pair density with height above the plane, for various fractions of total input power going to hard primary component. The $f_{\text{hard}}=10^{-1}$ line corresponds to model in Fig. 18.

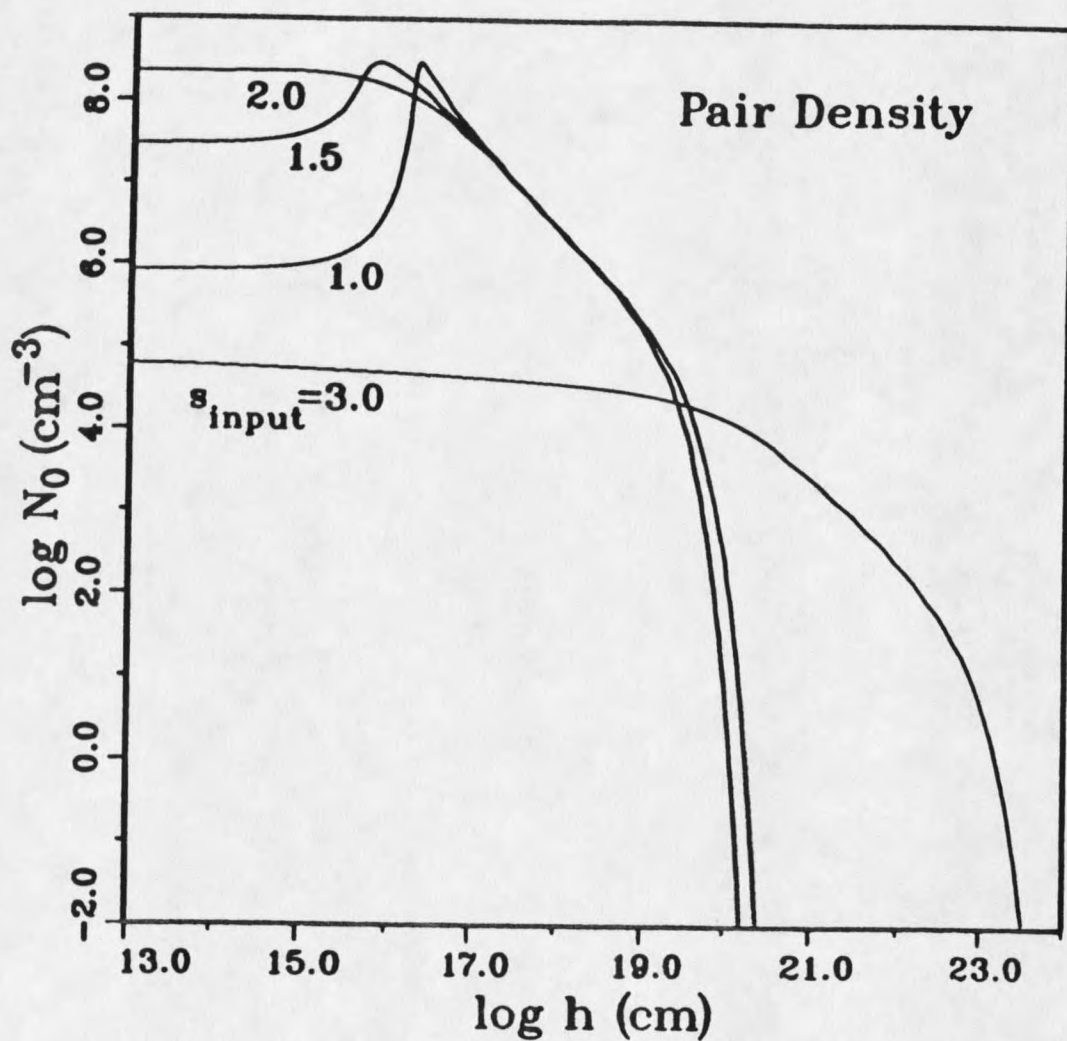


Fig. 24. Variation in thermal pair density with height above the plane, for various input power-law number density slopes s ($s=\alpha+1$). The $s=1.5$ ($\alpha=0.5$) line corresponds to model in Fig. 18.

power-law energy slopes, $\alpha=0, 0.5, 1,$ and 2 (corresponding number density slopes are $s=1, 1.5, 2,$ and 3). A critical value of $\alpha=1.0$ ($s=2.0$) becomes apparent. Input energy slopes shallower than $\alpha=1.0$ evolve to saturation at $\alpha=1.0$ and will produce the characteristic pair profile (zones I-IV). Energy slopes steeper than $\alpha=1.0$ have too few high-energy photons to produce a cascade and the atmosphere merely attenuates as γ -rays densities are gradually depleted, as seen for the $\alpha=2$ ($s=3$) line in Figure 24. The spectral evolution for initial energy slope $\alpha=2.0$ is shown in Figure 25 and reveals little power-law steepening (evidence for the absence of a functioning cascade) and high energy depletion.

Finally we investigate the results of monochromatic primary input. Delta function input produces final (escaping) spectra quite similar to that from distributed input, but can reveal interesting features within the atmosphere. For instance Figure 26 shows the radiation spectrum at various heights (increasing from lines A through J) above a source radiating the same total energy flux as in the model of Figure 19, but now with the soft emission concentrated at the blackbody maximum $x=2.8\theta_{\text{disk}}$ and the hard emission concentrated at $x_{\text{max}}=10_4$. A power law bridging the soft and hard input energies quickly forms from upscattered soft photons and gradually steepens towards energy slope 1.0 as the cascade progresses, as in the continuous input models. However a prominent pair annihilation line at $x=1.0$ appears in the lower regions of the atmosphere. This is seen because the power law is not yet strong enough to overwhelm it. Higher up the line is drowned out by the power law and no

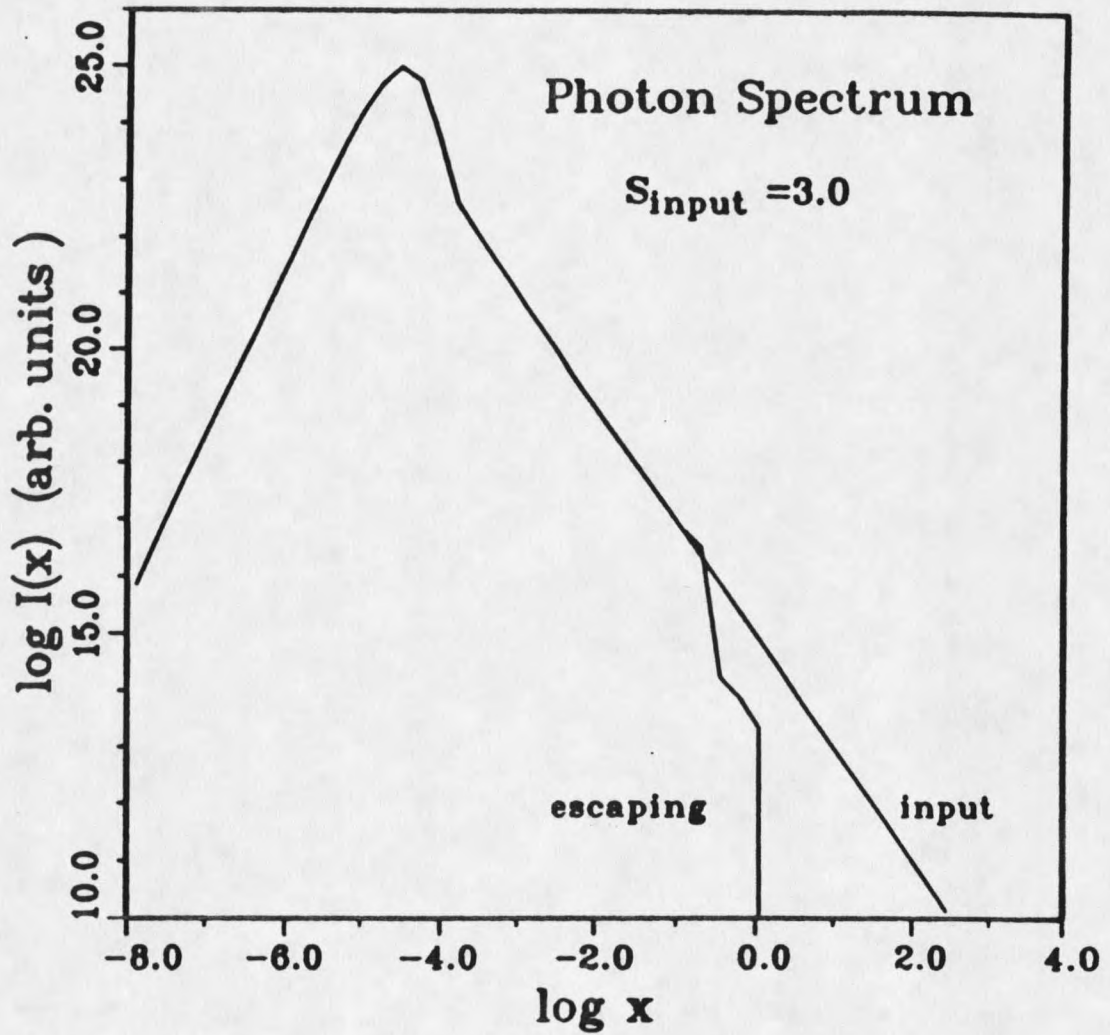


Fig. 25. Primary and escaping spectra for $s=3.0$ primary hard input of Fig. 24.

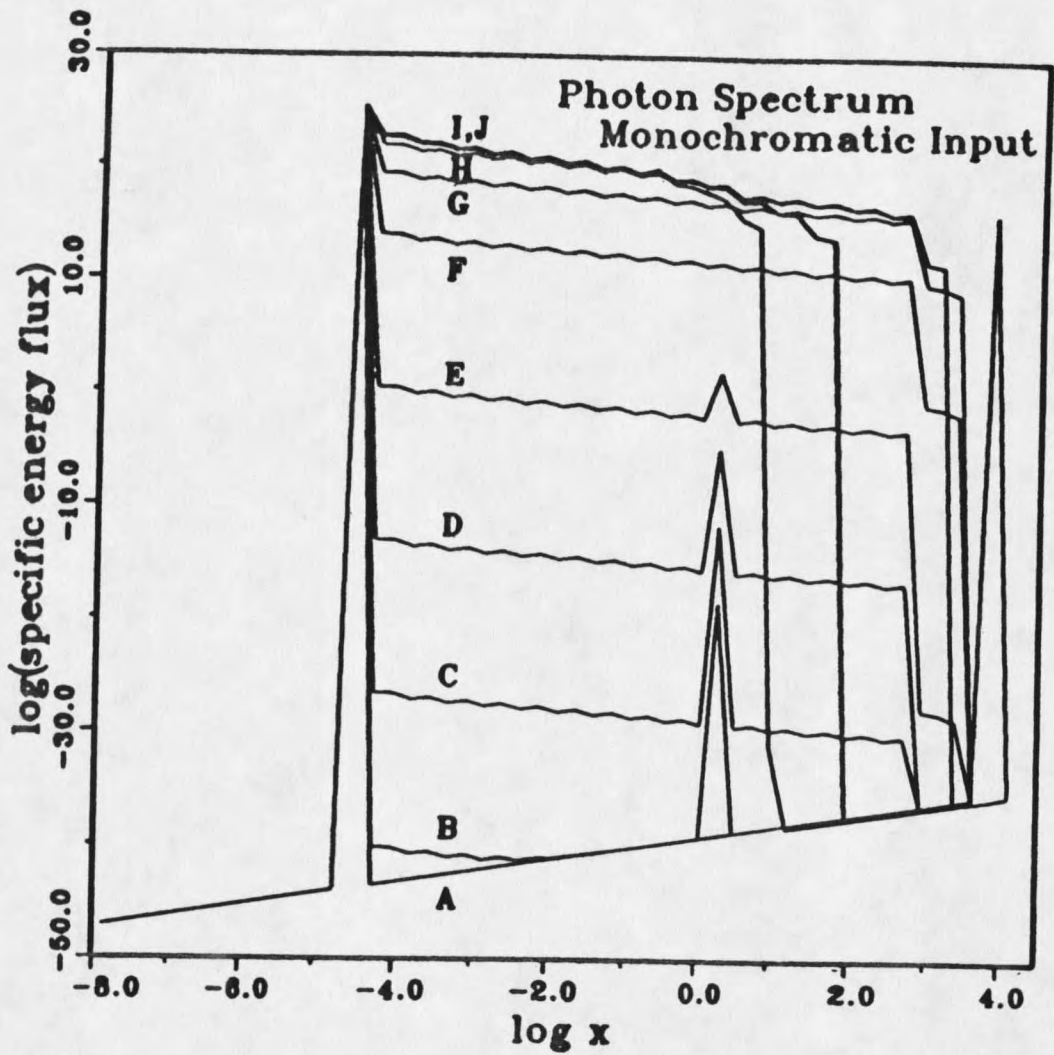


Fig. 26. Radiation spectrum at increasing heights (lines A-J) above the plane for delta function primary spectra at energies $x_{\text{soft}}=2.37 \times 10^{-5}$ and $x_{\text{hard}}=3.8 \times 10^3$. Line A is primary input; line J is output.

annihilation line at $x=1.0$ escapes to the observer. (It is found, though, that many models will emit an observable annihilation feature downscattered and broadened from $x=1$ by thermal pair scattering; see Figure 19). Figure 27 shows the pair profile for the delta function input model of Figure 26. Pair densities just above the emission surface (small h) are quite small, because direct pair production cannot occur between the soft and hard input energies. Only as the power law develops and strengthens can pair densities rise, as power-law photons begin to pair produce.

Uniform Radiating Spherical Surface

The principal qualitative differences between pair cascade shower atmospheres formed over infinite planar sources and those formed around spherical surface sources result from the inverse square law dilution of densities (see the second term in equation 3.4). The effect can be approximately characterized by the existence of a so-called freeze-out radius r_f , around any spherical emission surface. Beneath r_f the geometrical effects of curvature are negligible and the atmosphere closely resembles that from an infinite plane. Above r_f the inverse square law will dominate reaction rates and photon densities drop as $1/r^2$. This can be seen more quantitatively, if we define $h=r-r_e$ to be the height above the emission radius r_e corresponding to any position r , and write the vertical profile of photon density due solely to geometry:

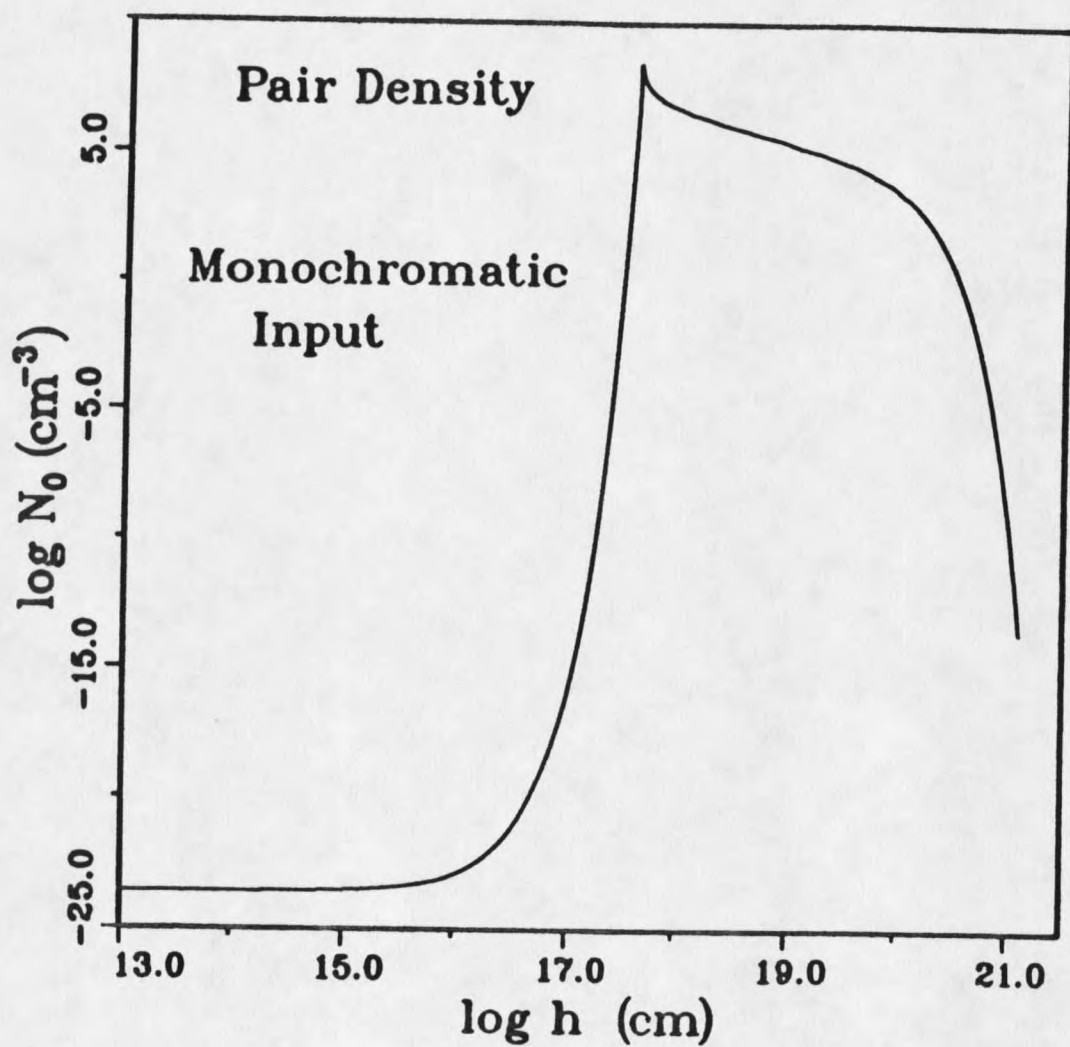


Fig. 27. Variation of thermal pair density with height above the plane for the monochromatic input model of Fig. 26.

$$n(h) = n(r_e) \frac{1}{1+(h/r_e)^2} . \quad (3.43)$$

The freeze-out height above the emission, $h_f \approx r_e$, separating the two regimes of behaviour is then seen to be equal in magnitude to the emission radius

$$h_f \approx r_e , \quad (3.44)$$

When $h \ll r_e$, $n(h) \approx n(r_e)$. When $h \gg r_e$, $n(h) \approx n(r_e)(r_e^2/h^2)$. This is illustrated quite clearly in Figure 28. Here we have plotted as a reference the planar source N_0 profile of Figure 18 (the line marked "plane"), against the profiles obtained from emission of the same spectrum (same shape and same total energy flux: energy/area/time emitted), but from uniform spherical surfaces of varying radii: $r_e = 10^{13}$, 10^{14} , 10^{15} , 10^{16} , 10^{17} , and 10^{18} cm. The horizontal axis represents h , the height above the surface. The prediction of equation (3.44) is born out: the pair density closely follows the planar results (Figure 18) out to $h \approx r_e$, where a turnover to inverse square law domination $N_0 \sim 1/r^2$ occurs. This $1/r^2$ decline solves the problem of infinitely thick atmospheres found above uniform infinite planar sources. Integration of $1/r^2$ out to infinity yields finite optical depths.

The "freezing-out" aspect of h_f is strikingly shown in Figure 29, where six lines, labeled by the size of the emission radius, denote the escaping spectrum from each model of Figure 28. For reference, the

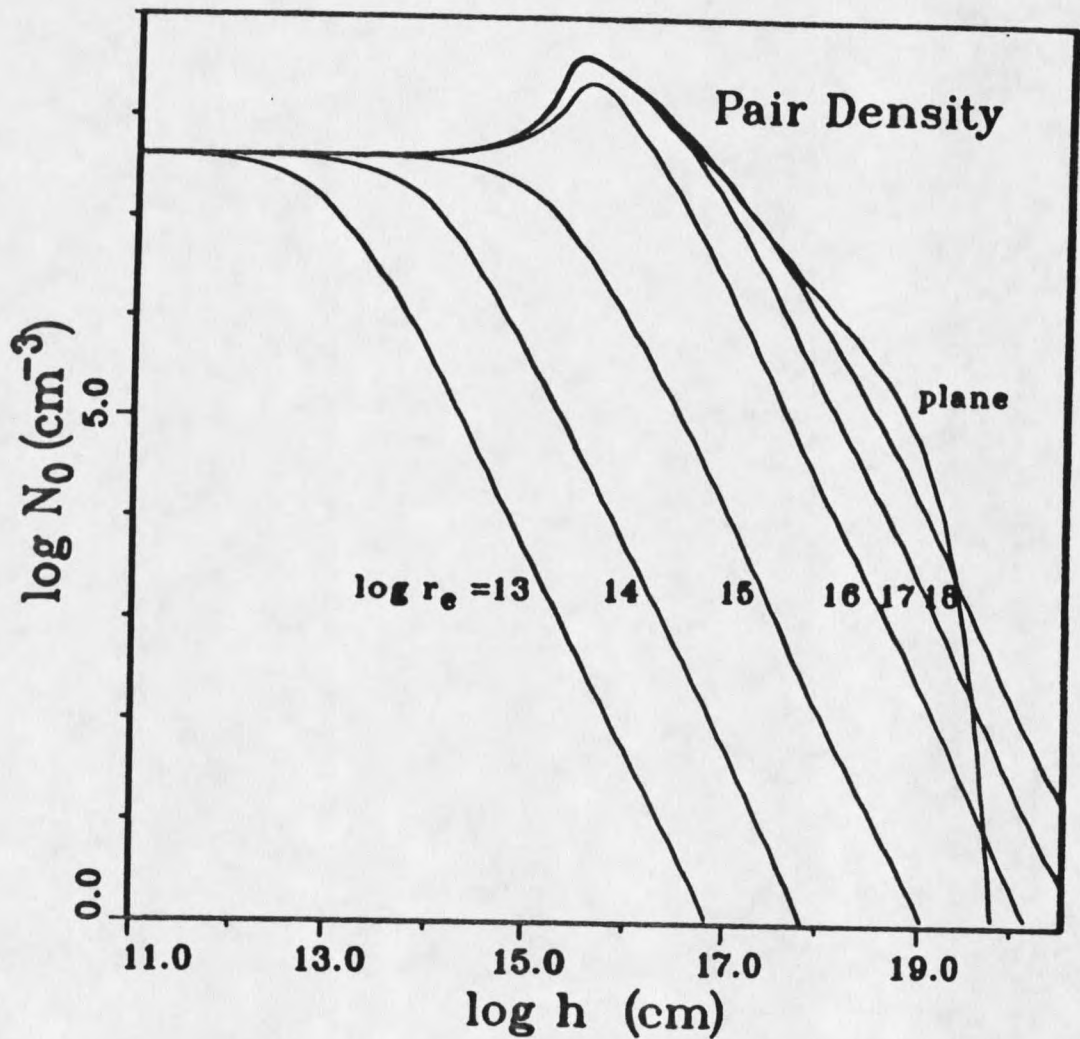


Fig. 28. Variation of thermal pair density with height above a uniform radiating spherical surface of radii $r = 10^{13-18}$ cm. Input spectral shape same as in Fig. 18; strength of input adjusted so energy flux (or density) at emission surface is held constant while r_e is varied. The pair density profile from Fig. 18 is shown as "plane" for comparison.

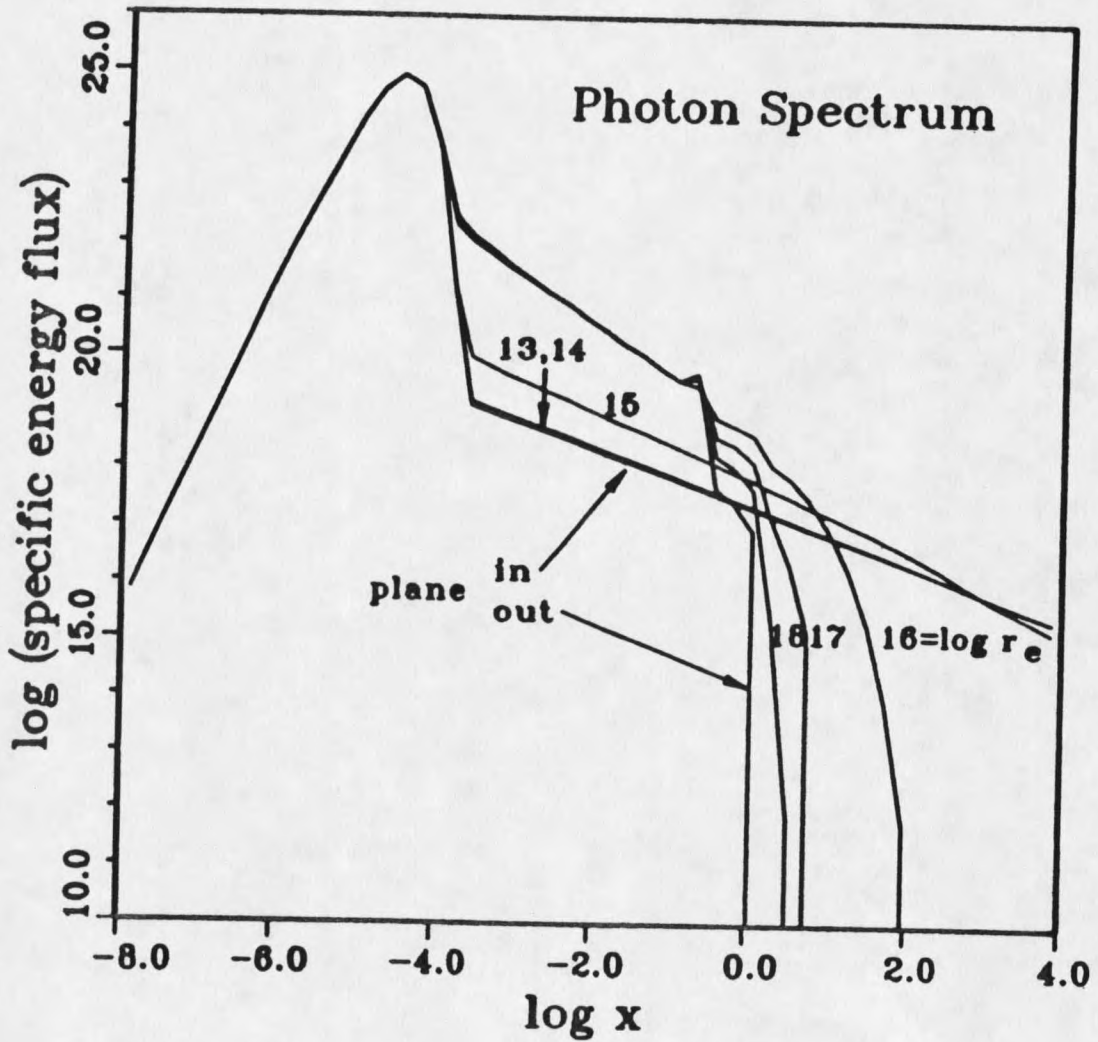


Fig. 29. Escaping spectrum from models of Fig. 28. Input and output spectra for the corresponding planar emission are shown as "plane in" and "plane out," respectively.

initial (input) and final (escaping) spectra for the corresponding planar case are plotted as lines "in" and "out," respectively. The final (escaping) spectrum from a spherical source with an emission radius r_e is seen to be approximately the local spectrum found inside the equivalent planar source atmosphere at height $h=r_e$. For example, compare the similarity between the escaping spectrum from a spherical system of $r_e=10^{16}$ cm shown in Figure 29, with the spectrum existing a distance $10^{16.2}$ cm above a planar source shown as line "E" in Figure 19. The spectral evolution ceases, or freezes out, at the freeze-out height.

We next present results of spherical models run with input parameters set to a specific astrophysical context relevant to AGN. (Refer to the photon source section and the Appendix for motivation and details.) In particular we shall consider a typical AGN: a luminous Seyfert galaxy or a moderate quasar. Mass estimates of the central black hole for these objects suggest $M=10^8 M_{\text{sol}}$. Without specifying whether the accretion flow takes the form of quasi-spherical inflow or a disk, theory tells us that most of the luminosity will be released in the central $100r_g$ region of the flow. We will approximate either of these as a uniform spherical emission surface of radius

$$r_e = 100 (2GM/c^2) = 3 \times 10^{15} \text{ cm} . \quad (3.45)$$

As discussed earlier, the spherical models are appropriate both very close to and very far from a finite disk, and of course is appropriate for a spherical flow.

The soft emission component consists of a blackbody spectrum at $T_{\text{disk}}=5 \times 10^4 \text{K}$, while the hard component consists of a power law of energy index $\alpha=0.5$ extending from the blackbody maximum $x=2.373 \times 10^{-5}$ to $x=10^4$. The fraction f_{hard} of the energy flux carried by the hard component is left as a free parameter. (No theory has been developed to predict the partitioning of soft and hard radiation from AGN central engines. However, Lightman and White 1988 have found that the observed, or reprocessed, spectra from a large class of AGNs exhibit f_{hard} in the range 0.25 to 0.77.) The entire input spectrum is uniformly scaled up or down by specifying an effective brightness temperature, to provide any total luminosity $L=\epsilon \dot{M} c^2$ (erg/sec), accommodating any combination of accretion rate \dot{M} and accretion radiative efficiency ϵ .

Figure 30 shows the total thermal pair optical depth τ of the resulting atmosphere for dimensionless accretion rates $\dot{m} = \dot{M} / \dot{M}_{\text{Edd}}$ from 10^{-1} to 10^3 , and for $f_{\text{hard}}=10^{-4}, 10^{-3}, 10^{-2}, 10^{-1}, 0.5,$ and 0.9 . We use $\epsilon=0.1$, a reasonable value. The power law dependence found in τ for small \dot{m} and f_{hard} occurs when the freeze-out height falls in zone I. Recall that in zone I, N_0 is constant in h , and is proportional to $n_1^{1/2} n_2^{1/2}$, where $n_{1(2)}$ is the density of power-law photons $\langle \nu \rangle 1$. These densities are proportional to \dot{m} and f_{hard} , so: $N_0 \sim \dot{m} f_{\text{hard}}$, in complete agreement with the asymptotic region of Figure 30. Pair optical depth is positively correlated to the accretion rate, but saturation is always reached for sufficiently large accretion rates. This happens when the freeze-out radius lies outside of zone III, the cascade maximum. This is seen in the upper right portion of Figure

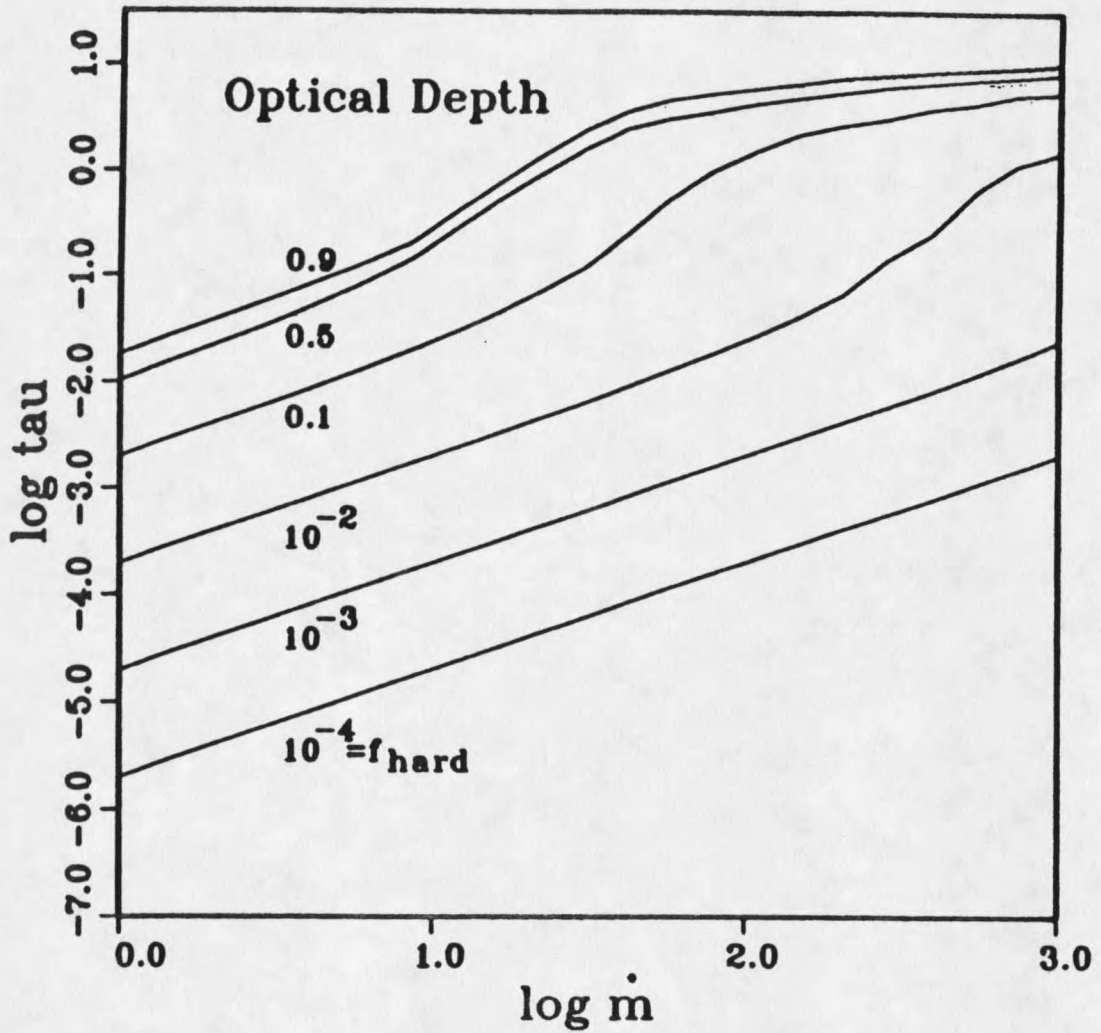


Fig. 30. Total optical depth of atmosphere forming around $100r_s$ radius accretion cloud surrounding $10^8 M_{\text{sol}}$ black hole as function of dimensionless accretion rate \dot{m} and energy partitioning f_{hard} . Primary spectral shape same as for model in Figs. 18 and 19.

30. Inverse square dilution takes over and the atmosphere thins too quickly for the optical depth to further increase as one proceeds out through the atmosphere. Pair optical depth is positively correlated with f_{hard} only up to $f_{\text{hard}} \approx 0.5$, past which a decline in τ is encountered due to the inability of the now sparse soft photon reservoir to supply many photons to the cascade mechanism. Figure 30 shows that for sub-Eddington accretion rates, the resulting pair atmosphere remains thin, with $\tau \leq 10^{-2}$. At moderately super-Eddington accretion, the optical depth can approach or surpass unity, and can reach a maximum of $\tau \approx 10$ for very super-Eddington accretion and very hard input. Figure 31 presents the variation of pair yield PY with \dot{m} and f_{hard} . The maximum values $\text{PY} = 10\% - 20\%$ at saturation agree with the maxima found in uniform spherical volume sources (Lightman and Zdziarski 1987, and Fabian et al. 1986).

Observationally, the soft X-ray spectral power-law slope is of considerable interest. Figure 32 presents the 2-10 keV (soft X-ray) energy index α for the same model parameters as Figures 30 and 31, in which the input spectral index was 0.5. For sufficiently small f_{hard} and in the freeze-out height is small enough to "catch" the spectrum before appreciable spectral evolution took place. This is seen by the trend to $\alpha = 0.5$ in that region of parameter space. The saturation seen for large f_{hard} and \dot{m} indicates the freeze-out height was great enough to allow the cascade to evolve the spectral slope to its terminal value of near $\alpha = 1.0$. Note for a given f_{hard} , the energy index is positively correlated with luminosity increases. Some surveys, however, suggest that the index remains fairly constant during

